Vessel driven correction of brain-shift

Ingerid R. Reinertsen, M.Sc

Department of Biomedical Engineering

McGill University

Montreal, Québec, Canada

February 4, 2007

A thesis submitted to McGill University in partial fulfillment of the requirements for the degree of Doctor of Philosophy

Your file Votre référence
ISBN: 978-0-494-32378-6
Our file Notre référence
ISBN: 978-0-494-32378-6

To Anthony and Emil

Acknowledgements

I would like to acknowledge:

Louis Collins for guidance, support, encouragement and good humour;

All of my co-authors: Maxime Descoteaux, Dr. Kaleem Siddiqi, Dr. Frank Lindseth and Dr. Geirmund Unsgaard;

Dr. R. F. Del Maestro for helpful discussions and access to the operating room;

All the members of the the Image Processing Laboratory and Brain Imaging Center, in particular Simon Drouin, Anka Kochanowska, Pierre Hellier, Laurence Mercier, Mallar Chakravarty and Simon Duchesne.

Table of Contents

List of Tables

List of Figures

Abstract

The displacement and deformation of brain tissue is a major source of error in image-guided neurosurgery systems. This thesis presents the design, implementation and validation of an image registration algortithm to detect and correct brain-shift using pre-operative MR images and intraoperative Doppler ultrasound data. The registration algorithm uses segmented vessels from both modalities, and estimates the displacement using a modified version of the iterative closest point (ICP) alogrithm. The least trimmed squares (LTS) was used to reduce the number of outliers in the point matching procedure. The selected points were first used to estimate a linear transformation between the two data-sets, and then used to drive a thin-plate spline transform to achieve non-linear registration.

A deformable brain phantom was designed, constructed and characterized in order to serve as a gold standard in the validation of the registration algorithm. The reproducibility of the elastic deformation of the phantom was evaluated using MR imaging and surface measurements. The experiments showed that the phantom was well suited for MR and ultrasound imaging (B-mode and Doppler) with sub-millimeter reproducibility for the deformations.

Validation of the registration technique was then completed in three parts. First, the technique was tested and validated using realistic simulations where the results were compared to the known deformation. The registration technique recovered 75% of the deformation in the region of interest accounting for deformations as large as 20 mm.

Second, a phantom study was performed where both MR and ultrasound images of the phantom were obtained for three different deformations. The registration results based on MR data were used as a gold standard to evaluate the performance of the ultrasound based registration. On average, deformations of 7.5 mm magnitude were corrected to within 1.6 mm for the ultrasound based registration and 1.07 mm for the MR based registration. Finally, the registration algorithm was validated using five retrospective clinical data-sets. Because the true displacement remained unknown, the method was validated using homologous landmarks identified in the original data, the exclusion of selected vessels, and finally manual segmentation of non-vascular structures in anatomical data. The tracking of homologous landmarks show that the registration algorithm was able to correct the deformation to within 1.24 mm, and the validation using excluded vessels and anatomical structures show an accuracy close to 1 mm. Pre-processing of the data can be completed in 30 seconds per dataset, and registrations can be performed in less than 30 seconds. This makes the technique well suited for intra-operative use.

Résumé

La déformation du tissu cérébral est une source majeure d'erreurs dans les systèmes de neuro-navigation guidés par l'image. Cette thèse présente la conception, implémentation et validation d'une méthode pour détecter et corriger les déformations cérébrales en utilisant des images par résonance magnétique (IRM) pre-operatiores et des images par échographie Doppler intra-operatoires. L'algorithme de recalage emploie des vaisseaux segmentés des deux modalités, et estime le déplacement en utilisant une version modifiée de l'algorithme ICP (Iterative Closest Point). La technique des moindres carrés tamisés a été utilisé pour réduire le nombre de points aberrants dans la procédure de recalage. Les points sélectionnés sont d'abord utilisés pour calculer une transformation linéaire et ensuite ils sont utilisés pour estimer la déformation non-linéarire à l'aide du principe de la flexion des plaques minces.

Un fantôme déformable a été conçu, construit et charactérisé pour servir comme étalon or dans la validation de l'algorithme de recalage. La reproducibilite de la déformation élastique du fantôme a été évalue en utilisant l'imagerie par résonance magnétique et des mesures en surface. Les experiences ont montré que le fantôme était bien adapté pour l'imagerie par résonance magnétique et l'imagerie par échographie avec une reprodicibilité sous-millimetre pour les déformations.

La validation de la téchnique de reclage a été completé en trois parties. Tout d'abord, l'algorithme a été testé et validé en utilisant des simulations réalistes ou le résultat a été comparé avec la déformation connue. L'algorithme de recalage a retrouvé 75% de la

déformation dans le volume d'interêt en prenant en compte des déformations jusqu'a 20 mm. Deuxiémement, une étude utilisant le fantôme a été completeé, ou des images par résonance magnétique et des images par échographie ont ete obtenues pour trois déformations differentes. Les résultats du recalage basés sur les données IRM ont été utilisés comme étalon or pour évaluer la performance du recalage base sur les données d'échographie. En moyenne, des déformations de 7.5 mm ont été corrigés avec une exactitude inférieure a 1.6 mm pour les recalages basés sur des données d'échographie et 1.07 mm pour le recalage basé sur des données d'IRM. Finalement, l'algorithme de recalage a été validé en utilisant des données cliniques rétrospectives. Parce que le vrai déplacement reste inconnu, la méthode a été validé en utilisant des points homologues identifiés dans les données originales, l'exclusion de vaisseaux selectionnés et finalement la segmentation de structures non-vasculaires dans les données anatomiques. Le pistage de points homologues montre que la méthode est capable de corriger les déplacements avec une exactitude de 1.24 mm, et la validation utilisant des vaisseaux exclus montre une exactitude proche de 1 mm. Le traitement des données avant le recalage peut être fait en 30 secondes par volume, et le recalage en lui-meme peut être completé en moins de 30 secondes. Ceci rend la méthode bien adapté à l'utilisation intra-operatoire.

Original contributions

The following are the main contributions of this work:

1. Development of a new vessel based algorithm for linear and non-linear registration.
2. Design, construction and characterization of a deformable brain phantom for brain-shift simulations.
3. Validation of registration algorithm using simulated data, phantom data and retrospective clinical data.
4. Quantitative comparison of vessel based MR-to-Ultrasound registration and MR-to-MR registration using phantom data.
5. Software development for pre-processing of angiographic images, linear and non-linear registration, visualization of vessel data and evaluation of registration results.

Author contributions

I am the first author of all three manuscripts included in this thesis and have performed all of the methodological developments, experimental design, data processing and analysis of the results. I have also coded the registration algorithm as well as the pipeline for data pre-processing. The contributions of co-authors included supervision, data acquisition and review of the manuscripts. The following list, by manuscript, summarizes the contributions of co-authors:

Chapter 4 - A Realistic Phantom for Brain-shift Simulations

Authors: I. Reinertsen and D. L. Collins;

Guarantors of integrity of entire study: I. R., D. L. C; study concepts and design: I. R., D. L. C; literature research: I. R.; phantom design and construction: I. R.; data acquisition: I. R.; experiments and analysis: I. R.; manuscript preparation: I. R.; manuscript revision/review: I. R., D. L. C.; editing and final version approval: I. R., D. L. C.;

Chapter 5 - Validation of Vessel-based Registration for Correction of Brain-shift

Authors: I. Reinertsen, M. Descoteaux, K. Siddiqi and D. L. Collins;

Guarantors of integrity of entire study: all authors; study concepts and design: I. R., D. L. C; literature research: I. R.; data acquisition: I. R.; vessel segmentation algorithm: M. D., K . S.; registration algorithm: I. R. D. L. C.; experiments and analysis: I. R.; manuscript preparation: I. R. (M. D. prepared section 5.3.1); manuscript revision/review: all authors; editing and final version approval: I. R., D. L. C.;

Chapter 6 - Clinical validation of vessel-based registration

Authors: I. Reinertsen, F. Lindseth, G. Unsgaard, and D. L. Collins;

Guarantors of integrity of entire study: all authors; study concepts and design: I. R., F. L., D. L. C.; literature research: I. R.; data acquisition: G.U, F. L.; experiments and analysis: I. R.; manuscript preparation: I. R.(F.L prepared sections 6.3.1 and 6.3.2); manuscript revision/review: all authors; editing and final version approval: I. R., F. L., D. L. C.;

Chapter 1

Introduction

1.1 Motivation

The main purpose of medical imaging is to provide physicians with high-quality images in order to facilitate the diagnosis and treatment of patients. In neurosurgery in particular, imaging modalities such as magnetic resonance imaging, computer tomography, ultrasound imaging and positron emission tomography play a vital role in the determination of the type, localization, extent and malignancy of different brain lesions and their relation with normal tissue. The images are used for primary diagnosis as well as surgery planning, guidance during the operation and to evaluate the surgical result after the procedure. Different modalities provide complementary information about anatomy, pathologies, vasculature and function. It is therefore crucial to be able to incorporate all the data available into a system where the neurosurgeon can access the multi-modal images aligned with each-other and the patient in order to plan and perform the optimal surgery. This is the main role of any image-guided surgery system. Another key component of such systems is the ability to track surgical tools and display their position relative to the pre-operative images. Most systems assume that the patient

anatomy remains in a fixed position during surgery and that the relation with the pre-operative images is unchanged during the entire procedure. This assumption is rarely valid in cases that require an open craniotomy in order to reach the surgical target. Brain tissue will shift and deform under influence of drugs, leakage of liquids such as cerebro-spinal fluid and gravity in addition to retraction and resections performed by the surgeon. This tissue movement can seriously compromise the accuracy of the image-guided navigation system, and the surgeon can no longer rely on the images for updated information about the patients anatomy.

This thesis is concerned with the detection and correction of such brain deformations during surgical procedures. In order to reach this goal, a system based on intraoperative ultrasound imaging and image registration was developed and tested using numerical simulations, phantom data and retrospective images from patients who had undergone brain surgery. This method will ultimately improve the accuracy of the navigation systems currently used in neurosurgery and provide neurosurgeons with a tool to get updated information about anatomy, pathologies, vasculature and function at any time during surgery.

1.2 Outline of thesis

This thesis is organized into seven chapters. Chapter 2 contains the background material necessary for the understanding of the work presented in the following sections.

This chapter includes an introduction to neuronavigation systems and the various imaging modalities currently used in surgical planning and navigation. The causes and effects of brain-shift are briefly presented, as well as a review of the main detection and correction techniques available. Chapter 3 includes a detailed description of the

registration algorithm developed and validated in this thesis. Chapters 4, 5 and 6 are all separate manuscripts. In the first paper, the design, construction and characterization of a deformable brain phantom for validation of detection and correction techniques are presented [1]. The second paper includes a detailed description of the registration algorithm and presents validation experiments using simulations and data obtained from the phantom described in the previous chapter [2]. The third and last paper describes the application of the method to retrospective data from five patients who have undergone neurosurgical procedures for brain tumors, cerebral aneurysms or arterioveneous malformations (AVMs) [3]. The thesis concludes with a summary of the results presented in the previous chapters and some suggestions for future research.

Chapter 2

Background

Neurosurgical planning is an extensive process that aims at collecting all the necessary information about the patient and the disease in order to optimize the surgical outcome. This includes a detailed neurological examination of the patient and in most cases, one or more imaging studies. Image data gathered for primary diagnosis and surgical planning can be imported into a neuronavigation system prior to surgery and used for image guidance during the operation. This chapter reviews imaging modalities most commonly used in neurosurgical planning and navigation. It then gives a detailed description of a typical neuronavigation system and the steps required to obtain image guidance. The chapter continues with a summary of the causes, extent and effects of brain-shift and concludes with a detailed review of available detection and correction techniques.

2.1 Imaging for neurosurgical planning and navigation

As mentioned above, the goal of imaging for neurosurgical planning and guidance is to gather as much information as possible about the surgical target and its anatomical and

functional relationship with surrounding tissue. This information is crucial in order to plan the surgical path and optimize the outcome by minimizing the damage to healthy tissue.

2.1.1 Anatomical imaging

Anatomical imaging is used to for primary diagnosis to identify the localization, shape, size, type and malignancy of the surgical target. Conventional x-ray imaging was the first anatomical imaging technique used in neurosurgical planning, and developed soon after the discovery of x-rays by Roentgen in 1895 [4]. One of the main limitations of standard radiography is the lack of soft tissue contrast. A conventional x-ray image of the human head shows only a projection of the bony skull, and gives very limited information about possible anomalies inside the brain. In order to increase the amount of information in the images, a number contrast agents were discovered and developed during the first half of the 20th century [4]. Air and later oxygen and helium were injected into the skull in order to visualize the ventricular system and the subarachnoid space (ventriculography and later pneumoencephalography), and sodium-iodine injected into the blood stream made it possible to visualize the cerebral vasculature (angiography). Cerebral angiography became easier and safer to perform in the 1960s and 70s using new and improved contrast agents and injections via the femoral artery instead of direct puncture of the common carotid artery. Pneumoencephalography was largely abandoned by the late 1980s due to pain and danger to the patient. Despite some improvements, x-ray imaging for neurosurgical planning and navigation was quickly replaced by other modalities such as computer tomography (CT) and magnetic resonance imaging (MRI) when they became available in the 1970s and 80s. The poor soft tissue

contrast, the loss of information in the direction parallel to the beam and the difference in magnification due to the diverging beam made the modality difficult, if not impossible to use for neurosurgical planning and navigation.

Computer tomography

True three dimensional imaging became possible with CT imaging in the early 1970s [37] and sparked new interest in the development of image-guided systems [5]. CT imaging, like conventional radiography, is based on the difference in absorption of x-rays in different tissue types. During CT scanning, a cross-section of the human body is probed with small x-ray beams from a number of directions. The x-rays are attenuated by the different structures inside the body and reach detectors on the opposite side of the patient. The recorded signals can be converted to projections of the linear attenuation coefficient distribution of the cross-section using the theory developed by Radon in 1917. CT imaging is widely used in spine surgery where the bony vertebrae are of primary interest. In brain surgery, MR imaging is often preferred due to superior soft tissue contrast and lack of radiation dose to the patient.

Magnetic resonance imaging

Magnetic resonance imaging is by far the most commonly used modality for neruosurgical planning and navigation. High resolution three-dimensional images with superior soft tissue contrast makes MRI the modality of choice in diagnosis, characterization and treatment of intra-cranial disease. MR imaging uses the principle of nuclear magnetic resonance to create images of the human anatomy and function [40]. Nuclei with an odd number of protons such as hydrogen-1, carbon-13 and nitrogen-15 possess a nuclear spin that describes their angular momentum. The nuclei used for conventional MR imaging is

hydrogen-1 due to its large concentration in water and fat, which are major constituents of the human body. In the presence of an external magnetic field B_0, these small magnetic dipoles line up with B_0 in one of two states: a low energy state, parallel to the external field, or a high-energy state, anti-parallel to B_0. The tissue magnetization exploited by MR imaging is due to a tiny excess of the population in the lower energy level creating a net magnetization vector parallel to B_0. An external oscillating electomagnetic pulse (RF pulse) can then excite the nuclear spins and the magnetization vector is rotated by an angle θ, called the flip angle. In absence of the RF field, the magnetization vector gradually "relaxes" to its equilibrium state emitting energy at the same radiofrequency (RF) . This relaxation process is exponential, and governed by the time constants T1 and T2 describing the longitudinal and transverse relaxation respectively. The differences in T2 and T1 between tissue types such as white matter, gray matter and cerebro-spinal fluid (CSF) are the source of contrast in the most commonly used MR imaging acquisitions. In proton density (PD) imaging, on the other hand, the observed intensity is weighted by the overall concentration of both aqueous and non-aqueous protons in tissue. Examples of typical transverse T1 weighted, T2 weighted and PD weighted MR images of a normal volunteer are shown in Figure 2–1.

Many pathologies such as brain tumors have relaxation times that differ from normal brain tissue, and can therefore be easily localized in MR images. A number of tumors can also be classified based on their appearance on T1 and/or T2-weighted images [35].

2.1.2 Functional imaging

Functional imaging can be an important supplement to anatomical imaging in neurosurgical planning [38]. Modalities like positron emission tomography (PET) and functional

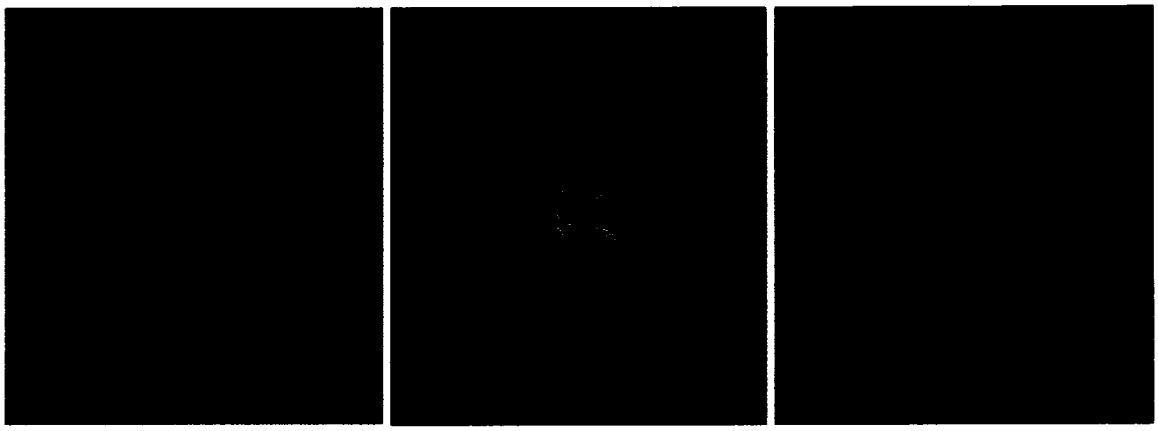

Figure 2–1: MR images of a normal volunteer: T1 weighted (left), T2 weighted (middle) and PD weighted (right).

magnetic resonance imaging (fMRI) make it possible to map functional areas surrounding the surgical target. One of the main goals of preoperative functional mapping is to evaluate the relationship between the target and eloquent cortical areas and thereby assess the feasibility of surgical treatment. This information can also be crucial in planning the surgery in order to minimize the risk of neurological deficits following the procedure. Other applications of pre-surgical functional imaging can be selection of patients for intra-operative mapping and finally guiding the procedure as a part of the information available in the neuronavigation system.

Positron emission tomography

PET imaging was the first functional imaging modality widely used for pre-surgical mapping. PET imaging is based on the fact that some atoms like carbon, oxygen, nitrogen, phosphorus and fluorine have isotopes that decay by positron emission [39]. The emitted positron will almost instantly combine with an electron and their masses are converted into two photons which travel in opposite directions. The resulting photons

can be detected and the position of the initial annihilation between the positron and electron can be computed. For the application to functional imaging, one of the isotopes mentioned above has to be injected into the patient's bloodstream or breathed by the patient. Depending on the isotope it will attach to compounds distributed according to particular functions such as glucose metabolism, cerebral blood flow (CBF) and blood volume (CBV) and oxygen consumption. The resulting PET images will give information about the radioactivity distribution within the brain and maps of activated brain regions can be produced by measuring the indirect effect of neural activity on CBF, CBV and glucose metabolism, for example. PET imaging can also be used to map functional areas eloquent to the surgical target.

Functional magnetic resonance imaging

Functional magnetic resonance imaging has some major advantages over PET imaging and has therefore quickly become the most widely used method for brain mapping in general, and mapping for surgical planning in particular. fMRI, is completely non-invasive and there is no use of ionizing radiation. Another great advantage of this imaging technique is that both functional and anatomical images can be obtained from the same modality and during the same imaging session. By far, the most widely used contrast mechanism used in fMRI studies is the blood-oxygenation-level-dependent (BOLD) contrast. A few seconds after cortical activation generated by a specific task (e.g. motor, visual, auditory or cognitive), a hemodynamic response occurs and the oxygen demand to the activated region increases. Oxygen to the activated cells is carried by the red blood cells (hemoglobin) and supplied from the local capillaries. The blood flow to the region increases in excess of the local demand, resulting in a dilution

of deoxygenated hemoglobin. Due to the difference in magnetic properties between oxygenated and deoxygenated hemoglobin, a signal increase can be observed around the venous vessels [40]. In neurosurgical planning, fMRI is used to map essential functional regions close to the surgical target or in the planned surgical path. An example of such mapping prior to surgery is shown in Figure 2–2.

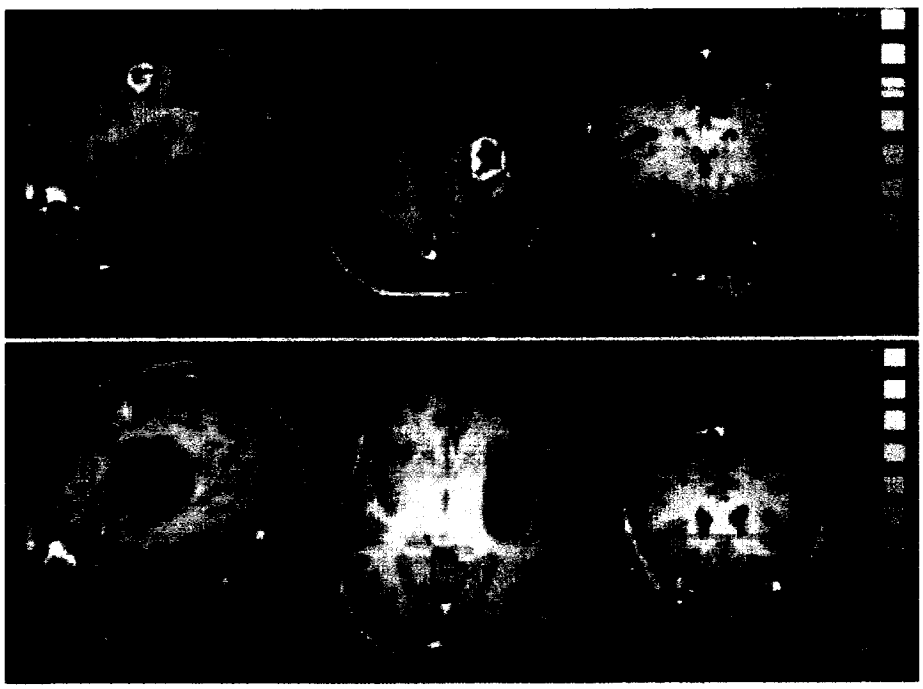

Figure 2–2: fMRI for neurosurgical panning in patients with brain tumors. (a) Activation map of motor stimulation of the right hand in a patient with a glioblastoma multiforme. (b) Activation map of word generation in a patient with a low-grade astrocytoma. Reprinted from "Functional magnetic Resonance Imaging at 3T as a Clinical Tool in Patients with Intracranial Tumors" by D. van Westen, G. Skagerberg, P. Fransson and E.-M. Larsson from Acta Radiologica, www.tandf.no/actaradiologica, 2005, vol 6, p. 599-609, by permission of Taylor & Francis.

2.1.3 Angiographic imaging

The main purpose of angiographic imaging is to map the cerebral blood vessels. This can be particularly important in cases directly involving the vascular nework such as stroke, aneurysms and arteriovenous malformations (AVMs), but can also be a valuable supplement to traditional anatomical and functional imaging in surgical planning for tumor resections, for example. Pre-operative angiographic imaging can give crucial information about blood vessels in the vicinity of the surgical target and thereby makes it possible to plan the surgery in order to avoid intersecting major vessels and ensure sufficient blood supply and drainage from all brain regions during and after the procedure.

Digital subtraction angiography

Digital subtraction angiography (DSA) is a two-dimensional x-ray technique. The method requires two acquisitions: one with a radio-opaque contrast agent injected into the patient's blood stream and one without. The subtraction of one image from the other results in a map of the cerebral vascular network. By acquiring multiple projections from different angles it is possible to build a three-dimensional model of the vasculature. One of the main problems with this imaging technique is patient movement between the two corresponding images, which can seriously reduce the useful signal. Other disadvantages of the modality are the radiation dose to the patient and the invasive injection of contrast agents. An example of a DSA image of the cerebral arteries is shown in Figure 2–3.

Computer tomography angiography

Like DSA, computer tomography angiography (CTA) requires the administration of a contrast agent prior to scanning, but produces fully three-dimensional images of the

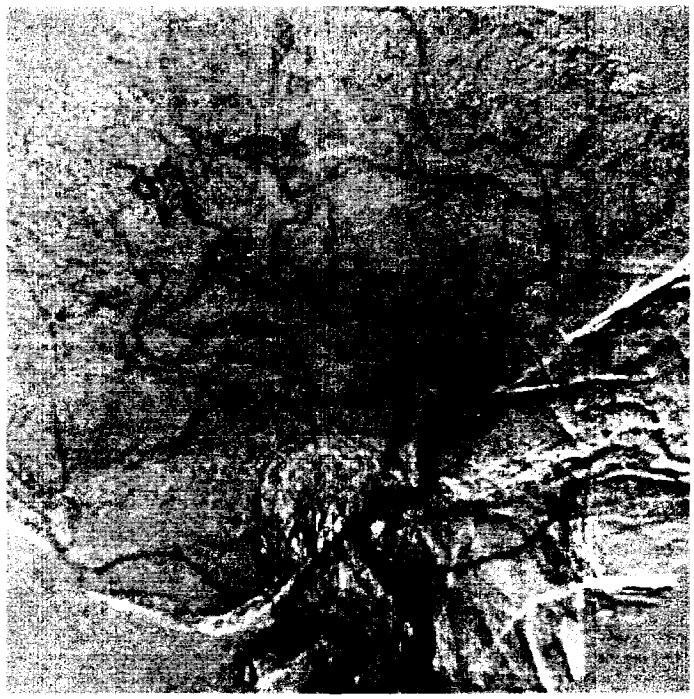

Figure 2–3: Contrast enhanced digital subtraction angiography of the cerebral arteries. Source: Image Sciences Institute (http://www.isi.uu.nl/Research/Gallery/DSA/)

patient, and is therefore better suited for use in surgical planning and navigation. CTA images can accurately reveal a number of vascular pathologies such as aneurysms and AVMs [42] and can be particularly useful in cases when the patient cannot undergo MRI scanning due to previously clipped aneurysms, for example. The radiation dose to the patient remains one of the main drawbacks with the modality.

Magnetic resonance angiography

The MR acquisition sequence can be designed to be sensitive to moving material within the body and thus produce images of the vascular network. Due to the noninvasive nature of the technique and the lack of radiation dose to the patient, magnetic resonance angiography (MRA) has become a commonly used acquisition in diagnosis and treatment of

patients with a number of intra-cranial pathologies. The two main imaging techniques currently used to produce angiographic images are Time-of-Flight (TOF) MRA and Phase Contrast (PC) MRA. TOF MRA uses repetitive pulses to suppress signal from stationary tissue [43]. The TOF MRA sequence uses a repetition time (TR) much shorter than the relaxation time of the longitudinal component of the magnetization vector. Because the longitudinal magnetization does not have the time to recover between excitations, the signal generated by the stationary brain tissue is very low. This state is called partial saturation. Blood flowing into the region is fully relaxed and therefore produces a strong signal that gradually decays to partial saturation. The result is a high contrast between fully relaxed blood (bright) and partially saturated tissue (dark). The main limitation of this technique is the signal loss experienced as blood flows deep into the imaging volume. A solution to this problem can be to acquire a sequential series of 2-D images. This results in a limited axial resolution and a lower signal-to-noise ratio (SNR). A compromise between 2-D and 3-D images is the multiple overlapping thin slab acquisition (MOTSA) technique.

Phase contrast (PC) MRA creates a vascular contrast by manipulating the phase of the magnetization vector. The motion of the magnetization vector in the direction of an applied magnetic field gradient induces phase variations [43]. There are many sources of phase variation not related to flow, so in order to acquire images which are only dependent on motion, two measurements are necessary : one reference scan and one scan where the gradient along one direction is modified. It is also necessary to select a velocity range for the phase-encoding. This range might be on the order of 60-80 cm/s for selective imaging of arteries and close to 20 cm/s for imaging of veins and sinuses.

The difference between the images with and without the velocity-encoding gradient will be dependent only upon the motion along the direction of that gradient. In order to measure motion along all directions, four scans are therefore necessary. From these data it is possible to obtain quantitative velocity images by forming a phase difference image between measurements. Angiograms can also be obtained by displaying the magnitude of the different images. PC MRA does not suffer from signal loss when the blood flows deep into the imaging region and is therefore well suited to image the venous and arterial systems simultaneously. MR angiograms and anatomical MR images are acquired at the same time and are therefore inherently registered. This is a great advantage for neurosurgery planning. The main limitation is a relatively long acquisition time due to the number of scans. In order to decrease acquisition times, resolution is often compromised. Another limitation is velocity aliasing which occurs when true velocities exceed the pre-defined velocity range. Flow can then incorrectly be shown as being in the opposite direction. PC MRA is often the best solution when an angiogram of the entire brain along with an anatomical image are required for surgery planning. When only a detailed view of arterial anatomy is needed, TOF MRA is most often preferred. Examples of PC MRA and TOF MRA of a normal volunteer are shown in Figure 2–4. The last and most invasive MRA technique widely used in neurosurgical planning is Gd-enhanced T1-weighted imaging. By injecting a gadolinium (Gd)-based contrast agent into the patient's blood stream, the T1 of the blood is shortened compared to the surrounding tissue [44]. A standard T1-weighted MR sequence can then be applied to image the vascular network. MRI contrast agents are also widely used to delineate pathological structures associated with the breakdown of the blood brain barrier.

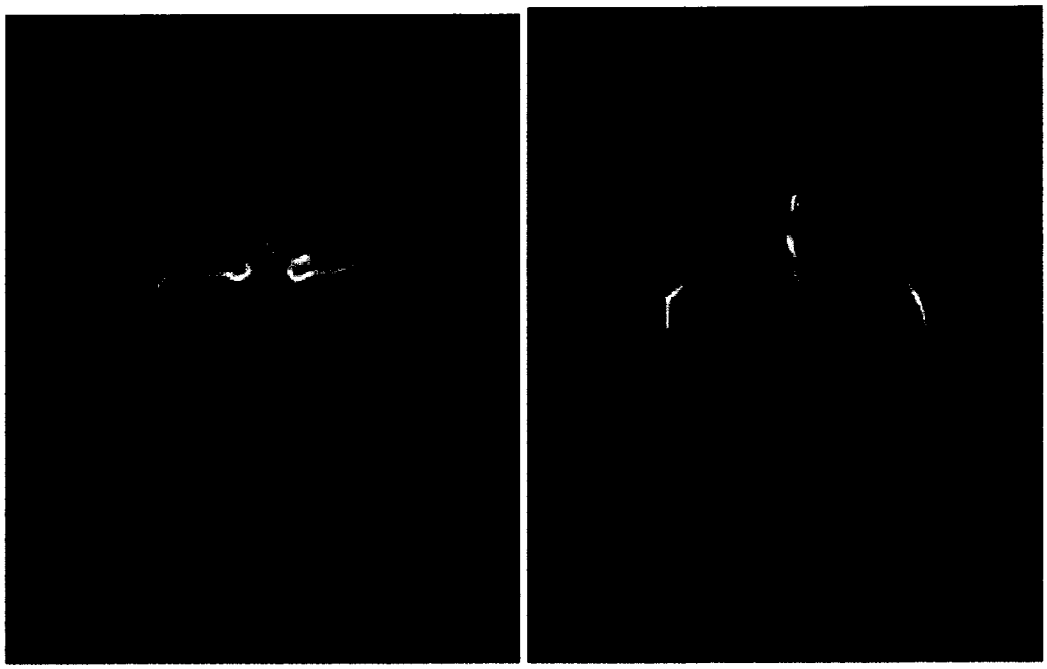

Figure 2–4: Transverse maximum intensity projection of two MRA volumes of a normal volunteer: Time-of-flight (left) and phase contrast (right).

Disruption of the blood brain barrier is known to be associated with malignant tumors, inflammatory demyelinating disease and ischemia, for example. When compared to DSA, all MRA techniques are limited in resolution.

2.2 Navigation systems

In order to take advantage of the complementary information in the pre-operative images from different imaging modalities, all available data-sets have to be imported into the navigation software and visualized in the same coordinate system. A typical software is capable of displaying three-dimensional cross-sections of single or fused data-sets, surface/volume renderings and segmented structures in addition to the position and orientation of the computer tracked tools. Other key components of the navigation

system are a tracking system (e.g. infrared, acoustic or magnetic sensor), a reference mounted on the operating table and one or more tools with tracking devices attached. The different components of a typical neuro-navigation system and the spatial transforms required to achieve tracking and guidance are shown in Figure 2–5.

The overall accuracy of a neuronavigation system is the sum of the errors associated with each individual step required to reach image guidance [6, 9]. The first step in this process is pre-operative imaging of the patient. MR and CT imaging have been compared in the context of neuro-navigation [10, 11, 9], and it was demonstrated that CT imaging slightly increased the localization error. Due to other important advantages of MR imaging compared to CT discussed previously, MR imaging is the most commonly used modality for pre-operative imaging. However, geometric distortions due to field inhomogeneities and non-linear gradients may cause errors in the way the patients anatomy is represented in the MR images [12]. The resolution of the pre-operative images will also influence the navigation accuracy [9].

The next step in the process is performed in the operating room prior to opening of the skull. When the patient has been immobilized on the operating table and a computer tracked reference has been attached to the table, the pre-operative images have to be registered to the patient. This step can be performed by identifying a series of homologous points on the patient's head and in the pre-operative images (anatomical landmarks), by using fiducial markers glued to the patients skin prior to MR imaging, by using various surface matching techniques, by using a stereotactic frame applied prior to imaging and maintained during surgery or by using markers attached to cranial-implanted screws [5, 13]. Mascott et al. [13] demonstrated that the highest accuracy is obtained using

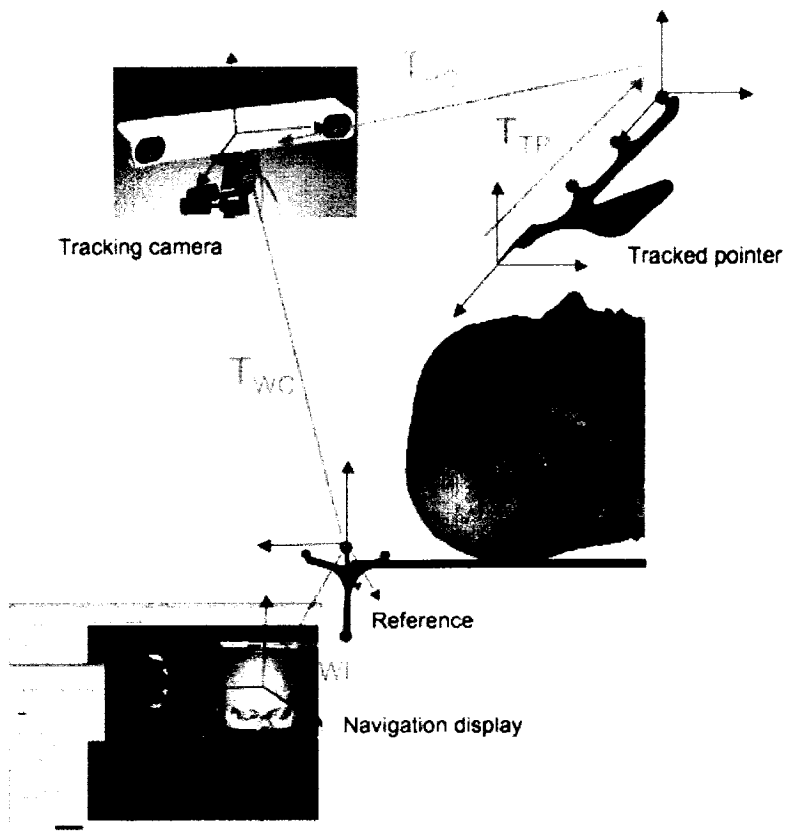

Figure 2–5: The different components of a typical neuro-navigation system and the spatial transforms required to enable tracking of an intra-operative tool and thus reach image guidance. T_{TP} relates the origin of the pointer to the pointer tip. This transform has to be determined using a calibration procedure. T_{PC} is the spatial relationship between the tracked instrument and the tracking camera. T_{WC} is the transform between the reference (world) and the tracking camera. These two transforms are connected in the sense that the tracking system gives the position of the tracked instrument relative to the reference. This means that the camera can be moved during surgery without consequences for the navigation system as long as the reference stays firmly attached to the operating table. T_{WI} is the transform between image space and the patient (world) coordinate systems. This transform has to be estimated at the beginning of the procedure using either a point or surface based matching technique.

implanted markers (up to 2 mm), and the lowest accuracy is obtained using anatomical landmarks (over 5 mm in some cases). In cases where anatomical landmarks, fiducial markers or implanted markers are used, the calibration of the computer tracked pointer used for point identification on the patient's head and the precision and accuracy of the tracking system are important for the accuracy of the registration. In addition, the manual identification of points both on the patient's head and in the pre-operative images, is associated with an operator dependent error. Following point selection, an automatic algorithm is used to estimate the rigid transformation between the pre-operative images and the patient. The error associated with the applied algorithm also affects the overall accuracy of the system. Ideally, the surgeon can now localize any point in the patient's brain on the pre-operative images by using a computer-tracked probe. However, the calibration of this probe and other computer tracked instruments, and possible displacement between the patient and the reference will also contribute to the navigation error.

In ultrasound based navigation systems [14, 15, 16], the errors associated with this imaging modality will add to the errors described above. In particular, the calibration of the ultrasound probe is a major source of error in these systems [6]. The spatial calibration of the ultrasound probe determines the spatial transformation between the ultrasound image plane and the tracking device attached to the ultrasound probe. This transformation has to be determined prior to surgery in a controlled laboratory setting. A number of different techniques have been presented in the literature in order to estimate this transform as correctly as possible [17, 18, 19, 20, 21, 22]. Most calibration techniques are based on imaging of a phantom with known geometry. The manual or automatic identification of points or lines in the ultrasound images then allows the

determination of the calibration parameters. The error associated with ultrasound probe calibration is in most systems on the order of 1-2 mm [6].

The ultrasound image plane has to be accurately localized in three-dimensional space, but also in time. Temporal calibration consists of estimating and correcting the difference between the timestamp of the tracking system and the timestamp of the ultrasound image. If this difference is important and not accounted for, it might lead to errors in 3-D quantitative measurements in general, and in ultrasound based neuronavigation in particular. Several methods have been developed in order to estimate this time difference for particular ultrasound systems [23, 24, 25]. Rousseau et al. [25] showed that a small time difference of about 40 ms does not introduce a considerable error into a volume estimation from reconstructed 2D ultrasound images. Larger latencies on the order of 200 ms, on the other hand caused an inaccuracy of 5% in a 3-D volume estimation.

Another possibly important source of error in ultrasound based systems is the difference in speed of sound in brain tissue and the speed of sound used by the ultrasound scanner to reconstruct 2D images. The average speed of sound in soft tissue and thus the value used by most ultrasound scanners is 1540 m/s. For brain tissue the average value is 1568 m/s at 37° and 5 MHz, but large variations occur between tissue types such as cysts and tumors, for example. In extreme cases, the error associated with the speed of sound may reach more than 2 mm [6]. Finally, the 2D ultrasound slices have to be reconstructed into a regular 3D volume. The reconstruction of irregularly spaced two-dimensional ultrasound images into a regularly spaced three-dimensional volume has been the subject of a number of studies. A reconstruction technique should not introduce artifacts, distort or degrade the images. The reconstruction should also be reasonably fast to compute in

order to be well suited for intra-operative use. Current methods presented in the literature include nearest neighbor interpolation [26], interpolation weighted by some function of the distance [27, 28, 29], interpolation using radial basis function interpolation [30], non-rigid registration [31], Rayleigh model for the intensity distribution [32] and methods using the probe trajectory [33].

A number of groups have investigated the overall accuracy of different ultrasound-based neuro-navigation systems. Lindseth et al. [6, 7] estimated an accuracy of less than 2 mm for navigation based on a recently acquired ultrasound volume. Jodicke et al. [34] reported a localization error of 2.26 mm using images imported from an external ultrasound scanner into the navigation system.

An additional and in many cases important source of error in neuronavigation systems is the brain displacement and deformation during the operation. The brain surface and also internal structures may shift more than 10 mm compared to their positions during pre-operative imaging. Accurate navigation using pre-operative images will therefore only be possible if such displacements are detected and corrected. This issue and possible solutions will be described in more detail in the next section.

2.3 Brain-shift

A significant source of error in neuronavigation systems is brain tissue movement and deformation, so called brain-shift, during the surgical procedure. Tissue movement can be caused by gravity, drainage of cerebro-spinal fluid, retraction and resection of tissue, swelling of brain structures, and administration of drugs. The amount of movement and its influence on the accuracy of the neuro-navigation system depends on a number of

factors including surgical target size and location, craniotomy size and patient position during surgery.

The magnitude and direction of brain deformation during surgery have been the subject of several studies. The first quantitative measurements of brain deformation during surgery relied on recordings of points on the cortical surface relative to fixed points on the cranial surface [55, 56]. These studies showed a cortical surface shift of 10 mm on average, and movement was found to be greatest along the direction of gravity.

To better describe the dynamic process of brain deformation, several groups have used intraoperative MRI (iMRI) to study brain shift [57, 58]. The results show that surface shift ranges from almost no detectable shift for smaller lesions to up to 50 mm for larger lesions. Surface shift well beyond the craniotomy has also been documented. As in the previously discussed studies it was found that surface shift was mainly due to loss of cerebro-spinal fluid and resulted in a shift in the direction of gravity. They also showed that surface shift occurs throughout the procedure while deformation of deeper structures occurs mainly during resection. Volume changes depend on the nature of the surgical procedure, and are in general greater for resection cases than for biopsies and functional interventions. The principal direction of displacement was not always aligned with the direction of gravity.

Intraoperative ultrasound has also been used to estimate brain-shift. Letteboer et al. [59] used ultrasound to measure the linear component of the shift at the tumor boundary. This study also confirms the assumption that the brain deforms mainly in the direction of gravity is not always valid.

In summary, the cortical surface shift is mainly caused by loss of CSF and subsequent "sinking" of the brain in the direction of gravity. Surface shift can occur well beyond the borders of the dural opening and can occur throughout the procedure. However, the surface has been shown to settle in cases where the resection cavity is smaller than the cortical opening. If the cavity is larger than the cortical opening, the borders sink in to form a crater. Deformation of subsurface structures on the other hand is mainly due to resection, relief of weight and intraparenchymal pressures. Larger deformations are generally observed in the hemisphere ipsi-lateral to the lesion, but significant deformations can also occur in the contra-lateral hemisphere [58].

2.4 Intra-operative imaging

2.4.1 Intra-operative CT imaging

A few groups have used intraoperative CT to actualize the navigation data and verify the anatomical situation during surgery [60, 61, 62, 63]. The CT images can be used to localize intracranial lesions, but suffer from lower soft tissue contrast than MRI, and are therefore less useful for brain surgery. CT imaging is more commonly used in spine surgery, where the vertebrae and surrounding structures are of primary interest. Other disadvantages of intraoperative CT imaging are the radiation dose to the patient which limits the number and duration of the scans, and the physical space occupied by the scanner in the operating room.

2.4.2 Intra-operative MR imaging

Intraoperative MRI (iMRI) scanners can provide the surgeon with updated anatomical images several times during a procedure, and can therefore be a valuable tool for characterization and correction of brain shift. One of the first reports on the use of

iMRI for neurosurgical guidance was presented by Black et al. [64]. They illustrated the advantages of intraoperative MRI imaging in a series of 60 craniotomies for tumor resection. Images were acquired before and after opening of the dura and after closure of the craniotomy. Nimsky et al. [65] went one step further and used intraoperative data for registration purposes. Intraoperative MR images were rigidly registered to the pre-operative data using MR-visible fiducials placed around the craniotomy. The root mean square position error after registration was reported to be between 0.39 mm and 2.3 mm. Even though intra-operative MR imaging provides good quality images in reasonable time, this solution suffers from a number of disadvantages [68, 69]. Intra-operative MR imaging is a complex, expensive and sometimes quite time consuming procedure. The intraoperative images may be of poorer quality than pre-operative MR images due to scanner design and short acquisition time. In general, intraoperative images are less complete, have lower resolution and are more susceptible to image distortions due to inhomogeneous magnetic fields when compared to pre-operative images. Another major shortcoming of this solution is the substantial financial investment required for the scanner as well as MR-compatible surgical instruments. These investments are justifiable for only a very limited number of hospitals. In addition, interventional MR scanners are space-consuming and in many cases compromise the surgeon's access to the operating field. So far, no study has demonstrated a clear benefit to the patient using intra-operative MRI. This is mostly due to the difficulty in setting up a controlled study and also the difficulty of doing post-hoc analysis.

2.4.3 Ultrasound imaging

Intraoperative ultrasound imaging does not suffer from many of the limitations associated with interventional MRI. A high-end ultrasound scanner costs less than 10% of a typical MRI system and is already in use by many neurosurgeons. In addition, ultrasound systems are portable and compatible with existing surgical equipment. Despite these advantages, the use of ultrasound in neuro-navigation has been limited, probably due to poor image quality and the difficulty of interpreting such images.

Ultrasound imaging is based on emission and reception of sound waves [70]. Sound with a frequency of 20,000 Hz or higher is called ultrasound and the range of frequencies employed for most diagnostic ultrasound applications is 2 to 10 MHz. The usefulness of ultrasound as an imaging modality is primarily the result of reflection and scattering of the incident ultrasound pulses at tissue boundaries, and scattering within heterogeneous tissues. At a given boundary, the intensities of the reflected and transmitted sound depend on the incident intensity and the acoustic impedances of the media. From the ultrasound transducer, a great number of pulses travel out in different directions. When the echoes return to the transducer, their travel time and intensity are registered. If the propagation speed is known, the travel time of the echo gives the position of the reflecting point in the medium along the axis of the emitted pulse. The intensity of the echo gives the brightness of the pixel at that position. A high intensity echo means that the reflecting boundary separates two media with very different acoustic impedances. The acoustic impedance Z is given by:

$$Z = \rho c \tag{2.1}$$

where ρ is the density of the material and c is the speed of sound in the medium.

By combining the information from a number of pulses emitted in different directions, a B-mode (Brightness-mode) image can be constructed. Ultrasound B-scans are grey-scale images of tissue cross sections and can be produced in nearly real-time (10-60 frames per second). This imaging mode permits imaging of the motion of moving structures as well as static (freeze-frame) images. Ultrasound imaging has been used in neurosurgery since the early 1980's in order to guide the surgeon and localize lesions within the brain during surgical procedures [5, 46, 45]. However, ultrasound imaging is usually not part of the neuro-navigation system and if ultrasound is used, it is left to the surgeon to combine the information from the pre-operative MR or CT images from the neuro-navigation system and the intraoperative ultrasound images. The use of ultrasound in this context is non-trivial and requires experience in interpretation of ultrasound images. When ultrasound images are incorporated into the neuro-navigation system and displayed, for example together with the corresponding MR or CT slice, the interpretation of the ultrasound data is facilitated and the usefulness of the imaging modality largely increased [14]. Although the interpretation is easier with ultrasound built in to the neuronavigaton system, it is still up to the surgeon to compare the two images and determine if significant brain-shift has occurred. The information from the ultrasound images will be even more useful if it could be used to update the pre-operative data, which has higher image quality and is easier to interpret.

This is the main motivation behind the work presented in this thesis, and the goal of this project is to present updated images to the surgeon which may be used to guide the intervention.

2.4.4 Doppler ultrasound imaging

The Doppler effect is named after Christian Andreas Doppler (1803-1853), and is the perceived difference between the frequency emitted by a source and the frequency observed by a receiver whenever there is a relative motion between the two. An example of a source of waves moving to the left is shown in Figure 2–6.

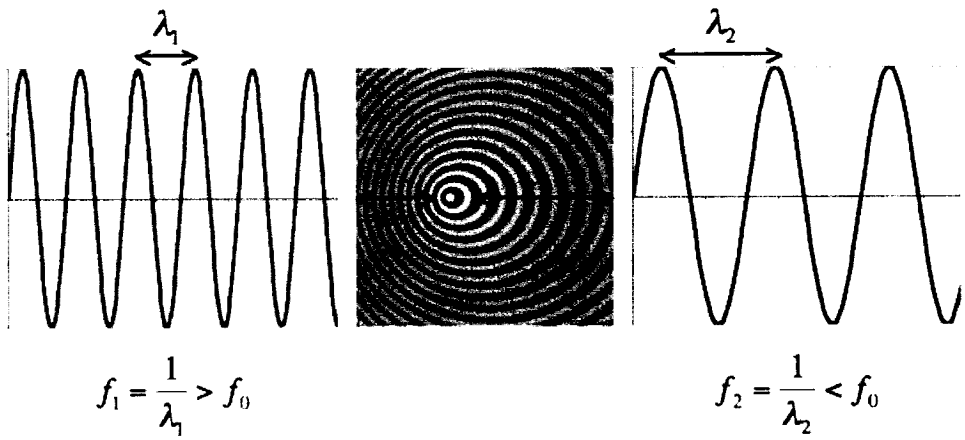

Figure 2–6: A source of waves moving to the left. The frequency is higher on the left and lower on the right. f_0 is the frequency emitted by the source, f_1 and f_2 are the perceived frequencies to the left and to the right respectively and λ_1 and λ_2 are the corresponding wavelengths. (Source: Adapted from http://en.wikipedia.org/wiki/Doppler-effect).

The apparent change in frequency is given by the Doppler equation:

$$f_D = f_0 - f_e = \frac{2 f_0 v \cos\theta}{c} \tag{2.2}$$

The Doppler shift f_D is defined as the difference between the operating frequency f_0 of the transducer and the echo frequency f_e. It is proportional to the emitted frequency f_0, the speed of movement v, the speed of sound c and the Doppler angle θ. The Doppler

angle is the angle between the sound propagation and the blood flow direction as shown in Figure 2–7.

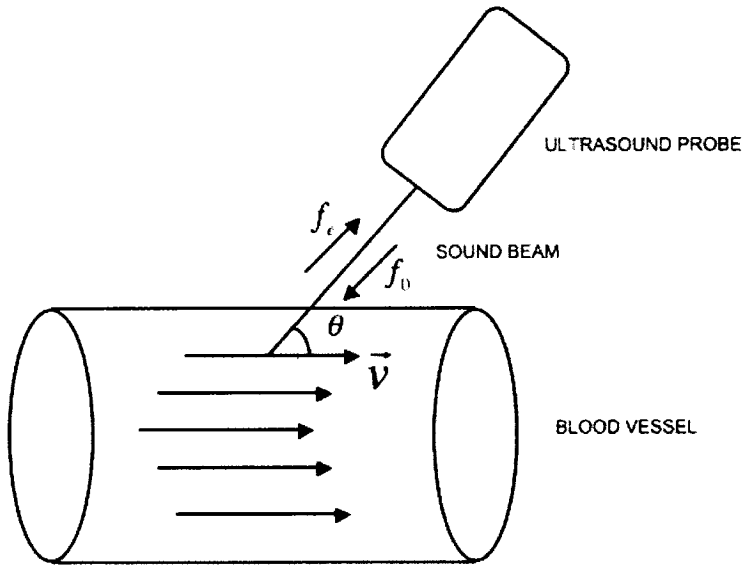

Figure 2–7: Schematic diagram showing the different parameters that influence the Doppler shift.

Due to the dependence on the angle θ, the speed of flow calculated from the observed Doppler shift is only as accurate as the estimated Doppler angle. Usually, Doppler information is superimposed on real-time gray-scale anatomic cross-sectional images. Flow directions toward and away from the transducer (positive and negative Doppler shifts) are presented as different colors on the display. This technique is called color Doppler imaging. An example of a color Doppler image of some of the branches of the middle cerebral artery (MCA) is shown in Figure 2–8.

Power Doppler imaging, on the other hand, depicts the amplitude, or power, of Doppler signals rather than the frequency shift. This allows detection of a larger range of Doppler

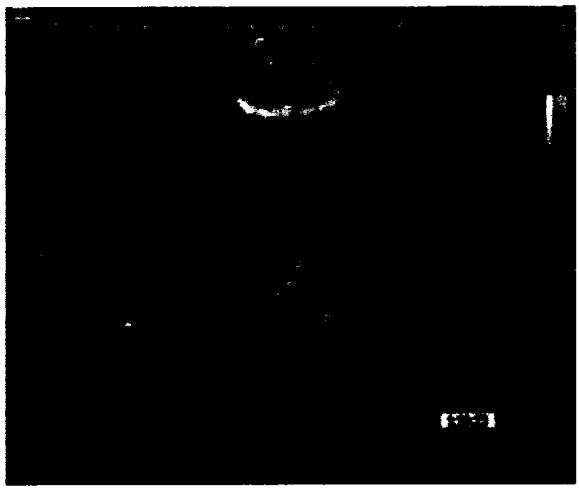

Figure 2–8: Color Doppler image of some of the branches of middle cerebral artery (MCA) of a patient who underwent neurosurgery to remove a brain tumor. The Doppler signal is superimposed on the gray-scale B-mode image.

shifts and thus better visualization of small vessels, but at the expense of directional and velocity information.

In the context of neurosurgery, Doppler ultrasound imaging is useful in detecting and quantifying the presence, direction, speed and character of blood flow in the cerebral vasculature. Doppler ultrasound scanning provides the neurosurgeon with a simple and cheap possibility of direct intraoperative visualization of pathological and normal vasculature. It can be used to characterize tumors' vascularization, artery venous malformations (AVMs) and aneurysms, for example.

2.5 Image registration for correction of brain-shift

2.5.1 Deformable models

With all this prior knowledge about how the brain shifts and deforms during surgery, a number of groups have developed model-based techniques to try to correct for the displacements. Among the first groups to attempt this approach was Miga et al. [47]. The

technique was applied to four neurosurgical cases, and it was found that the model could account for 79% of the gravity induced deformations on average. Other groups have extended this work to include more complex deformations and deformation of deeper structures [56, 48]. These studies are based on a number of assumptions about the brains mechanical properties and about the localization and extent of brain deformations. It was assumed, for example, that brain tissues are isotropic, homogeneous and with identical density and stiffness. It was also assumed that there is no deformation in the hemisphere contralateral to the craniotomy, and that all deformations can be estimated based on data from the exposed surface.

In general, the displacement and deformation of the brain during surgery is far more complex and far reaching than these models assume, and more work is needed to estimate the mechanical properties of the brain [49] in order for this type of approach to be useful in more than a very limited number of neurosurgical procedures.

The more direct solution to the problem is to acquire new images when significant amount of deformation is suspected. The most popular intraoperative imaging modalities for neurosurgery are intraoperative CT, intraoperative MRI, and intraoperative ultrasound (US) imaging.

2.5.2 MR-to-MR registration

A point based registration method using intra-operative MR was presented by Nimsky et al. [65]. Intraoperative MR images were rigidly registered to the pre-operative data using MR-visible fiducials placed around the craniotomy. The root mean square position error after registration was reported to be between 0.39 mm and 2.3 mm.

An image based registration algorithm for iMRI was presented by Ferrant et al. [66]. A biomechanical finite element (FE) model driven by surface correspondances was used to estimate the deformation of the entire brain during surgery. The accuracy of the registration was evaluated using manually identified landmarks and resulted in a mean error of less than 1.6 mm. A second image-based registration technique was published by Hastreiter et al. [67]. After having characterized the brain deformations, they used a non-linear registration method based on mutual information to register pre-operative and intra-operative data. The registration process made it possible to register pre-operative functional data such as fMRI, PET and MEG to the intraoperative MR images.

2.5.3 US-to-MR registration

Since the mid-1990's a number of groups have developed systems correlating intraoperative US with pre-operative MR. In a neurosurgical context, intraoperative ultrasound imaging can either be used directly as a surgical guide when brain-shift occurs or as a registration target for the pre-operative images in order to correct for deformations. These systems are described in more detail in the following sections.

Direct ultrasound navigation

Grønningsæter et al. [14] developed a neuro-navigation system based on navigation solely by 3D ultrasound. This system also incorporates visualization of pre-operative MR and/or CT images, but uses only intra-operative 3D ultrasound for navigation if brain deformation occurs. Navigation by ultrasound images requires high quality images and display software in addition to well trained surgeons and technicians.

Manual registration of intraoperative ultrasound

Intra-operative ultrasound data can also be used in a less direct manner. Image registration techniques can be used to update pre-operative data. By registering pre-operative MR or CT images with intra-operative ultrasound images, complex deformations can be estimated and accounted for in the navigation system. For example, by identifying anatomical landmarks in the US images, and using a physical model of the brain, an elastic transformation can be calculated and applied to the pre-operative data. Comeau et al. [18] presented a surgical guidance system that incorporated pre-operative images with intraoperative ultrasound to detect and correct for brain-shift during neurosurgical procedures. Two dimensional ultrasound images were acquired during the operation and compared to the corresponding slice from the pre-operative data set. A method was presented to manually identify homologous landmarks in ultrasound and MRI in order to construct a set of displacement vectors that would allow the pre-operative MR image to be warped to match the intra-operative ultrasound image. The mapping procedure was demonstrated to have an accuracy better than 2 mm. Gobbi et al. [71] demonstrated a similar technique where manually placed landmarks and a thin-plate spline interpolation were used to deform the MR volume to match the ultrasound volume.

Automatic registration of intraoperative ultrasound

Several automatic registration procedures have also been developed, in order to minimize the need for user intervention and speed up the procedure, which is particularly important for intraoperative registration. Roche et al. [52] estimated the rigid body transform required to linearly align pre-operative MR images and intra-operative US images. They correlated the US intensities with both the MR intensity and the MR gradient magnitude

using a variant of the correlation ratio and a robust distance measure. The algorithm was tested on two clinical datasets and one phantom dataset. Because the ultrasound probe was not tracked during imaging, and no gold standard for the registration was available, registration loops involving both the ultrasound and MR data were used. A registration loop is a series of transform compositions that in the ideal lead to the identity matrix. They reported the standard deviations for the registration loops that corresponded to the residual rotation and the residual translation. Values up to 1.65 mm in translation and 1.57° in rotation were reported.

In order to correct for non-linear deformation Arbel et al. [50, 51] used a tracking system to reconstruct 3D volumes from a series of US images in the same space as the pre-operative MR-image. From the pre-operative MR images, they created pseudo-US images that closely resembled real US images of the same structures acquired during surgery. They then used an intensity based non-linear registration technique to match tracked intraoperative US images with the pseudo-US images to detect and correct brain deformations. Qualitative results from 12 surgical cases showed that the technique was able to account for a large portion of the deformations.

Registration of intraoperative US with pre-operative MR is a challenging registration problem due to very different underlying physical principles and thus different image characteristics. Image intensities, noise characteristics, contrast, volume coverage and dimensionality are only a few main differences between a typical pre-operative MR image and a corresponding intraoperative ultrasound acquisition.

2.5.4 Vessel-based registration

To try to overcome some of the difficulties discussed in the previous section, we explore a different approach to this particular registration problem. The idea is to use homologous features in the two datasets as "landmarks". Such features might be any segmented structures, such as organ surfaces and vascular structures present in both images. In this project we investigate the use of blood vessels segmented from pre-operative angiographic images and Doppler US for registration purposes. The cerebral vasculature is relatively easy to identify and segment from pre-operative angiographic data such as MR angiograms (MRA). A method to segment vessels from other types of MR aquisitions such as proton density (PD) images or gadolinium (Gd) enhanced MR images has been presented in [72]. Segmentation of Doppler ultrasound images can easily be performed by simple thresholding although this often produce vessels with a too big radius due to noise from moving vessel walls. By using the centerlines of the vessels this problem is largely overcome.

The cerebral vasculature is a good candidate for use in image registration because the vessels are distributed all over the cerebral cortex and inside the brain and move with the surrounding tissue. The brain deformations are therefore well captured by the vasculature. In addition, blood vessels will be present in any region of interest (ROI) throughout the brain. The probability of not finding reliable landmarks in a given ROI is therefore low. Keeping track of important vessels during surgery also provides the surgeon with important reference points in order to avoid major vessels during the procedure and monitor blood supply to specific areas of the brain. This approach has already been investigated by a number of different groups for several different purposes.

Porter et al. [73] rigidly registered MRI with B-mode and color Doppler ultrasound volumes based on segmented blood vessels from the forearm, the liver and a prostate phantom. The skin surface, bone and internal landmarks were used to evaluate the registration error which ranged from 2 to 8 mm.

Another rigid body registration technique based on vasculature was presented by Slomka et al. [74]. The carotid bifurcation of six patients was imaged with B-mode and Power Doppler ultrasound as well as MRA. The mean errors were 0.32 mm in translation and 1.6° in rotation based on a series of anatomical landmarks for initial misalignments of up to 5.4 mm in the x and y directions, 10 mm in the z direction and rotations up to 40°. The algorithm was not affected by missing arterial segments of up to 8 mm, but would fail if the bifurcation was missing from either dataset.

A third rigid body registration technique as well as a vessel segmentation algorithm was presented by Aylward et al. [75]. A registration metric was defined based on the parameters of the vessel segmentation algorithm and used to register CT images of the liver, pre and post-surgery MRA images of the brain. A series of Monte Carlo simulations was conducted to measure how consistently the registration method was able to align segmented vessels from the liver given random initial misregistrations. The application of this registration algorithm was extended to include CT to ultrasound registration [76] and then further extended to take into account non-linear deformations [77]. Following global rigid registration, each branch in the vessel tree was linearly registered resulting in a piece-wise rigid transformation. The alignment was then further refined with a deformable registration method. The results showed that the 87% of the centerline points in the model were within 2 voxels of the centerlines in the target image.

A more recent technique to register MR and B-mode ultrasound images of the liver based on vasculature was presented by Penney et al. [78]. The rigid registration used ultrasound images to establish the correspondence between the MR volume and the patient on the operating table. This corresponds to the rigid registration usually performed by identifying homologous landmarks on the patient's head and on the pre-operative images before neurosurgical procedures. The results showed that the method was accurate to within an RMS error of between 2.3 and 5.5 mm with respect to a "bronze standard" registration calculated by manually picking points in both modalities.

The algorithm described in this thesis is designed to register pre-operative MR images and intra-operative US images of the brain in order to correct the brain-shift occurring during neurosurgical procedures. The technique uses segmented vessel centerlines from MRA and Doppler ultrasound data to drive the registration with the assumption that the movement and deformation of the vasculature accurately captures the displacement of surrounding brain tissue. A modified version of the ICP algorithm has been implemented and tested with both linear and non-linear transformations. In order to reduce the number of outliers, the least trimmed squares (LTS) robust estimator [112] has been incorporated. Therefore, the method effectively reduces the number of incorrect pairings without limiting the capture range of the registration algorithm. While the algorithm shares some similarities with the procedure described by Lange et al. [79], there are some important differences. The procedure presented in this thesis is applied to interventional brain imaging, while Lange's technique was applied to liver. Both techniques use segmented vessel centerlines to drive the registration. While the technique proposed in this thesis uses LTS robust estimation to reject outlier points, Lange proposes a

user-defined distance threshold. Both techniques use spline-based regularization of the deformation; in this thesis a thin-plate spline is used, while Lange uses B-splines. Finally, Lange estimated the quality of registration quantitatively based on the RMS distance of vessel-points and semi-quantitatively based on structure boundaries. One of the main contributions in this thesis is a more thorough quantitative validation using data with simulated deformations and real MR and US data from a novel deformable anthropomorphic poly vinyl alcohol cyrogel (PVAc) brain phantom [54].

Chapter 3

Methods

In this chapter, the vessel-based image registration technique is described in detail. This chapter is a more complete version of the methods section in Chapter 5. The informed reader can therefore skip this chapter without loss of information. The validation of the method using numerical simulations, phantom data and real patient data is presented in subsequent chapters.

3.1 MR vessel segmentation

MRA is one of the most commonly used modalities to study the cerebral vasculature. As mentioned previously, the non-invasive nature of the procedure and the lack of radiation dose to the patient makes the modality well suited for detection of vascular pathologies and surgical planning. While the simplest and fastest segmentation technique consists of intensity-based thresholding of the original data, this may not be sufficient in situations with high background noise, for example. A number of more sophisticated segmentation techniques have therefore been proposed in order to extract the vessel information from

the MRA images in order to create three-dimensional models of the cerebral vasculature. These methods can be divided into five categories: deformable models, statistical analysis methods, knowledge-based methods, artificial intelligence methods and multi-scale filtering methods. While a complete review of MRA segmentation techniques is beyond the scope of this section, examples from each of the categories are given below.

Deformable models used in vessel segmentation are curves or surfaces that evolve iteratively to optimize some error criterion based on intensity values and/or vessel shape. Lorigo et al. [80] presented a method using a level-set implementation of active contours to segment MRA images of the aorta and the brain in addition to CT data of the lung.

Statistical analysis methods use different statistical distributions to model both background signal and vessels. An example was presented by Hassouna et al. [81]. They used a Rayleigh distribution and two normal distributions to model the background noise and one normal distribution to model the blood vessels. The parameters of the probability density function were then estimated and segmentation was achieved using maximum a posteriori classification.

Knowledge-based techniques integrate a priori knowledge about the anatomy in the segmentation process. Passat et al. [82] created a vascular atlas from 18 PC MRA and used it to estimate the parameters of adaptive sets of gray-level hit-or-miss operators.

Yet another approach to this segmentation problem is using artificial intelligence methods. Kobashi et al. [83] used watershed segmentation and an artificial neural network to segment vessels from TOF MRA data.

Finally, multi-scale filtering techniques use the analysis of the Hessian matrix to characterize vascular structures. Krissian et al. [84] used multi-scale filtering followed

by reconstruction of the vessel centerlines and radii. The segmentation method applied in parts of this thesis is also based on multi-scale filtering. The method can be summarized in three steps: First, the method applies Frangi's vesselness measure [91] to find putative centerlines of tubular structures along with their estimated radii and orientation. Second, this multi-scale measure was distributed to create a vector field which was orthogonal to vessel boundaries. Finally, the flux maximizing flow algorithm [92] was applied to the vector field to recover the vessel boundaries. This technique overcomes many limitations of existing approaches in the literature specifically designed for angiographic data due its multi-scale tubular structure model. It has a formal motivation, is topologically adaptive due to its implementation using level set methods, is computationally efficient and requires minimal user interaction. The technique is detailed in [72].

3.2 US vessel segmentation and volume reconstruction

When scanning using Doppler ultrasound imaging, the Doppler signal and the B-mode signals are combined on the display of the ultrasound scanner. The Doppler signal is displayed in color, and the B-mode signal is displayed in grayscale. Segmentation of the ultrasound images was therefore obtained by extracting all colored pixels from the original images. A simple filter was implemented that would set to zero all pixels with a saturation equal to zero (Hue-Saturation-Value color model), which constitutes the grayscale. Following segmentation, the 2D images were masked, converted to grayscale, and finally reconstructed onto a uniform three-dimensional grid using a Kaiser-Bessel function as the interpolation function and an isotropic regrid radius of 2 mm. The 3D volume was then blurred using a Gaussian kernel with a FWHM of 1 mm and

Figure 3–1: An example of an color Doppler ultrasound image before and after segmentation (right and middle) and after masking (left).

thresholded again to produce a binary image. An example of an ultrasound image before and after segmentation and after masking is shown in Figure 3–1.

3.3 Centerline extraction

In the presence of the pulsating blood flow, the vessel walls and nearby tissue may move and cause a Doppler signal outside the vessels. This may cause the real vessel to have an apparent diameter that exceeds the real diameter of the vessels. In general, vessels will therefore appear thicker in Doppler ultrasound images than in corresponding MRA data, for example. For use in image registration algorithms, this might be a challenge in cases where a matching between vessel boundaries is performed. By extracting centerlines from the segmented vessels for use in the image registration, this problem is largely overcome. Other advantages of this approach are the reduced number of voxels that participate in the registration and thus reduced computation times. A number of different methods have been presented in order to extract centerlines from tubular structures. A suitable method for this task should preserve the geometry and topology of the object and be reasonably fast to estimate. A sequential 3D thinning algorithm was presented by Palagyi et al. [87] and applied to images of the airways, blood vessels and

colons. Deschamps et al. [88] proposed a path tracking algorithm in 3D by finding the minimal path between two user-defined end points. The minimal path is considered the path for which the integral of a cost function between the two end points is minimal. This technique was applied to virtual endoscopy of the colon, CT data of the trachea, MRA of the brain and MR images of the aorta. Aylward et al. [89] presented a method of intensity ridge traversal and investigated the influence of initialization, noise and singularities on the algorithm. Wink et al. [90] also proposed a minimum cost path, but started by creating a multiscale vessel representation of the image based on Frangi's vesselness measure [91]. The vector field was then converted to a cost image and the minimum cost path search was performed.

In this thesis, vessel centerlines were extracted using a fast, robust and automatic method based on medial surfaces. The technique uses the average outward flux of the gradient vector field of the distance transform of the object to compute the medial surface [93]. The centered medial curves are then obtained by topology preserving thinning ordered by the distance function to the object's boundary. This ensures that the remaining points lie on the medial surface and as far away from the vessel boundary as possible. The medial curve was finally pruned based on length to remove small superfluous branches and obtain a single curve for each vessel branch. Details on the method can be found in [94]. An example of the segmentation and centerline extraction in an ultrasound image is shown in Figure 3–2.

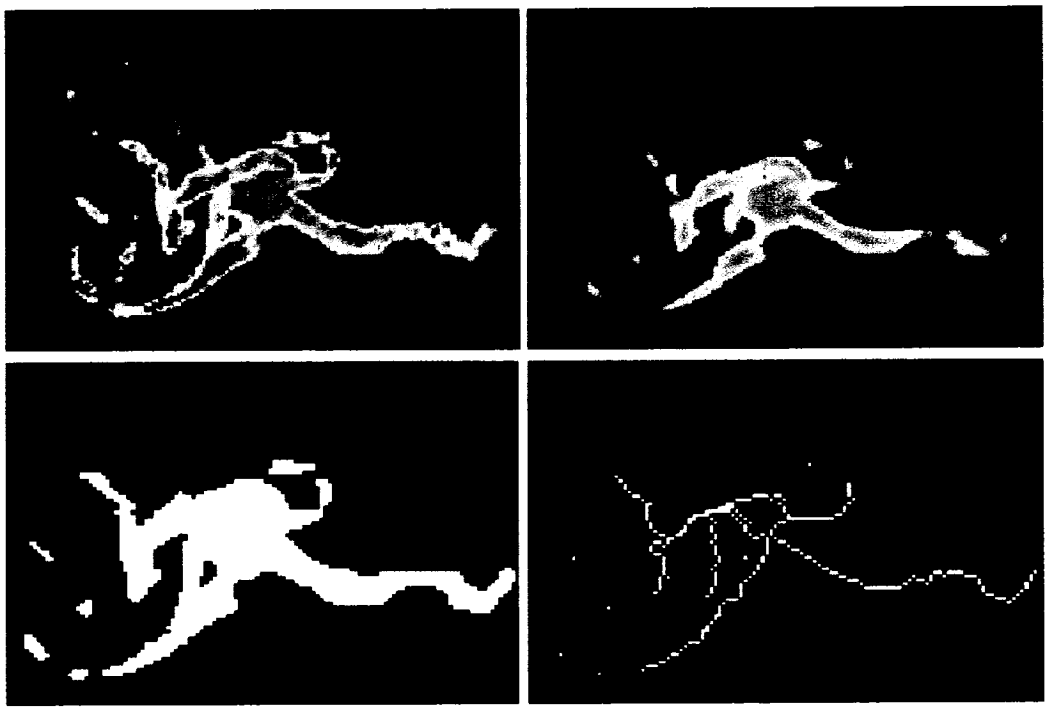

Figure 3–2: Pre-processing of an ultrasound image of an aneurysm acquired from the dura. Top left: Maximum intensity projection (MIP) of the original volume. Top right: MIP of the blurred volume. Bottom left: MIP of segmented volume. Bottom right: MIP of extracted centerlines.

3.4 Registration algorithm

After segmentation and centerline extraction, the MRA image and the Doppler ultrasound volumes are binary images representing the vascular tree. The vessels are in the form of a "skeleton" representing the midlines. The two datasets are only partially overlapping, and vessels are not necessarily continuous. A number of vessels might also be missing from one or both data sets. The task of registering the two datasets using a modified version of the original ICP algorithm proposed by Besl and McKay [95], can be summarized in the six following steps :

1. Sampling
2. Point matching
3. Weighting/Rejecting point pairs
4. Estimating the transformation
5. Applying transformation to the source points
6. Calculating the error

The details of these six steps are described in the following sections.

Sampling

There are multiple ways of sampling the original centerline data. The simplest method proposed in the original ICP algorithm is to use all available points. Since then, a number of other sampling strategies have been presented in order to improve the convergence rate, reduce sensitivity to noise and missing data or to adapt to particular types of images. Turk et al. [96] created triangle meshes from range images and used the ICP algorithm to bring corresponding portions of different meshes into alignment with one another. The creation of triangle meshes represents a uniform sub-sampling of the images. Sub-sampling of the images is an efficient way of reducing computation time, but depending on the sampling frequency, accuracy may be compromised. A different method of sub-sampling is to choose a number of points extracted at random. Masuda et al. [97] used this technique with a different subset of points at each iteration in order to provide different starting positions for the algorithm. Other possibilities include selecting points with high intensity gradients [98] or choosing points such that the distribution of normals among selected points is as large as possible [99] in order to obtain more points in regions with small features critical to determine the correct alignment. In line-to-line

registration, such features could be regions with high curvature or bifurcations. In this thesis we start with all available source points and then selects points based on the distance to the target. As an option it is possible to perform a uniform sub-sampling of the selected points in order to speed up the computation. Sub-sampling the source data will speed up the computation, but also influence the registration result. In the algorithm presented in this thesis, the registration error as a function of sample ratio can present several local minima. This parameter should therefore be chosen carefully for each registration.

Point matching

The next step addresses the problem of finding corresponding points in the source and target point sets. In the original ICP algorithm, the simple Euclidean distance was used to find the closest point in the target dataset. The closest-point algorithm tends to produce a large number of incorrect pairings when the images are relatively noisy or do not completely overlap. This sensitivity to noise and missing data is one of the main disadvantages of the original ICP algorithm. Because noise and missing data are problems frequently encountered in real images, a number of point matching techniques have been developed in order to increase the robustness of the registration algorithm. Possible approaches used in the past are to find the intersection of the ray originating at the source point in the direction of the source point's normal with the destination surface, or different projection methods such as projection of the source point onto the target followed by a local search based on distance or intensity [101]. For example, Rusinkiewitcz et al. [99] found that the projection-based algorithms converged significantly faster than the closest point method. In the experiments presented in this

thesis, we reached convergence in less than 20 iterations in all cases, and registration was completed in less than 30 seconds which was considered satisfactory. We have therefore chosen to keep the original point matching technique based on the Euclidean distance and minimize the number of incorrect pairings by implementing the least-trimmed squares estimator as explained in the following section.

Weighting and rejecting point pairs

The idea behind the assignment of weights or completely discarding certain point pairs is to limit as much as possible the influence of erroneous pairings on the transform computation. Efforts are made to reduce the number of such pairs through sampling and point matching strategies, but when dealing with noisy data where the overlap is not complete and data are missing as is the case here, efficient weighting and rejection techniques may considerably improve the final result. Without any weighting and/or rejection strategy, all pairs will be used and all points will be equally weighted. A simple modification to this method is to assign lower weights to pairs with greater point-to-point distance, and to possibly reject corresponding points more than a given distance apart by weighting these points with a weight of zero. Another method proposed in the past is weighting based on the compatibility of normals. The weight is then calculated as the scalar product of the normals. Point pairs with colinear normals will have weights equal to one, and point pairs with perpendicular normals will be rejected.

Other strategies include rejection of pairs whose point-to-point distance is larger than some multiple of the standard deviation of distances, or rejection of pairs that are not consistent with neighboring pairs. A potentially very useful strategy is to remove pairs

that include points on boundaries. These pairs may introduce a systematic bias in the estimated transform in cases where the overlap is not complete.

Yet another possibility is to use robust regression methods such as the Least Median of Squares (LMS) [102] or the Least Trimmed Squares (LTS) [103]. Both these methods were first presented by Rousseeuw [112]. While the least squares technique minimizes the sum of squared residuals, the LMS minimizes the median of squared residuals. The least-trimmed-squares (LTS), which is the estimator used in this thesis, is defined as:

$$E = \min_{\hat{\theta}} \sum_{i=1}^{h} r_i^2$$

where $r_1^2 \leq \cdots \leq r_n^2$ are the ordered squared residuals, n is the sample size, p is the number of dimensions, $\hat{\theta}$ is a vector containing the regression coefficients, and h is the breakdown value. This optimization procedure is equivalent to finding the subset of h points with smallest least squares objective function. The LTS regression estimate is then the least-squares fit to these h points. The LTS converges at a rate proportional to $n^{1/2}$ which is faster than the least median of squares. Its objective function is also smoother, making it less sensitive to local effects. This estimator is very similar to the least-squares method, the only difference being that the largest squared residuals are not used in the summation, thereby allowing the fit to ignore outliers. The value of h has to be set between $(n + p + 1)/2$ and n, but can be chosen according to the amount of contamination in the dataset. If the expected contamination is only a few percent, h can be set equal to 95% of n, for example. In situations where more severe contamination is expected, h should be set closer to the lower limit.

In spite of these advantages, the LTS estimator has been applied less often than the least median of squares because it was more difficult to compute due to the ordering of the residuals. Following point selection by LTS, it is possible to uniformly sub-sample the selected points in order to speed up the computation. This is particularly useful when doing non-linear registration.

Transformation

Most of the registration methods using a variant of the ICP algorithm estimate a rigid body transform (3 translations and 3 rotations). For linear registration, we have also included the possibility to perform isotropic scaling, which gives a total of 7 parameters. In general, when working with data-sets from the same patient scaling should not be necessary and 6 parameters will give a satisfactory result. In cases where the ultrasound volume registration, or even ultrasound probe calibration are inaccurate a scaling factor in the registration algorithm might improve the registration result. Scaling effects due to calibration errors are most likely to be present in the direction of the ultrasound beam. This approach could therefore possibly be improved further by estimating non-isotropic scaling parameters.

While a linear registration might be sufficient in cases of motion detection or to provide a good starting position for non-linear registration, it is not enough to describe the highly complex brain deformation taking place during neurosurgical interventions. The deformation is non-linear, and single points can move as far as 50 mm from their initial position. In this work, we start by estimating a linear registration with 6 or 7 parameters. In neuronavigation, this linear transformation is required due to the error in the patent registration performed prior to the opening of the skull in addition to

the actual linear component of the brain deformation occurring after the craniotomy. Following linear registration, non-linear registration is necessary in order to account for brain deformation. A number of different methods have been proposed for non-linear registration of point sets. The most popular methods used in image registration are different types of splines. These include Bézier splines, elastic B-splines, elastic body splines and a number of different radial basis functions. Bézier curves suffer from some important limitations such as lack of local control, high computational complexity and relatively poor fitting. In image registration, trilinear Bézier splines were applied by Otte [104] to register fMRI data to anatomical data-sets. A far more popular approach is the use of B-splines. They represent a lower computational complexity and give a better representation of the data by a closer but non-interpolating fit. The local control of the spline can be improved with hierarchical methods such as the technique presented by Forsey et al. [105] and applied by Xie et al. [106] to register MR images of the brain. Yet another solution in order to represent the displacement and deformation of an elastic body is the elastic body spline. This method has been applied in face modeling [107], for example. The elastic body spline assumes a homogeneous, isotropic elastic body subject to forces. In addition, it requires an estimate of the mechanical properties (Poissons ratio) of the body. For registration of images of the human brain, these assumptions remain problematic because human brain tissue is neither homogeneous nor isotropic, and the Poissons ratio of the brain *in vivo* remains largely unknown. Another group of splines widely used in image registration is the radial basis functions (RBFs). These functions include the Gaussian, the multiquadric, and the thin-plate spline. These splines are interpolating splines and they all minimize certain energy norms and are therefore

the smoothest splines. The Gaussian has been widely used in neural networks [109], but similar functions have also been used in elastic image registration [110]. Penney et al. [108] presented a registration algorithm that allows rigid bodies to be incorporated into a non-linear deformation based on radial basis functions. Zagorchev et al. [111] compared the multiquadric and thin-plate splines among others for non-rigid image registration. They found that both the multiquadric and the thin-palte spline were most suitable in cases where the number of points was relatively small (<1000) and the variation in spacing between the points was small. When considering compuational complexity, the multiquadric was found to be several times slower to estimate than the thin-plate spline. In this thesis, non-linear deformations are represented by the thin-plate spline (TPS) transformation [113]. TPS is an interpolation method that finds a "minimally bended" smooth (hyper)surface that passes through all given points. The summary given below closely follows the presentation given by Bookstein in [113] and [114]. For ease of notation, the summary given below desribes the two dimensional thin-plate splines. The extension to three dimensions is straight forward and the required modifications are pointed out at the end of this section. In two dimensions, the method can be summarized as follows:

Let U be the function

$$U(\vec{r}) = \frac{1}{\sigma} r^2 \log r$$

where σ is a scaling parameter that will determine the "stiffness" of the spline, and $P_i = (x_i, y_i)$ with $i = 1, ..., k$ are the k points irregularly spaced in the plane. It is then

possible to write $U_{ij} = U(P_i - P_j)$ and build the matrices:

$$K = \begin{pmatrix} 0 & U_{12} & \dots & U_{1k} \\ U_{21} & 0 & \dots & U_{2k} \\ \vdots & \vdots & \ddots & \vdots \\ U_{k1} & U_{k2} & \dots & 0 \end{pmatrix}, \quad Q = \begin{pmatrix} 1 & x_1 & y_1 \\ 1 & x_2 & y_2 \\ \vdots & \vdots & \vdots \\ 1 & x_k & y_k \end{pmatrix}$$

and

$$L = \begin{pmatrix} K & Q \\ Q' & O \end{pmatrix}$$

where O is a 3×3 matrix of zeros. Then write

$$W = \begin{pmatrix} w_1 \\ w_2 \\ \vdots \\ w_k \\ a_0 \\ a_x \\ a_y \end{pmatrix} = L^{-1} \begin{pmatrix} h_1 \\ h_2 \\ \vdots \\ h_k \\ 0 \\ 0 \\ 0 \end{pmatrix}$$

The thin-plate spline having values h_i at points $P_i = (x_i, y_i)$ with $i = 1, ..., k$ is given by

$$f(P) = \sum_{i=1}^{k} w_i U(P - P_i) + a_0 + a_x x + a_y y$$

The most important properties of this function are:

1. $f(P_i) = h_i$, which means that the interpolation is exact at the points P_i.

2. The function f has a minimum bending energy and thus minimizes the quantity

$$I_f = \int\int_{R^2} \left(\left(\frac{\partial^2 f}{\partial x^2} \right)^2 + 2 \left(\frac{\partial^2 f}{\partial x \partial y} \right)^2 + \left(\frac{\partial^2 f}{\partial y^2} \right)^2 \right)$$

3. The value of this bending energy is

$$\frac{1}{8\pi} W^t K W = \frac{1}{8\pi} W^t H = \frac{1}{8\pi} H_k^t L_k^{-1} H_k$$

where L_k^{-1}, the bending energy matrix is the $k \times k$ upper left submatrix of L^{-1}, and H_k is the initial k-vector of H.

In three dimensions, the function U becomes $U(\vec{r}) = |r|/\sigma$, the matrix Q now has four columns, and the integral I_f has six terms.

In the application to two-dimensional homologous landmarks, it is necessary to compute two surfaces: in the first surface f_x the matrix Q is loaded with the source points and the vector H is loaded with the x-coordinates of the target points. In the computation of the second surface f_y, the vector H is loaded with the y-coordinates. The resulting functions provides the interpolated x and y-coordinates of the deformation of one point-set onto the other with a minimum bending energy. The same is true in three dimensions.

TPS are particularly popular in representing shape transformations, for example in image morphing or shape detection. In this work, we use the thin-plate spline transformation with points selected as described above, to represent the non-linear component of the deformations.

The points used for non-linear registration are selected in the same way as the point used for linear registration. Each source point is paired to the closest point in the target, distances are sorted and points corresponding to the greatest distances are excluded from

the estimation of the non-linear fit. Because the thin-plate spline transform requires the inversion of a $n \times n$ matrix, the computation time increases rapidly with the number of points. In order to limit the number points in the non-linear registration it is possible to uniformly sub-sample the source dataset. In general, less than 500 points should be used in order to obtain a result in less than 30 seconds on a 1.67 GHz PC.

Registration error

In the original ICP algorithm, the mean squared error was used and the algorithm was proved to converge to a local minimum of the objective function in terms of this error metric. A "point-to-plane" metric can also be used by taking the sum of squared distances from each source point to the plane containing the target point and oriented perpendicular to the target normal [115]. The robust estimators LMS and LTS also converge to a local minimum of the objective function depending on the starting position [112]. The thin-plate spline transform needs to have a reasonably good starting point, in terms of correct point pairings in order to give a satisfactory result. In most cases involving registration of pre-operative MR and intra-operative ultrasound, the two modalities will be linearly registered at the beginning of the procedure. This initial registration can be corrected by performing a linear ICP registration with 6 or 7 parameters as described above. In cases where there is no initial linear registration, it is possible to manually perform a coarse linear registration by dragging the source dataset into place.

Algorithm

In this project, we have chosen to use the least trimmed squares and the simple Euclidean distance for point matching. The algorithm can be summarized in four steps:

1. Find the closest point in the target dataset for each source point.
2. Sort the distances, and select the source points corresponding to the n% smallest distances.
3. Estimate a 6 or 7 parameter linear transform or a thin-plate splines deformation based on the selected points.
4. Apply the transformation to the entire dataset.

For the linear registration, the steps described in the previous sections need to be iterated until a stopping criterion has been met. In previous literature, this criterion is usually a fixed number of iterations, an error metric below a pre-defined threshold or the difference between two successive error measurements below a pre-defined threshold. In this work, the iterations for the linear registration are stopped when the difference in mean distance between the source points and their closest target point between two successive iterations is smaller than 0.0001mm. Because the thin-plate spline transform gives an exact fit, only one iteration is needed for the non-linear registration.

In summary, the registration method developed for this thesis uses automatically extracted vessel centerlines as landmarks to drive the patient-image registration with a linear or non-linear transformation between intra-operative Doppler ultrasound images and preoperative MRA data. The technique uses ICP with LTS to improve robustness. The following chapters will describe the work completed to test and validate the method.

Chapter 4

The brain phantom

Foreword

The first step in the process of validating the registration technique described in the previous chapter was thorough testing in a context of simple geometry and carefully controlled deformations. The primary goal of the manuscript presented in this chapter was to design, build and characterize a deformable brain phantom for use in validation experiments of the registration algorithm. In order to determine the suitability of the phantom as a gold standard for validation experiments, the repeatability of the deformations was carefully measured using MR images and surface measurements using a computer tracked pointer. We also wished to verify the compatibility of the phantom with MR and ultrasound imaging, which are the two main imaging modalities used in this thesis. The results show that the deformations of the phantom were reproducible to within 1 mm, and that the phantom was therefore well suited for use in validation

experiments of the registration technique. We also showed that it was compatible with MR imaging as well as B-mode and Doppler ultrasound imaging. This work has been published in the journal *Medical Physics*, 33(9), p. 3234-3240, 2006.

A Realistic Phantom for Brain-shift Simulations

I. Reinertsen[1] and D. L. Collins[1]

[1] Montreal Neurological Institute (MNI), McGill University, Montréal, Canada

Medical Physics, 33(9), p. 3234-3240, 2006.

4.1 Abstract

Validation of techniques that characterize and correct for brain-shift for image guided surgery requires a realistic anthropomorphic phantom for use as a gold standard. The purpose of this study was to determine the characteristics of a deformable brain phantom made of polyvinyl alcohol cryogel (PVAc). The phantom was made of three layers of PVAc with inserted plastic tubes to simulate blood vessels. A catheter with an inflatable balloon was placed under the phantom in order to deform it in a non-linear manner. The reproducibility of the elastic deformation was evaluated using MR imaging and surface measurements. Our experiments show that the phantom is well suited for MR and ultrasound imaging (B-mode and Doppler) with sub-millimeter reproducibility for the deformations.

4.2 Introduction and Motivation

A significant source of error in image guided neurosurgery (IGNS) systems is brain tissue movement and deformation, so called brain shift, during the procedure. Tissue movement can be caused by gravity, drainage of cerebro-spinal fluid, retraction and resection of tissue, swelling of brain structures, and administration of drugs. The amount of movement and its influence on the accuracy of the neuro-navigation system depend on a number of factors including surgical target size and location, craniotomy size and patient position during surgery.

A number of methods have been developed to quantify and account for deformations. These include deformable models, often updated with intra-operative measurements of the displacements of the exposed cortical surface [47, 48, 49], and intra-operative imaging (MR, CT, Ultrasound). Intra-operative images can be used directly for navigation [14], or used in registration algorithms to update pre-operative data [50, 52]. In order to be routinely used in neuro-navigation systems these methods have to be thoroughly tested and validated. Validation should ideally consist of experiments on simulated data (numerical simulations and phantom data) where the truth is known, and on real patient data that represent the full anatomical complexity and the full range of possible deformations. In the first part of the validation process, simulations of brain deformations using a realistic phantom is therefore potentially very important.

Because several imaging modalities (MR, CT, Ultrasound,...) are commonly used in surgical planning and navigation, a suitable phantom should resemble human brain tissue in all the desired imaging modalities. A suitable phantom should also deform in a repeatable elastic non-linear manner when internal or external forces are applied. Finally

it should be roughly of the same size and shape as the human brain, in order to simulate deformations as realistically as possible.

In addition to known and reproducible deformations, a phantom represents a number of other advantages such as a simpler well-defined geometry and long term stability. A well designed phantom can also be an important part of a testing and training setup for image guided neuro-navigation that can be useful for surgeons as well as technical personnel and engineers.

In this study we designed a realistic brain phantom for testing and validation of brain-shift correction techniques and in particular image registration algorithms. The phantom is deformed by inflating a balloon catheter with a known volume of water. Our goal was to characterize the reproducibility of the deformation and to demonstrate that the phantom structures were visible in ultrasound and MRI. The deformations were characterized using MRI as well as surface measurements. Through the characterization of the phantom and its deformations we investigated its suitability as a gold standard for studies of brain-shift.

4.3 Phantom preparation

The phantom was made of three layers of polyvinyl alcohol cryogel (PVAc). Polyvinyl alcohol (PVA) is a non-toxic industrial compound, widely used in glue, paint and food and textile packaging. PVA is a synthetic resin produced by polymerization of vinyl acetate followed by hydrolysis of the polyvinyl acetate polymer. The degree of polymerization determines the molecular weight and viscosity, while the degree of hydrolysis signifies the extent of conversion from polyvinyl acetate to polyvinyl alcohol. An aqueous solution of PVA that is first heated to dissolve, then frozen and thawed

one or multiple times forms a highly elastic gel by the formation of micro-crystalline structures [53]. The size of these structures and thus the rigidity of the resulting gel depends on the concentration of PVA in the aqueous solution, the freeze time, the thaw time and the number of freeze-thaw cycles. The resulting gel is referred to as polyvinyl alcohol cryogel.

In recent years PVAc has been used as a tissue-mimicking material in a number of magnetic resonance (MR) and ultrasound (US) imaging applications [54, 18]. The popularity is due to mechanical and imaging characteristics close to those of human tissue in addition to ease of use and long-term stability.

4.3.1 Preparation of liquid PVA and PVA cryogel (PVAc)

To prepare the liquid PVA, the technique proposed by Surry et al. [54] was applied. A 10% by weight solution of PVA powder (Celvol 165, Celanese chemicals, Dallas, TX) and de-ionized water was prepared. The mixture was stirred using a magnetic stir plate to eliminate any aggregates of powder. In order to dissolve the PVA powder, the solution was heated to 121°C for 30 minutes in a steam autoclave. The resulting clear gel was stirred again for 30 minutes as it cooled down to room temperature. In order to obtain a solid phantom, the liquid PVA solution was poured into a mold. The solution was allowed to rest for 2-3 hours for air bubbles to rise to the surface and be removed. The mold with the liquid solution was then placed in a freezer at room temperature. A digital data logger was used to monitor the temperature in the freezer during the freeze thaw cycle. The freezer was turned on, and reached -20°C within one hour. The freezer was kept at this temperature for another 11 hours, for a total freeze time of 12 hours. The freezer was then turned off and allowed to come back to room temperature over a

period of 24 hours. The temperature of the freezer as a function of time during a typical freeze/thaw cycle is shown in Figure 4–1. The PVAc was then removed from the freezer for use.

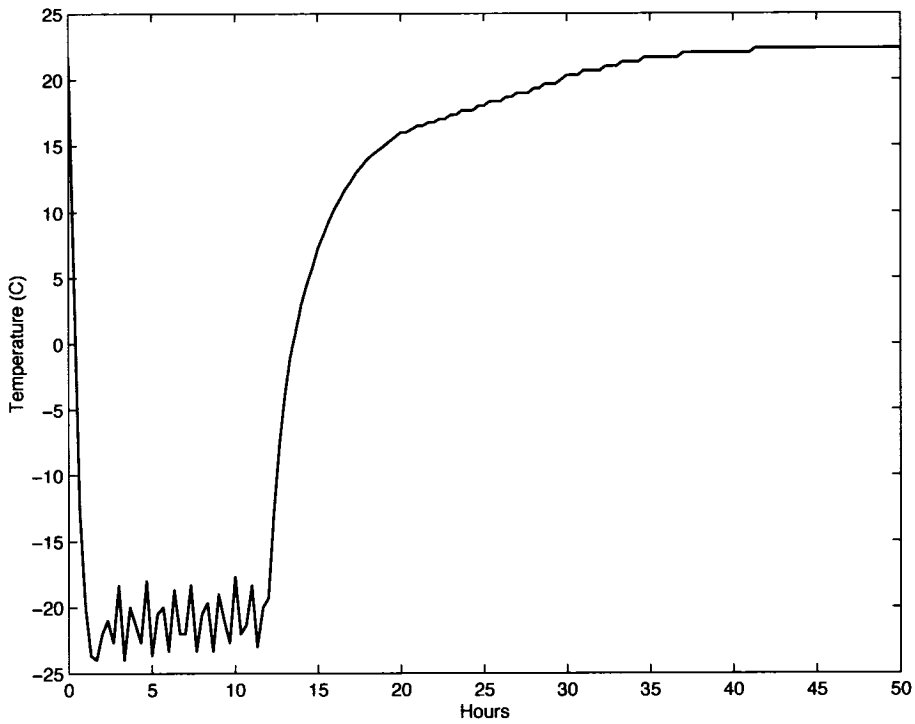

Figure 4–1: Typical freezer cycle.

4.3.2 The PVAc phantom

The phantom consisted of three different parts, all made of PVAc. The first part was made to simulate the cerebral falx and was a circular disc 20 cm in diameter and 1 cm thick. The disc was frozen and thawed separately in a plastic container. The second and most important part of the phantom was made using a brain mold (SKS Sibley Co., El Segundo, CA). The mold was filled with 500 ml liquid PVA, and plastic tubing with inside diameters of 1.57, 2.36, and 3.18 mm and two branching points was inserted into

the PVA. Two loops of tubing were left outside the mold and later attached to the surface of the phantom. A photo of the mold with inserted plastic tubes and liquid PVA is shown in Figure 4–2. Once the plastic tubes were inserted and any bubbles removed from the surface, the PVAc disc was fitted to the brain mold and placed on top of the liquid PVA. The mold with the liquid PVA, the tubes and the PVAc disc on top was then frozen and thawed. When the phantom had reached room temperature it was removed from the mold and the two loops of tubing were attached to the surface using surgical thread.

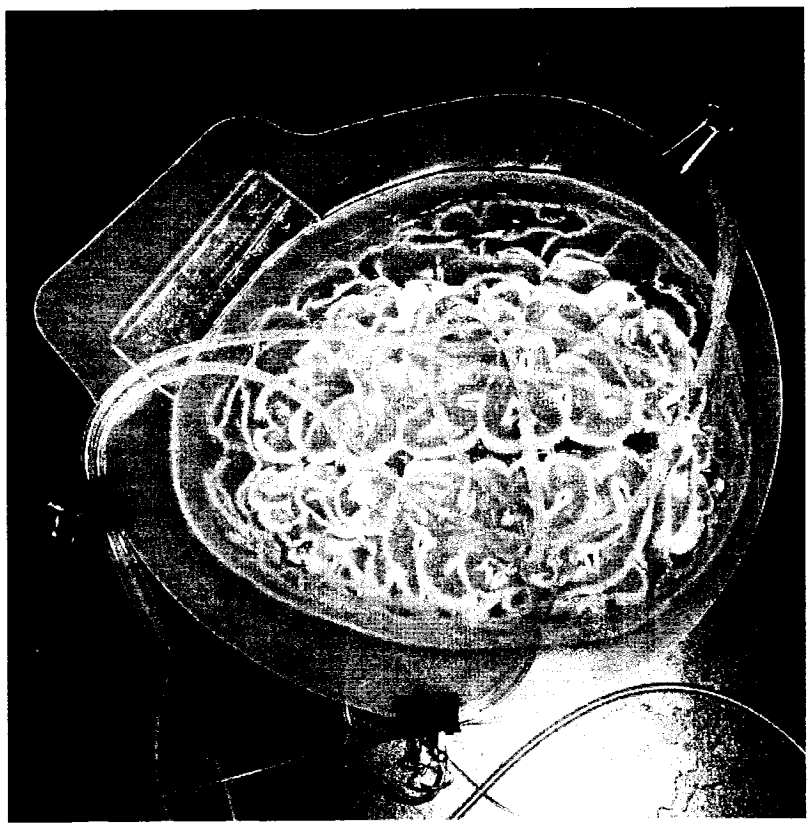

Figure 4–2: The brain mold filled with liquid PVA and plastic tubes

The PVAc disc and brain were then placed in an acrylic plastic container specially designed for the phantom. The container was cylindrical with a diameter of 20 cm. A

5 ml Bardex Foley catheter (C. R. Bard, Inc., Covington, GA) was placed under the PVAc disc and brain in the container. The container was finally filled with liquid PVA all around the phantom and about 2.5 cm deep to keep the catheter in place and prevent the PVAc disc and brain from moving inside the container. The entire container with the PVA disc and brain was then frozen and thawed. Following this last freeze-thaw cycle the disc had been frozen and thawed three times, the "brain" with the tubing twice and the PVA around the "brain" once. These three PVAc regions have different mechanical and imaging characteristics due to the different number of freeze-thaw cycles. A photo of the phantom is shown in Figure 4–3.

The catheter balloon placed under the PVAc disc and brain can be inflated by using a syringe to inject water into the catheter tube. The inflation of the balloon will cause the phantom to deform in an elastic non-linear manner. By measuring the volume of water injected into the catheter, the deformation of the phantom can be controlled. In the experiments described in the following section, we investigate the suitability of the phantom for MR and ultrasound imaging. We also characterize the reproducibility of the deformation through a series of surface measurements performed with a tracked pointer, and measurements of internal landmarks performed using the MR images of the phantom.

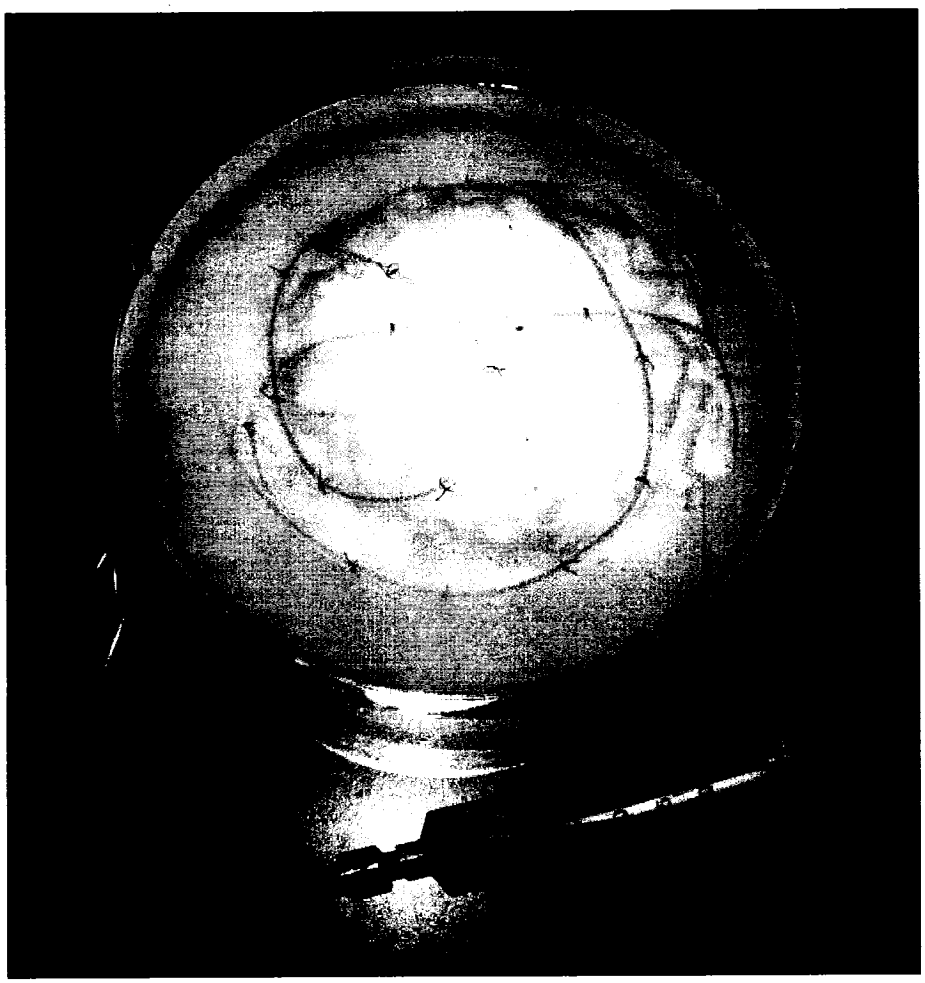

Figure 4–3: The brain phantom in the plastic container. The syringe was used to inject water into the catheter balloon to deform the phantom

4.4 Experiments

4.4.1 Surface measurements with handheld pointer

To characterize the repeatability of the surface deformation, ten easily identifiable landmarks on the surface of the phantom were measured with the Polaris optical tracking system (Northern Digital Inc., Waterloo, ON) and a handheld passive probe (Traxtal Inc., Toronto, ON). Before performing the measurements, the tracking error of the system was evaluated to be 0.3 mm by clamping the tracked pointer in a fixed position and capturing the position of the pointer 12 times. All ten surface points were recorded after each deformation, and the series of measurements was repeated four times for each catheter balloon volume. The mean and maximum distances between the measurements at each point and for each deformation are shown in Table 4–1, and plots of the recorded points are shown in Figure 4–4.

Point	Deformation A		Deformation B		Deformation C	
	Mean	Max	Mean	Max	Mean	Max
1	0.94	1.60	3.15	5.46	1.47	2.28
2	1.25	1.67	1.31	2.16	1.03	1.54
3	1.31	2.08	0.76	1.02	1.36	2.17
4	1.17	1.72	0.77	1.28	1.41	2.15
5	1.11	1.83	0.92	1.49	1.17	1.53
6	1.31	1.90	1.30	2.08	0.86	0.96
7	2.12	3.62	0.85	1.54	1.70	2.68
8	1.13	1.75	0.97	1.76	1.10	1.97
9	2.50	4.81	1.27	2.04	1.25	2.04
10	1.19	1.52	1.48	2.24	1.52	2.06

Table 4–1: Surface measurements with handheld pointer: Mean and maximum distances between the four measurements at each point and for each deformation. Deformation A corresponds to a catheter balloon volume of 0 ml, Deformation B corresponds to 5 ml and Deformation C corresponds to 10 ml. All measurements in mm.

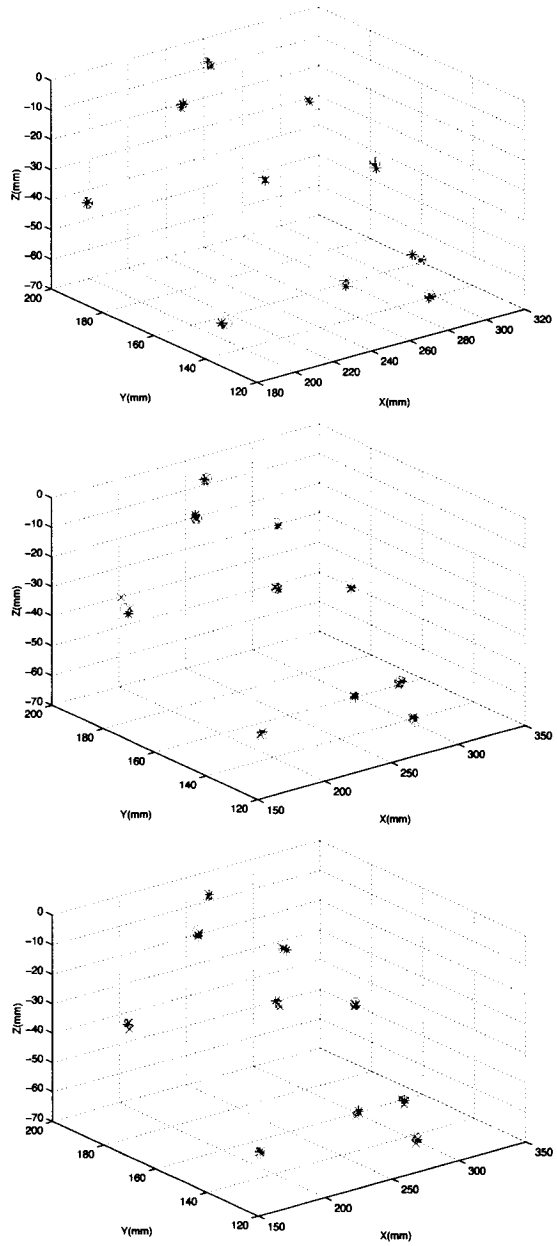

Figure 4–4: Surface measurements with handheld pointer: The ten recorded points for three different catheter balloon volumes: Empty balloon (top), half-full balloon (middle) and full balloon (bottom). The symbols o, +, x(green) and x(red) represent the four series of measurements for each balloon volume

4.4.2 Surface measurements with clamped pointer

In order to maximize the precision of the measurements and minimize the error associated with human error in accurately identifying points on a soft surface, we clamped the pointer before every recording and repeated a series of surface measurements. The same point was measured 4 times for each catheter balloon volume with a deformation (inflation or deflation of the balloon) between each measurement, for a total of 12 measurements per surface location. The mean and maximum distances between the measurements are shown in Table 4–2 and the standard deviation for each of the three coordinates x, y and z are shown in Table 4–3. Plots of the recorded points are shown in Figure 4–5, and the surface locations are shown in Figure 4–6.

Point	Deformation A		Deformation B		Deformation C	
	Mean	Max	Mean	Max	Mean	Max
1	0.61	0.90	0.54	0.69	0.68	1.02
2	0.44	0.61	0.40	0.75	0.21	0.27
3	0.21	0.31	0.29	0.44	0.15	0.20

Table 4–2: Surface measurements with clamped pointer: Mean and maximum distances between the four measurements at each point and for each deformation. All measurements in mm.

Point	Deformation A			Deformation B			Deformation C		
	std(x)	std(y)	std(z)	std(x)	std(y)	std(z)	std(x)	std(y)	std(z)
1	0.38	0.19	0.08	0.25	0.23	0.18	0.35	0.19	0.31
2	0.21	0.04	0.24	0.21	0.11	0.21	0.08	0.08	0.11
3	0.06	0.07	0.12	0.10	0.15	0.12	0.06	0.08	0.05

Table 4–3: Surface measurements with clamped pointer: Standard deviation (mm) of x, y and z coordinates for the different deformations. Each point was measured 4 times

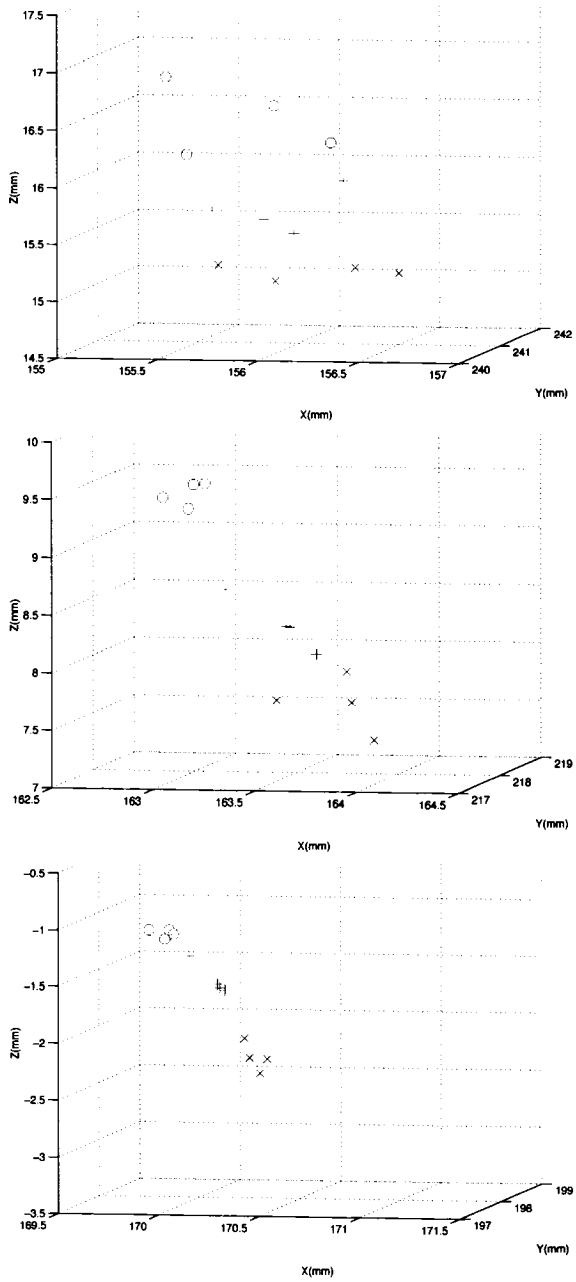

Figure 4–5: Surface measurements with clamped pointer: The three measures points: point 1 (top), point 2 (middle) and point 3 (bottom). Deformation A = x, Deformation B = + and Deformation C = o.

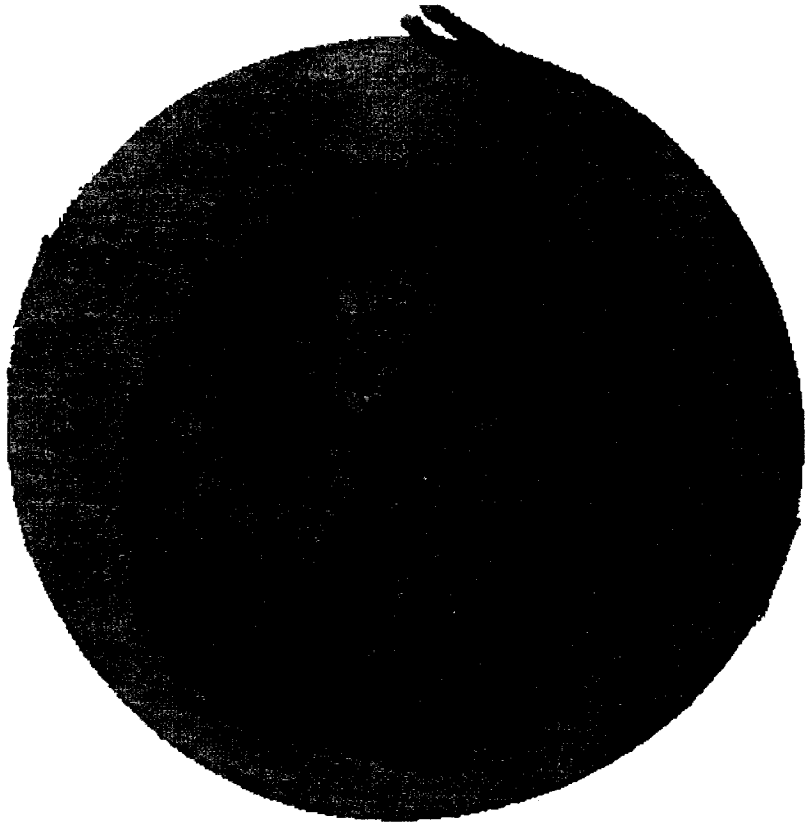

Figure 4–6: Surface rendering of the phantom with the tubes shown in red. The ten locations were surface measurements were performed with handheld pointer are shown in blue, and the three locations where surface measurements were performed with clamped pointer are shown in green.

4.4.3 MR imaging and measurements

The phantom was scanned using a Siemens SonataVision 1.5T scanner using a standard T1 weighted anatomical scanning sequence (TR=22 ms, TE=9.2 ms, flip angle = 30°) with full brain coverage and 1 mm isotropic resolution. The phantom was scanned six times, and the catheter was either inflated or deflated between each scan. The inflation or deflation of the balloon deformed the phantom in a non-linear fashion as shown in Figure

4–7. During MR imaging the phantom remained in the plastic container and the plastic tubes were filled with water.

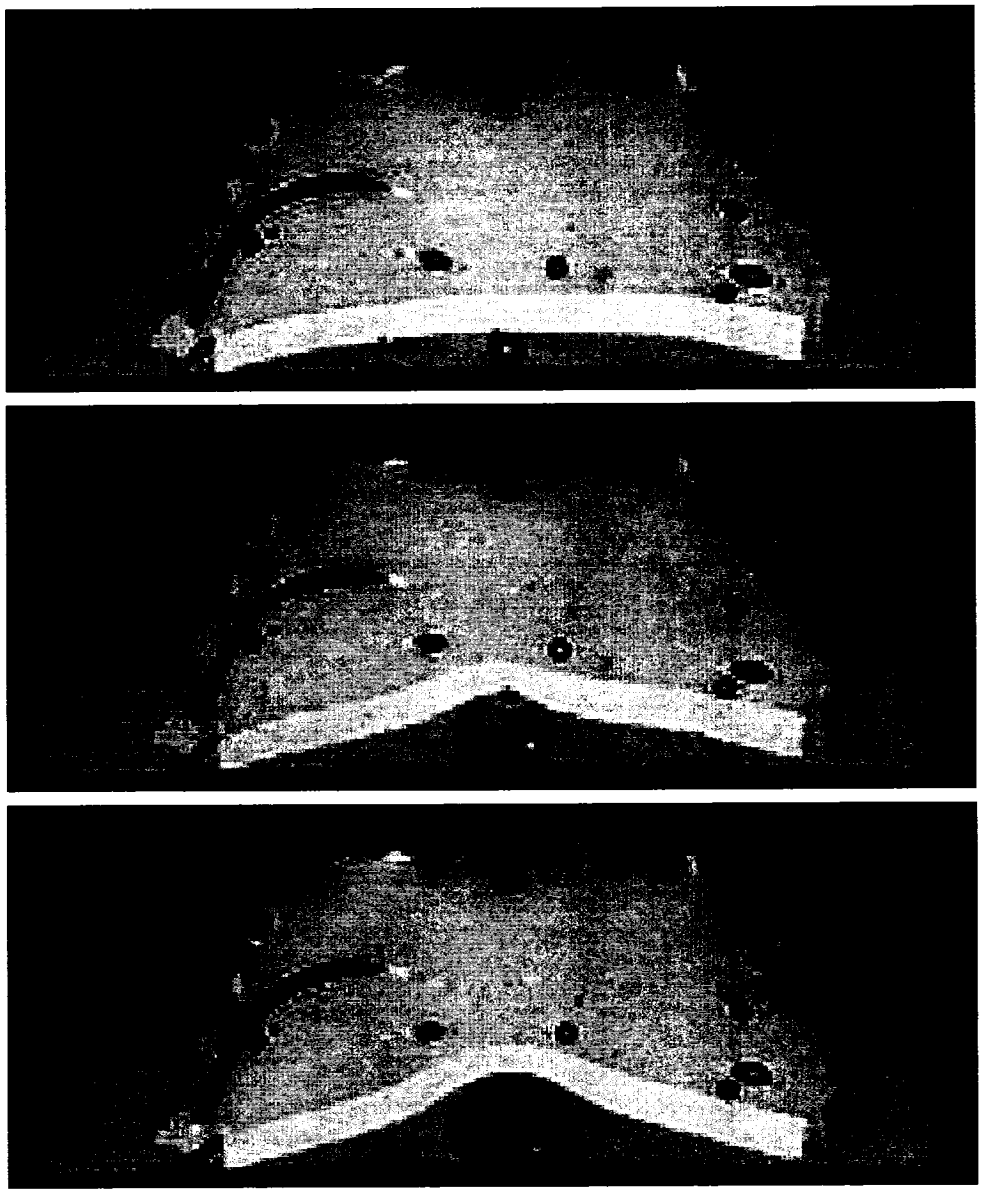

Figure 4–7: MR images of the phantom with empty catheter balloon (top), half-full catheter balloon (middle) and full catheter balloon (bottom).

In order to characterize the reproducibility of the deformation, a series of 10 landmarks distributed throughout the volume was manually identified in all six data-sets. These points were mainly air bubbles with a diameter of 2 to 3 mm trapped in the PVA, and appeared as dark spots in the MR images. The landmarks corresponding to equal catheter balloon volumes were compared. The distances between measured points are shown in Table 4–4.

	Deformation A	Deformation B	Deformation C
Mean	0.32	0.20	0.32
Max	0.98	1.09	0.97

Table 4–4: Internal landmarks: Distance in mm between points measured in corresponding scans.

4.4.4 US imaging

Ultrasound images were acquired using an HDI 5000, ATL (Bothwell, WA) ultrasound machine with an ATL P7-4 multi-frequency probe. Tracking was achieved with the use of the Polaris optical tracking system (Northern Digital Inc., Waterloo, ON), a passive reference and a passive tracker device (Traxtal Inc., Toronto, ON) attached to the ultrasound probe. A physiological pump (Manostat Corp., New York City, NY) was used to pump water through the plastic tubes while the phantom was scanned using regular B-mode and Doppler imaging. The plastic container with the phantom was filled with water, and the phantom was allowed to rest for a few minutes for air bubbles in the water to disappear. This procedure is analog to the one used in surgery when the craniotomy is filled with sterile water prior to ultrasound imaging. Air-filled glass micro-spheres (McMaster Carr, Atlanta, GA) were mixed in the water in order to enhance the Doppler signal and red food color was added to the water that was pumped through the tubes to

make it visible. A B-mode image and a Doppler image on top of their corresponding MR slices are shown in Figure 4–8.

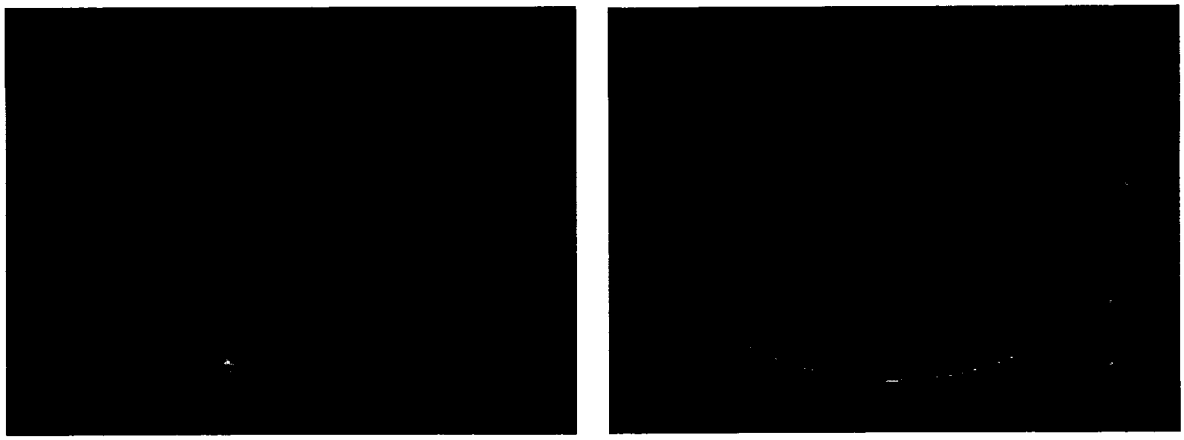

Figure 4–8: B-mode ultrasound in green overlaid on corresponding MR in grey (left) and color Doppler ultrasound image overlaid on corresponding MR in grey (right).

4.5 Discussion

Quantitative mechanical and imaging properties of PVAc have been investigated and reported in [54]. These experiments have not been repeated, but some qualitative observation have been made. First, the MR images of the phantom shown in Figure 5–5 show a relatively high contrast between the three different layers of PVA. The plastic tubes are easily identified, and we were able to see the water inside the tubes that have an inside diameter of only 1.57 mm. An MR contrast agent could have been used in order to get a higher signal from inside the tubes and differentiate it from the PVA. This would have been especially helpful to identify the tubes on the phantom surface.

The error in the measurements of internal landmarks in the MR volumes is the sum of the linear registration error between scans, potential geometric distortions in the data, manual landmarking error and the error in the reproducibility of the deformation that we

want to characterize. The ten point measurements show that the sum of all these elements give an average distance of 0.3 mm and a maximum distance between points close to 1 mm, which is equal to the resolution of the MR data.

The error in the surface measurements is the sum of the tracking error in the Polaris system, the manual landmarking error on a soft surface and the error in the reproducibility of the deformation. These errors in addition to the error in the reproducibility of the deformation gave an average error of 1.3 mm with a maximum distance of 5.46 mm for measurements performed with a handheld pointer. The large maximum distance in this experiment is due to the difficulty of repeatedly pointing to a specific location on a soft surface. The error was reduced to an average error of 0.6 mm and a maximum distance between measurements of 1.02 mm for measurements performed with a clamped pointer as shown in Table 4–2, which is consistent with the results from the identification of internal landmarks in the MR data. The standard deviation of the x, y and z coordinates was lower than 0.4 mm for all measurements as shown in Table 4–3.

No quantitative measurements were made from the ultrasound data, but as the images shown in Figure 4–8 suggest, the phantom is very well suited for ultrasound imaging. With B-mode imaging, the phantom surface, the different layers of PVA as well as the tubes inside the phantom were clearly visible. Doppler imaging of the phantom showed that the Doppler signal was easily detectable through the plastic tubes and the PVA. Our experiments showed that the Doppler signal was greatly enhanced when we added glass micro-bubbles to the water that was pumped through the tubes during scanning. This is due to the size of the reflectors in the fluid. Water molecules (10^{-10} m)are much smaller than the wavelength of the ultrasound beam (10^{-4}), and will not

cause longitudinal reflection of the beam. The particles added to the water are of the same order of magnitude as the red blood cells (10^{-6}), and will therefore cause a signal of similar amplitude to the signal observed from human blood vessels.

In order to make the phantom even more realistic, other brain structures such as the lateral ventricles can easily be simulated by creating liquid filled cavities in the PVA. It is also possible to simulate a grey/white-matter interface by changing the PVA concentration and/or the number of freeze-thaw cycles. Other possible improvements would be to place a small number of traditional fiducial markers or other markers on the phantom surface that would facilitate the landmark based rigid body registration of the phantom and the MR images for navigation purposes. An example of a similar phantom with fiducial markers can be seen in Fig. 4–9. For surface based measurements in order to characterize the deformation of the phantom, the use of such markers would not be practical due to the number of markers required and the size of the markers. It also important to notice that the markers have to be sewed onto the surface of the phantom and to not stick to the soft and humid surface. In this study, well defined patterns on the phantom surface were used for measurements. The points were not visible on the MR images, but as the points were not used for registration purposes, only to characterize the deformations, this was not critical. For applications using information about the plastic tubes, it would also be helpful to inject a contrast agent in the tubes before MR scanning. This would greatly enhance the signal, and make for example segmentation of the tubes easier. In fact, in the last phantom constructed in our lab gadolinium was pumped into the tubes before MR scanning. As can be seen in Fig. 4–9, this greatly enhances the signal from inside the tubes. This makes the use of any automatic segmentation

technique easier. In this case the tubes can be reasonably well segmented by simple thresholding based on intensity. However, as the identification and segmentation of the tubes were not involved in any of the measurements reported in this study, this extra feature would not have changed the results reported here.

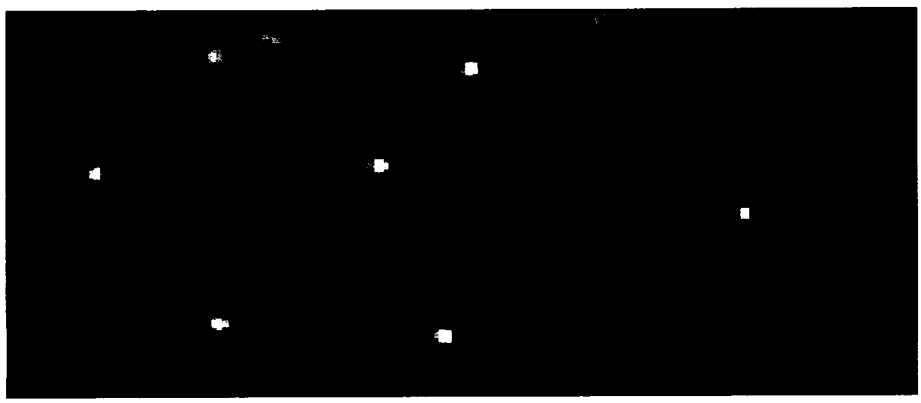

Figure 4–9: An example of a MR image of a similar phantom where the plastic tubes were filled with gadolinium before scanning. The signal from inside the tubes is greatly enhanced compared the signal from water-filled tubes. Source: Pierre Hellier

The phantom presented in this study had a lifetime of 4 months of extensive use. The weakest part proved to be the catheter balloon placed under the phantom in the container. In order to keep the PVA in good condition and maximize its useable lifetime, it is important to keep it humid at all times and change the water regularely. With careful handling and storage at 4°C in a regular fridge the phantom itself could last for at least a year.

4.6 Conclusions

In this study, we have designed, built and characterized the deformation reproducibility of a realistic phantom for simulations of non-linear brain deformations. Measurements of internal and surface landmarks show that the deformation of the phantom can be

reproduced with a maximum error of 1 mm. The phantom is therefore well suited to serve as a gold standard to evaluate detection and correction techniques for brain deformation. MR and ultrasound imaging show that the phantom is well suited for multi-modality imaging and that the main features of the phantom can be easily detected in both modalities. This is particularly important for its usefulness in testing different image registration algorithms. Finally, the phantom has shown to be a useful tool in testing and evaluating neuro-navigation software and in ultrasound guided surgery training.

Chapter 5

Validation of Vessel-based Registration for Correction of Brain-shift

Foreword

Having demonstrated in the previous chapter that the brain phantom was well suited for serving as a gold standard in validation experiments, we applied the registration algorithm to the phantom data in order to test the performance of the method in a situation with simple geometry and closely controlled deformations. The performance of the registration technique was evaluated by tracking a series of landmarks identified in the MR images of the phantom. This study also enabled us to quantitatively compare MR-MR registration and US-MR registration.

Because the phantom study only allows us to estimate the accuracy of the registration at a limited number of points, we also performed a series of numerical simulations were the transformation is known everywhere in the volume.

The numerical simulations showed that we were able to recover 75% of the deformations in the region covered by both imaging modalities, and in the phantom study we were able to correct the deformations to within 1.6 mm for the US-MR registration and to within 1.07 mm for the MR-MR registration.

The introduction and methods sections of this paper have already been presented in chapters 2 and 3 of this thesis. The description of the phantom data has also been seen in the previous manuscript. The reader may therefore choose to skip these sections without loss of information. The work presented in this chapter has been accepted for publication in the journal *Medical Image Analysis*.

Validation of Vessel-based Registration for Correction of Brain-shift

I. Reinertsen[1] , M. Descoteaux[2 3] , K. Siddiqi[2] and D. L. Collins[1]

[1] Montreal Neurological Institute (MNI), McGill University, Montréal, Canada

[2] Center for Intelligent Machines (CIM), McGill University, Montréal, Canada

Medical Image Analysis, In press, **October 2006.**

Reprinted with permission from Elsevier

5.1 Abstract

The displacement and deformation of brain tissue is a major source of error in image-guided neurosurgery systems. We have designed and implemented a method to detect and correct brain-shift using pre-operative MR images and intraoperative Doppler ultrasound data and present its validation with both real and simulated data. The algorithm uses segmented vessels from both modalities, and estimates the deformation using a modified version of the iterative closest point (ICP) alogrithm. We use the least trimmed squares (LTS) to reduce the number of outliers in the point matching procedure. These points are used to drive a thin-plate spline transform to achieve non-linear registration. Validation was completed in two parts. First, the technique was tested and validated using realistic simulations where the results were compared to the known deformation. The registration technique recovered 75% of the deformation in the region

[3] Present address: Odyssee Team, INRIA Sophia-Antipolis, France

of interest accounting for deformations as large as 20 mm. Second, we performed a PVA-cryogel phantom study where both MR and ultrasound images of the phantom were obtained for three different deformations. The registration results based on MR data were used as a gold standard to evaluate the performance of the ultrasound based registration. On average, deformations of 7.5 mm magnitude were corrected to within 1.6 mm for the ultrasound based registration and 1.07 mm for the MR based registration.

5.2 Introduction and Motivation

5.2.1 Neuro-navigation and brain-shift

Modern image guided neurosurgery (IGNS) systems enable the surgeon to navigate within the patient's brain using pre-operative anatomical images (MRI, CT) as a guide. The pre-operative images are related to the patient using a rigid body transformation calculated from a number of anatomical landmarks that can be easily identified on both the patient's head and the pre-operative images. By using a computer-tracked probe during the procedure, the surgeon can localize any point in the patient's brain on the pre-operative images. A significant source of error in these systems is brain tissue movement and deformation, so called brain-shift, during the procedure. Tissue movement can be caused by gravity, drainage of cerebro-spinal fluid, retraction and resection of tissue, swelling of brain structures, and administration of drugs. The amount of movement and its influence on the accuracy of the neuro-navigation system depend on a number of factors including surgical target size and location, craniotomy size and patient position during surgery.

The magnitude and direction of brain deformation during surgery have been the subject of several studies. The first quantitative measurements of brain deformation during

surgery relied on recordings of points on the cortical surface relative to fixed points on the cranial surface [55, 56]. These studies showed a cortical surface shift of 10 mm on average, and movement was found to be greatest along the direction of gravity.

To better describe the dynamic process of brain deformation, several groups have used intraoperative MRI (iMRI) to study brain shift [57, 58]. The results show that surface shift ranges from almost no detectable shift for smaller lesions to up to 50 mm for larger lesions. Surface shift well beyond the craniotomy has also been documented. As in the previously discussed studies it was found that surface shift was mainly due to loss of cerebro-spinal fluid and resulted in a shift in the direction of gravity. They also showed that surface shift occurs throughout the procedure while deformation of deeper structures occurs mainly during resection. Volume changes depend on the nature of the surgical procedure, and are in general greater for resection cases than for biopsies and functional interventions. The principal direction of displacement was not always aligned with the direction of gravity.

Intraoperative ultrasound has also been used to estimate brain-shift. Letteboer et al. [59] used ultrasound to measure the linear component of the shift at the tumor boundary. This study also confirms the assumption that the brain deforms mainly in the direction of gravity is not always valid.

In summary, the cortical surface shift is mainly caused by loss of CSF and subsequent "sinking" of the brain in the direction of gravity. Surface shift can occur well beyond the borders of the dural opening and can occur throughout the procedure. However, the surface has been shown to settle in cases where the resection cavity is smaller than the cortical opening. If the cavity is larger than the cortical opening, the borders sink

in to form a crater. Deformation of subsurface structures on the other hand is mainly due to resection, relief of weight and intraparenchymal pressures. Larger deformations are generally observed in the hemisphere ipsi-lateral to the lesion, but significant deformations can also occur in the contra-lateral hemisphere.

In the following sections, we present a detailed overview of previous work applied to the detection and correction of brain-shift. We present our vessel-based registration technique in section 6.4 followed by a series of validation experiments in section 6.6.

5.2.2 Model based techniques

With all this prior knowledge about how the brain shifts and deforms during surgery, a number of groups have developed model-based techniques to try to correct for the displacements. Among the first groups to attempt this approach was Miga et al. [47]. The technique was applied to four neurosurgical cases, and it was found that the model could account for 79% of the gravity induced deformations on average. Other groups have extended this work to include more complex deformations and deformation of deeper structures [56, 48]. In these studies, it was assumed that brain tissues are isotropic, homogeneous and with identical density and stiffness. It was also assumed that there is no deformation in the hemisphere contralateral to the craniotomy, and that all deformations can be estimated based on data from the exposed surface.

In general, the displacement and deformation of the brain during surgery is far more complex and far reaching than these models assume, and more work is needed to estimate the mechanical properties of the brain [49] in order for this type of approach to be useful in more than a very limited number of neurosurgical procedures.

The more direct solution to the problem is to acquire new images when significant amount of deformation is suspected. The most popular intraoperative imaging modalities for neurosurgery are intraoperative CT, intraoperative MRI, and intraoperative ultrasound (US) imaging.

5.2.3 Intraoperative CT imaging

A few groups have used intraoperative CT to actualize the navigation data and verify the anatomical situation during surgery [62, 61]. The CT images can be used to localize intracranial lesions, but suffer from lower soft tissue contrast than MRI, and are therefore less useful for brain surgery. CT imaging is more commonly used in spine surgery, where the vertebrae and surrounding structures are of primary interest. Other disadvantages of intraoperative CT imaging are the radiation dose to the patient which limits the number and duration of the scans, and the physical space occupied by the scanner in the operating room.

5.2.4 Intraoperative MR imaging

Intraoperative MRI (iMRI) scanners can provide the surgeon with updated anatomical images several times during a procedure, and can therefore be a valuable tool for characterization and correction of brain shift. One of the first reports on the use of iMRI for neurosurgical guidance was presented by Black et al. [64]. They illustrated the advantages of intraoperative MRI imaging in a series of 60 craniotomies for tumor resection. Images were acquired before and after opening of the dura and after closure of the craniotomy. Nimsky et al. [65] went one step further and used intraoperative data for registration purposes. Intraoperative MR images were rigidly registered to the pre-operative data using MR-visible fiducials placed around the craniotomy. The root

mean square position error after registration was reported to be between 0.39 mm and 2.3 mm.

An image based registration algorithm for iMRI was presented by Ferrant et al. [66]. A biomechanical finite element (FE) model driven by surface correspondances was used to estimate the deformation of the entire brain during surgery. The accuracy of the registration was evaluated using manually identified landmarks and resulted in a mean error of less than 1.6 mm. A second image based registration technique was published by Hastreiter et al. [67]. After having characterized the brain deformations, they used a non-linear registration method based on mutual information to register pre-operative and intra-operative data. The registration process made it possible to register pre-operative functional data such as fMRI, PET and MEG to the intraoperative MR images in 20-30 minutes.

Even though intra-operative MR imaging provides good quality images in reasonable time, this solution suffers from a number of disadvantages [68, 69]. Intra-operative MR imaging is a complex, expensive and sometimes quite a time consuming procedure. The intraoperative images may be of poorer quality than pre-operative MR images due to scanner design and short acquisition time. In general, intraoperative images are less complete, have lower resolution and are more susceptible to image distortions due to inhomogeneous magnetic fields when compared to pre-operative images. Another major shortcoming of this solution is the substantial financial investment required for the scanner as well as MR-compatible surgical instruments. These investments are justifiable for only a very limited number of hospitals. In addition, interventional MR scanners are

space-consuming and in many cases compromise the surgeon's access to the operating field.

5.2.5 Intraoperative ultrasound imaging

Intraoperative ultrasound imaging does not suffer from many of the limitations associated with interventional MRI. A high-end ultrasound scanner costs less than 10% of a typical MRI system and is already in use by many neurosurgeons. In addition, ultrasound systems are portable and compatible with existing surgical equipment. Despite these advantages, the use of ultrasound in neuro-navigation has been limited, probably due to poor image quality and the difficulty of interpreting such images.

Since the mid-1990's a number of groups have developed systems correlating intraoperative US with pre-operative MR. In a neurosurgical context, intraoperative ultrasound imaging can either be used directly as a surgical guide when brain-shift occurs or as a registration target for the pre-operative images in order to correct for deformations. These systems are described in more detail in the following background sections before presenting our registration method and validation experiments.

Direct ultrasound navigation

Grønningsæter et al. [14] developed a neuro-navigation system based on navigation solely by 3D ultrasound. This system also incorporates visualization of pre-operative MR and/or CT images, but uses only intra-operative 3D ultrasound for navigation if brain deformation occurs. Navigation by ultrasound images requires high quality images and display software in addition to well trained surgeons and technicians.

Manual registration of intraoperative ultrasound

Intra-operative ultrasound data can also be used in a less direct manner. Image registration techniques can be used to update pre-operative data. By registering pre-operative MR or CT images with intra-operative ultrasound images, complex deformations can be estimated and accounted for in the navigation system. For example, by identifying anatomical landmarks in the US images, and using a physical model of the brain, an elastic transformation can be calculated and applied to the pre-operative data. Comeau et al. [18] presented a surgical guidance system that incorporated pre-operative images with intraoperative ultrasound to detect and correct for brain-shift during neurosurgical procedures. Two dimensional ultrasound images were acquired during the operation and compared to the corresponding slice from the pre-operative data set. A method was presented to manually identify homologous landmarks in ultrasound and MRI in order to construct a set of displacement vectors that would allow the pre-operative MR image to be warped to match the intra-operative ultrasound image. The mapping procedure was demonstrated to have an accuracy better than 2 mm. Gobbi et al. [71] demonstrated a similar technique where manually placed landmarks and a thin-plate spline interpolation were used to deform the MR volume to match the ultrasound volume.

Automatic registration of intraoperative ultrasound

Several automatic registration procedures have also been developed, in order to minimize the need for user intervention and speed up the procedure, which is particularly important for intraoperative registration. Roche et al. [52] estimated the rigid body transform required to linearly align pre-operative MR images and intra-operative US images. They correlated the US intensities with both the MR intensity and the MR gradient magnitude

using a variant of the correlation ratio and a robust distance measure. The algorithm was tested on two clinical datasets and one phantom dataset. Because no gold standard was available, registration loops involving both the ultrasound and MR data were used. In the ideal case each loop should lead to the identity matrix. They reported registration residuals up to 1.65 mm in translation and 1.57° in rotation and a computation time of 5-10 minutes.

In order to correct for non-linear deformation Arbel et al. [50, 51] used a tracking system to reconstruct 3D volumes from a series of US images in the same space as the pre-operative MR-image. From the pre-operative MR images, they created pseudo-US images that closely resembled real US images of the same structures acquired during surgery. They then used an intensity based non-linear registration technique to match tracked intraoperative US images with the pseudo-US images to detect and correct brain deformations. Qualitative results from 12 surgical cases showed that the technique was able to account for a large portion of the deformations.

Registration of intraoperative US with pre-operative MR is a challenging registration problem due to very different underlying physical principles and thus different image characteristics. Image intensities, noise characteristics, contrast, volume coverage and dimensionality are only a few main differences between a typical pre-operative MR image and a corresponding intraoperative ultrasound acquisition.

5.2.6 Vessel-based registration

To try to overcome some of the difficulties discussed in the previous section, we explore a different approach to this particular registration problem. The idea is to use homologous features in the two datasets as "landmarks". Such features might be

any segmented structures present in both images such as organ surfaces and vascular structures. In this project we investigate the use of blood vessels segmented from pre-operative angiographic images and Doppler US for registration purposes. The cerebral vasculature is relatively easy to identify and segment from pre-operative angiographic data such as MR angiograms (MRA). A method to segment vessels from other types of MR aquisitions such as proton density (PD) images or gadolinium (Gd) enhanced MR images has been presented in [72]. Segmentation of Doppler ultrasound images can easily be performed by simple thresholding although this often produce vessels with a too big radius due to noise from moving vessel walls. By using the centerlines of the vessels this problem is largely overcome.

The cerebral vasculature is a good candidate for use in image registration because the vessels are distributed all over the cerebral cortex and inside the brain and move with the surrounding tissue. The brain deformations are therefore well captured by the vasculature. In addition, blood vessels will be present in any region of interest (ROI) throughout the brain. The probability of not finding reliable landmarks in a given ROI is therefore low. Keeping track of important vessels during surgery also provides the surgeon with important reference points in order to avoid major vessels during the procedure and monitor blood supply to specific areas of the brain. This approach has already been investigated by a number of different groups for several different purposes. Porter et al. [73] rigidly registered MRI with B-mode and color Doppler ultrasound volumes based on segmented blood vessels from the forearm, the liver and a prostate phantom. The skin surface, bone and internal landmarks were used to evaluate the registration error which ranged from 2 to 8 mm.

Another rigid body registration technique based on vasculature was presented by Slomka et al. [74]. The carotid bifurcation of six patients was imaged with B-mode and Power Doppler ultrasound as well as MRA. The mean errors were 0.32 mm in translation and 1.6° in rotation based on a series of anatomical landmarks for initial misalignments of up to 5.4 mm in the x and y directions, 10 mm in the z direction and rotations up to 40°. The algorithm was not affected by missing arterial segments of up to 8 mm, but would fail if the bifurcation was missing from either dataset.

A third rigid body registration technique as well as a vessel segmentation algorithm was presented by Aylward et al. [75]. A registration metric was defined based on the parameters of the vessel segmentation algorithm and used to register CT images of the liver and pre and post-surgery MRA images of the brain. A series of Monte Carlo simulations was conducted to measure how consistently the registration method was able to align segmented vessels from the liver given random initial misregistrations. The application of this registration algorithm was extended to include CT to ultrasound registration [76] and then further extended to take into account non-linear deformations [77]. Following global rigid registration, each branch in the vessel tree was linearly registered resulting in a piece-wise rigid transformation. The alignment was then further refined with a deformable registration method. The results showed that the 87% of the centerline points in the model were within 2 voxels of the centerlines in the target image.

A more recent technique to register MR and B-mode ultrasound images of the liver based on vasculature was presented by Penney et al. [78]. The rigid registration used ultrasound images to establish the correspondence between the MR volume and the patient on the operating table. This corresponds to the rigid registration usually performed by

identifying homologous landmarks on the patient's head and on the pre-operative images before neurosurgical procedures. The results showed that the method was accurate to within an RMS error of between 2.3 and 5.5 mm with respect to a "bronze standard" registration calculated by manually picking points in both modalities.

The algorithm described in this paper is designed to register pre-operative MR images and intra-operative US images of the brain in order to correct the brain-shift occurring during neurosurgical procedures. The work is based on experiments first presented in [85] where we demonstrated that it was possible to use vessel-based non-linear registration for this task. In this paper, we have further developed and improved our vessel-based registration method and present experimental validation of the technique. We have replaced the free-form ANIMAL-based deformation [86] with a thin-plate spline transform to improve regularization of the deformation. We now use a modified version of the ICP algorithm to register vessel centerlines extracted from MR and Doppler ultrasound data. In order to reduce the number of outliers, we have incorporated the least trimmed squares (LTS) robust estimator [112]. Therefore, our method effectively reduces the number of incorrect pairings without limiting the capture range of the registration algorithm. While our algorithm shares some similarities with the procedure described by Lange et al. [79], there are some important differences. Our procedure is applied to interventional brain imaging, while Lange's technique was applied to liver. Both techniques use segmented vessel centerlines to drive the registration. Our technique uses LTS robust estimation to reject outlier points instead of a the user-defined distance threshold used by Lange. Both techniques use spline-based regularization of the deformation; we use a thin-plate spline

while Lange uses B-splines. Finally, Lange estimated the quality of registration quantitatively based on the RMS distance of vessel-points and semi-quantitatively based on structure boundaries. Our main contribution in this paper is a more thorough quantitative validation using data with simulated deformations and real MR and US data from a novel deformable anthropomorphic poly vinyl alcohol cyrogel (PVAc) brain phantom.
This paper is organized into five sections. In section 5.3, the vessel segmentation method and the centerline extraction technique are briefly decribed, and the registration algorithm is presented in detail. Section 5.4 is concerned with the validation experiments using simulated and phantom data. A discussion of the results is given in section 5.5, and finally our conclusions are presented in section 5.6.

5.3 Methods

5.3.1 MR vessel segmentation

We used a new multi-scale geometric flow for segmenting vasculature in the MR images of the phantom. The method can be summarized in three steps: First, the method applies Frangi's vesselness measure [91] to find putative centerlines of tubular structures along with their estimated radii and orientation. Second, this multi-scale measure is distributed to create a vector field which is orthogonal to vessel boundaries. Finally, the flux maximizing flow algorithm [92] is applied to the vector field to recover the vessel boundaries. This technique overcomes many limitations of existing approaches in the literature specifically designed for angiographic data due its multi-scale tubular structure model. It has a formal motivation, is topologically adaptive due to its implementation using level set methods, is computationally efficient and requires minimal user interaction. The technique is detailed in [72].

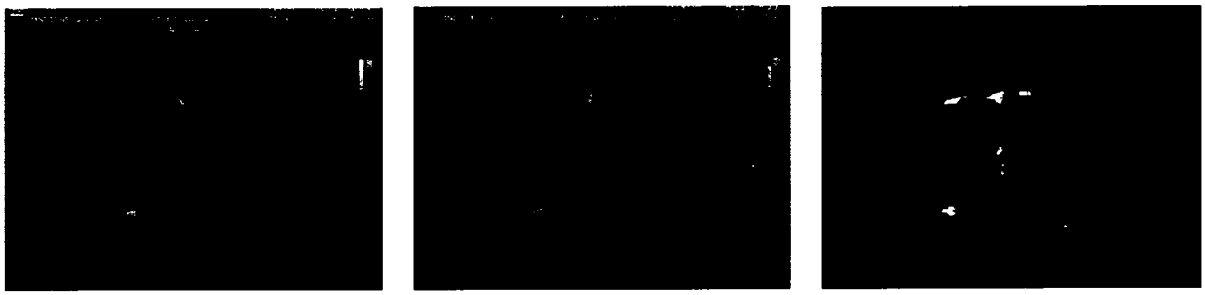

Figure 5–1: An example of an ultrasound image before and after segmentation (right and middle) and after masking (left).

5.3.2 US vessel segmentation and volume reconstruction

When scanning using Doppler ultrasound imaging, the Doppler signal and the B-mode signals are combined on the display of the ultrasound scanner. The Doppler signal is displayed in color, and the B-mode signal is displayed in grayscale. Segmentation of the ultrasound images was therefore obtained by extracting all colored pixels from the original images. A simple filter was implemented that would set to zero all pixels with a saturation equal to zero (Hue-Saturation-Value color model), which constitutes the grayscale. Following segmentation, the 2D images were masked, converted to grayscale, and finally reconstructed into a 3D volume. The 3D volume was then thresholded again to produce a binary image. An example of an ultrasound image before and after segmentation and after masking is shown in Figure5–1. The 2D slices were interpolated to a uniform grid using a Kaiser-Bessel function as the interpolation function and an isotropic regrid radius of 2 mm.

5.3.3 Centerline extraction

Following segmentation, we extracted the vessel centerlines using a fast, robust and automatic method based on medial surfaces. The technique uses the average outward flux

of the gradient vector field of the distance transform of the object to compute the medial surface [93]. The centered medial curves are then obtained by topology preserving thinning ordered by the distance function to the object's boundary. This ensures that the remaining points lie on the medial surface and as far away from the vessel boundary as possible. The medial curve was finally pruned based on length to remove superfluous branches and obtain a single curve for each vessel branch. Details on the method can be found in [94].

5.3.4 Registration algorithm

After segmentation and centerline extraction, the MRA image and the Doppler ultrasound volumes are binary images representing the vascular tree. The vessels are in the form of a "skeleton" representing the midlines. The two datasets are only partially overlapping, and vessels are not necessarily continuous. A number of vessels might also be missing from one or both data sets. The task of registering the two datasets using a modified version of the original ICP algorithm presented by Besl and McKay [95], can be summarized in the six following steps as proposed by Rusinkiewitcz at al. [99]:

1. Sampling
2. Point matching
3. Weighting/Rejecting point pairs
4. Estimating the transformation
5. Applying transformation to the source points
6. Calculating the error

Sampling

There are multiple ways of sampling the extracted centerlines. The simplest method proposed in the original ICP algorithm is to use all available points. Since then, a number of other sampling strategies have been presented in order to improve the convergence rate, reduce sensitivity to noise and missing data or to adapt to particular types of images. Turk et al. [96] created triangle meshes from laser range images and used the ICP algorithm to bring corresponding portions of meshes from different images into alignment with one another in order to create a single polygonal mesh that completely describes the outside part of the scanned object. The creation of triangle meshes represents a uniform sub-sampling of the images. Sub-sampling of the images is an efficient way of reducing computation time, but depending on the sampling frequency, accuracy may be compromised. A different method of sub-sampling is to choose a number of points extracted at random. Masuda et al. [97] used this technique with a different subset of points at each iteration in order to provide different starting positions for the algorithm. Other possibilities include selecting points with high intensity gradients [98] or choosing points such that the distribution of normals among selected points is as large as possible [99]. in order to obtain more points in regions with small features critical to determining the correct alignment. In line-to-line registration, such features could be regions with high curvature or bifurcations. In this paper we start with all available source points and then selects points based on the distance to the target. As an option it is possible to perform a uniform sub-sampling of the selected points in order to speed up the computation.

Point matching

The next step addresses the problem of finding corresponding points in the source and target point sets. Because the ICP algorithm is is sensitive to the source vs. target selection, the source should always have fewer points than the target. In the original ICP algorithm, the simple Euclidean distance was used to find the closest point in the target dataset. The closest-point algorithm tends to produce a large number of incorrect pairings when the images are relatively noisy or do not completely overlap. This sensitivity to noise and missing data is one of the main disadvantages of the original ICP algorithm. Because noise and missing data are problems frequently encountered in real images, a number of point matching techniques have been developed in order to increase the robustness of the registration algorithm. Possible approaches used in the past are to find the intersection of the ray originating at the source point in the direction of the source point's normal with the destination surface, or different projection methods such as projection of the source point onto the target followed by a local search based on distance or intensity [101]. Rusinkiewitcz et al. [99] found that the projection-based algorithms converged significantly faster than for example the closest point method. In their experiments, convergence was reached in between 10 and 20 iterations. In the experiments presented in this paper, we reached convergence in less than 35 iterations in all cases, and linear registration was completed in less than 15 seconds which was considered satisfactory. We have therefore chosen to keep the original point matching technique based on the Euclidean distance and minimize the number of incorrect pairings by implementing the least-trimmed squares estimator as explained in the following section.

Weighting and rejecting point pairs

The idea behind the assignment of weights or completely discarding certain point pairs is to limit as much as possible the influence of erroneous pairings on the transform computation. Efforts are made to reduce the number of such pairs through sampling and point matching strategies, but when dealing with noisy data where the overlap is not complete and data are missing as is the case here, efficient weighting and rejection techniques may considerably improve the final result. Without any weighting and/or rejection strategy, all pairs will be used and all points will be equally weighted. A simple modification to this method is to assign lower weights to pairs with greater point-to-point distance, and to possibly reject corresponding points more than a given distance apart. Another method proposed in the past is weighting based on the compatibility of normals. The weight is then calculated as the scalar product of the normals. Point pairs with colinear normals will have weights equal to one, and point pairs with perpendicular normals will be rejected.

Other strategies include rejection of pairs whose point-to-point distance is larger than some multiple of the standard deviation of distances, or rejection of pairs that are not consistent with neighboring pairs. A potentially very useful strategy is to remove pairs that include points on boundaries. These pairs may introduce a systematic bias in the estimated transform in cases where the overlap is not complete.

A method widely used in computer vision is the random sample consensus (RANSAC) algorithm introduced by Fischler et al. [100]. The method selects a subset of the data to estimate the parameters of the model to fit. The subset is selected at random, and the algorithm determines the number of samples that are within an error tolerance. If the

number of samples within the error tolerance is high enough, the solution is kept. The process is repeated and the solution with the smallest error is kept as the final model. The number of iterations required increases with the size of the sample subset and the percentage of outliers in the data.

Another possibility is to use robust regression methods such as the Least Median of Squares (LMS) [102] or the Least Trimmed Squares (LTS) [103]. While the least squares technique minimizes the sum of squared residuals, the LMS minimizes the median of squared residuals. The LTS method on the other hand, is based on sorting and trimming the sequence of squared residuals. The squared residuals are sorted, and the points corresponding to the n% greatest distances are rejected. The percentage is user defined and can be adjusted according to the amount of noise or missing data expected in the dataset. The transformation is then calculated based on the remaining pairs, and the result is applied to the entire dataset. These two steps are then iterated until convergence. The LTS method is usually preferred to the LMS because it has a better convergence rate and a smoother objective function [112]. LTS and LMS have the same breakdown point of 50%, which means that the number of outliers in the dataset cannot exceed 50%.

Transformation

Most of the registration methods using a variant of the ICP algorithm estimate a rigid body transform (3 translations and 3 rotations). For linear registration, we have also included isotropic scaling, which gives a total of 7 parameters. While this might be sufficient in cases of motion detection or to provide a good starting position for non-linear registration, it is not enough to describe the highly complex brain deformation taking place during neurosurgical interventions. The deformation is non-linear, and

single points can move as far as 50 mm from their initial position. One possibility is to use a thin-plate spline (TPS) transformation [113]. TPS is an interpolation method that finds a "minimally bended" smooth (hyper)surface that passes through all given points. TPS are particularly popular in representing shape transformations, for example in image morphing or shape detection. In this work, we use the thin-plate spline transformation with points selected as described above, to represent the non-linear component of the deformations. The interpolation can be regularized using a scaling parameter σ that will determine the "stiffness" of the spline. In this work, we start by estimating a 7 parameter linear registration. In neuronavigation, this linear transformation is required due to the error in the landmark-based registration performed prior to the opening of the skull and the actual linear component of the brain deformation occurring after the craniotomy. Then, the linear registration is refined by re-running the algorithm and using a thin-plate spline transform to correct the non-linear component of the deformation.

Registration error

In the original ICP algorithm, the mean squared error was used and the algorithm was proved to converge to a local minimum of the objective function in terms of this error metric. A "point-to-plane" metric can also be used by taking the sum of squared distances from each source point to the plane containing the target point and oriented perpendicular to the target normal [115]. The robust estimators LMS and LTS also converge to a local minimum of the objective function depending on the starting position [112]. The thin-plate spline transform needs to have a reasonably good starting point, in terms of correct point pairings in order to give a satisfactory result. In most cases involving registration of pre-operative MR and intra-operative ultrasound, the two

modalities will be linearly registered at the beginning of the procedure. This initial registration can be corrected by performing a linear ICP registration with 7 parameters as described above. In cases where there is no initial linear registration, or if the ultrasound probe is not tracked during the procedure, it is possible to manually perform a coarse linear registration by dragging the source dataset into place.

For the linear registration, the steps described in section 5.3.4 to 5.3.4 need to be iterated until a stopping criterion has been met. In previous literature, this criterion is usually a fixed number of iterations, an error metric below a pre-defined threshold or the difference between two successive error measurements below a pre-defined threshold. In this work, the iterations are stopped when the difference in mean distance between the source points and their closest target point between two successive iterations is smaller than 0.0001mm.

Algorithm

In this project, we have chosen to use the least trimmed squares and the simple Euclidean distance for point matching. The algorithm can be summarized in four steps:

1. Find the closest point in the target dataset for each source point.
2. Sort the distances, and select the source points corresponding to the n% smallest distances.
3. Estimate a 7 parameter linear transform **or** a thin-plate splines deformation based on the selected points.
4. Apply the transformation to the entire dataset.

5.4 Experiments and Results

In order to validate the registration algorithm presented above we performed two sets of experiments. First, we simulated fourteen realistic brain deformations in order to test the algorithm in a situation where the ground truth is known. Second, we performed a phantom study with a deformable brain phantom in order to come closer to a realistic clinical situation and to test the registration technique with real ultrasound data.

5.4.1 Simulations

Data pre-processing

For the simulation experiments, a standard phase-contrast MRA (TR=71 ms, TE=8.2 ms, flip angle=15°) from a normal volunteer with full brain coverage and a voxel size of $0.5 \times 0.5 \times 1.5$ mm was used. The original dataset was resampled using tri-linear interpolation to an isotropic voxel size of 0.5 mm. A series of 22 landmarks were placed at random spots throughout the volume and 4 landmarks were placed on the surface of the cortex in a square just above and below the right lateral fissure. These four landmarks were then manually displaced from plus or minus 2 to 20 mm in the x-direction(left-right direction). These deformations represent a smooth expansion or contraction toward the midline of the brain as shown in Fig. 5–3. A thin-plate spline transform was computed between the original 26 landmarks and the 26 landmarks where four points had been displaced. The resulting transform was then applied to the resampled MRA dataset in order to obtain a deformed version of the same brain. Thus, the thin-plate spline transform represents the ground truth in these experiments, and the two datasets (resampled and deformed) will be used to estimate the deformation.

In order to simulate a typical ultrasound acquisition, a 4.5 cm rectilinear scan path was defined between two points on the cortical surface in the region of interest on the MRA. The region of interest is shown by the rectangular box in Fig. 5–3. Two points inside the brain were manually selected to determine the direction of the first and last image plane. The orientation of the image planes was perpendicular to the scan path. The dimension of the image planes was 50 mm wide, a depth of 40 mm and a thickness of 3 mm, with a voxelsize of $1 \times 1 \times 3$ mm and 2 mm between each slice. The slice was averaged over 3 mm in the scan direction to simulate the thickness of the ultrasound beam. The individual slices were thresholded to segment vessels and then masked using a wedge-shaped mask to simulate the shape of real ultrasound images. The masked images were then recontructed into a volume using the reconstruction algorithm described in section 5.3.2. Following volume reconstruction centerlines were extracted. The original MRA dataset was then segmented using the algorithm described in section 5.3.1. The vessel centerlines were extracted from the segmented data, and used as input to the registration algorithm. In order to reduce the noise in the extracted centerlines (single points not connected to the vessel tree), points located more than 5 mm from their closest neighbor were removed from the image prior to registration. The resulting vessel tree is shown in blue in Fig. 5–3.

This technique of simulating ultrasound data from MR images is similar to the method proposed by Arbel et al. [50, 51]. They created pseudo ultrasound data from pre-operative MR images in order to facilitate intensity based registration of intra-operative ultrasound data.

Registration

In this experiment the simulated ultrasound volume represents a part of the middle cerebral artery that has been shifted and deformed compared to the target image which represents a nearly complete arterial "tree". Because the simulated ultrasound volume contained fewer points than the original MR dataset, it was considered the source image in this experiment. In order to recover the deformation, the source image was first linearly registered to the target in order to provide an optimal position for the non-linear deformation. In this step, between 80 and 99% of the available source points were used. The iterations were stopped when the difference in mean distance between all source points and their closest target point between two successive iterations was smaller than 0.0001mm. The mean distance as a function of iteration number for all 14 linear registrations is shown in Figure 5–2.

The registration was then further refined by non-linear registration, where 55 to 99% of the source points were used and a σ between 0.5 and 1.5. An example of the registration is shown in Fig. 5–3. To evaluate the performance of the registration technique, the recovered transformations were compared with the ground truth thin-plate spline transform applied. We computed the 3D root-mean-square (RMS) of the difference between the two transforms over every third voxel in the region of interest (ROI). In addition, a series of ten landmarks placed in the highly deformed region were used to specifically estimate registration accuracy in the ROI. The percentage of the deformation recovered by the registration algorithm was calculated in each case using the following formula:

$$\% = \frac{(RMS_{Before} - RMS_{After}) \times 100}{RMS_{Before}} \tag{5.1}$$

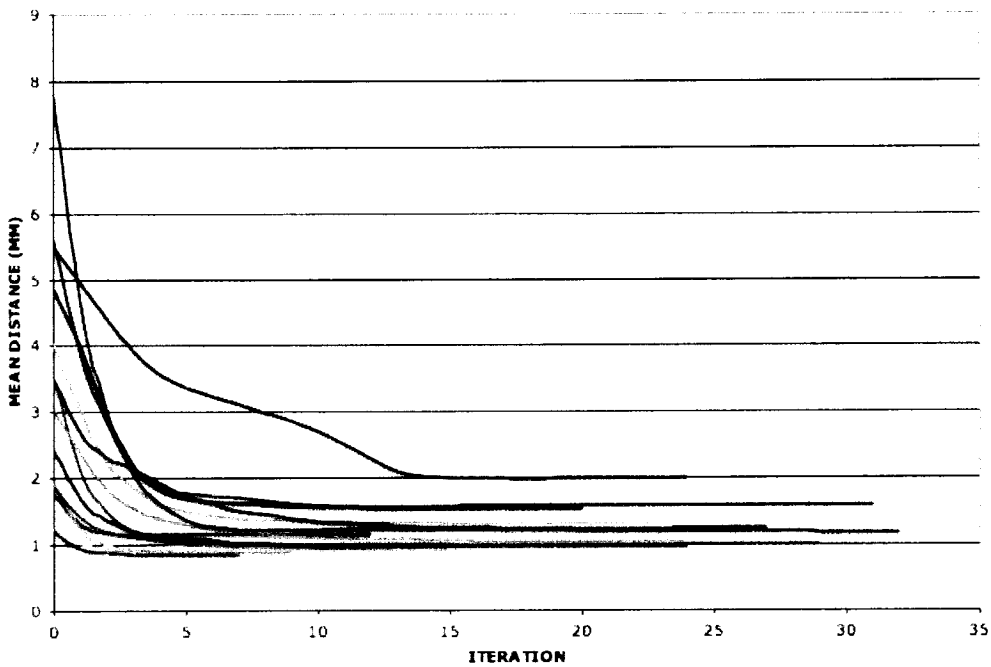

Figure 5–2: Mean distance (mm) between all source points and their closest target point as a function of iteration number for the linear registrations. Iterations were stopped when the difference in mean distance between two successive iterations was smaller than 0.0001mm.

For the landmarks, the RMS in Equation 5.1 should be replaced by the mean distance between landmarks.

The results are presented in Table 5–1 and Table 5–2. These results show that the technique was capable of recovering on average 76% of the deformations ranging from 2 to 20 mm, by measuring the distance between landmarks, and 73% by estimating the RMS over the ROI.

Table 5–1: Mean±std distance between ten source and target landmarks before registration, after linear registration and after non-linear registration. All measurements in mm.

Displ. (mm)	Mean±std before reg.	Mean±std after linear reg.	Mean±std after non-lin. reg.	**% of def. recovered by reg.**
-20	15.66±2.85	2.83±1.57	2.69±1.66	**83%**
-15	11.63±2.27	2.14±1.31	1.88±1.06	**84%**
-10	7.65±1.62	1.63±1.10	1.43±0.61	**81%**
-8	6.08±1.33	1.32±0.71	1.19±0.54	**80%**
-6	3.15±1.60	1.53±1.13	1.47±0.98	**53%**
-4	3.00±0.71	1.02±0.46	0.86±0.34	**71%**
-2	1.49±0.36	0.54±0.32	0.52±0.31	**65%**
2	1.47±0.39	0.52±0.10	0.37±0.14	**75%**
4	2.91±0.79	0.81±0.43	0.74±0.24	**75%**
6	4.33±1.22	1.30±0.65	1.17±0.46	**73%**
8	5.73±1.66	1.55±0.99	1.05±0.38	**82%**
10	7.10±2.13	2.08±1.22	1.56±0.52	**78%**
15	10.41±3.41	2.88±1.66	2.11±0.85	**80%**
20	13.54±4.83	3.64±1.59	2.86±1.24	**79%**

Table 5–2: 3D RMS before registration, after linear registration and after non-linear registration evaluated over the region of interest (ROI). All measurements in mm.

Displ. (mm)	RMS (ROI) before reg.	RMS(ROI) after linear reg.	RMS(ROI) after non-lin. reg.	**% of def. recovered by reg.**
-20	14.81	2.63	2.46	**83%**
-15	10.98	2.14	1.96	**82%**
-10	7.21	1.66	1.59	**78%**
-8	5.73	1.29	1.27	**78%**
-6	3.09	1.63	1.55	**50%**
-4	2.83	0.96	0.92	**67%**
-2	1.40	0.54	0.54	**62%**
2	1.38	0.52	0.36	**74%**
4	2.74	0.84	0.71	**74%**
6	4.08	1.33	1.19	**71%**
8	5.40	1.65	1.29	**76%**
10	6.69	2.15	1.59	**76%**
15	9.82	3.07	2.18	**78%**
20	12.79	4.64	3.74	**71%**

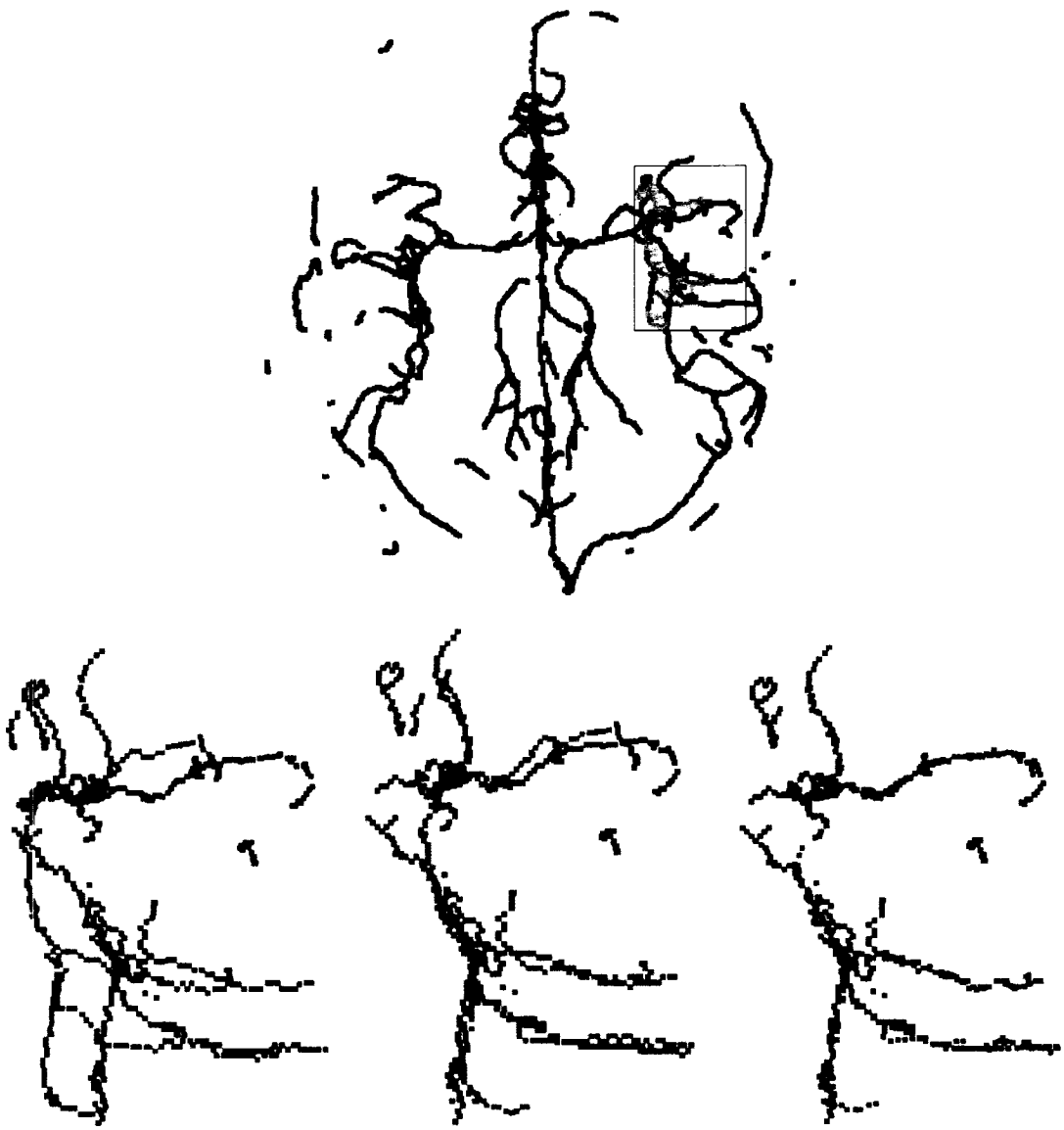

Figure 5–3: The centerlines extracted from the simulated ultrasound volume registered to the MR vessel tree (top). Before registration (bottom left), after linear registration (bottom middle) and after non-linear registration (bottom right). In the upper image target points are in blue, source points that participate in the registration are in green and source points that don't participate in the registration are in red. The yellow lines illustrate the closest point correspondances for the points that participate in the registration.

5.4.2 Phantom study

Phantom preparation

To further evaluate and validate the registration technique in a situation closer to a real clinical setting, we performed a phantom study. The phantom was made of polyvinyl(alcohol)-cryogel (PVAc), and was designed to resemble a hemisphere of the human brain. To prepare the PVAc, the technique proposed by Surry et al. [54] was applied. An inflatable 5 ml Bardex Foley catheter (C. R. Bard, Inc., Covington, GA) was placed under the phantom to simulate a brain lesion, and plastic tubes with inside diameters of 1.57, 2.36 and 3.18 mm were inserted to simulate blood vessels. By inflating or deflating the catheter balloon, the phantom would deform in an elastic non-linear manner. A detailed description of the phantom as well as a thorough study of the reproducibility of the deformations can be found in [2]. The phantom made it possible to test the registration algorithm and segmentation technique as well as the ultrasound imaging setup and the navigation software in a setting with known geometry and simpler deformations than in the human brain. Because both MR and ultrasound images of the phantom were obtained both in the original and two deformed states, it was possible to validate the US based registration by comparing it to MR based registration. In this experiment, the MR based registration would therefore serve as a gold standard in order to validate the ultrasound based registration. A photo of the phantom is shown in Fig. 5–4

MR imaging and vessel segmentation

The phantom was scanned using a Siemens SonataVision 1.5T scanner using a standard T1 weighted anatomical scanning sequence (TR=22 ms, TE=9.2 ms, flip angle = 30°)

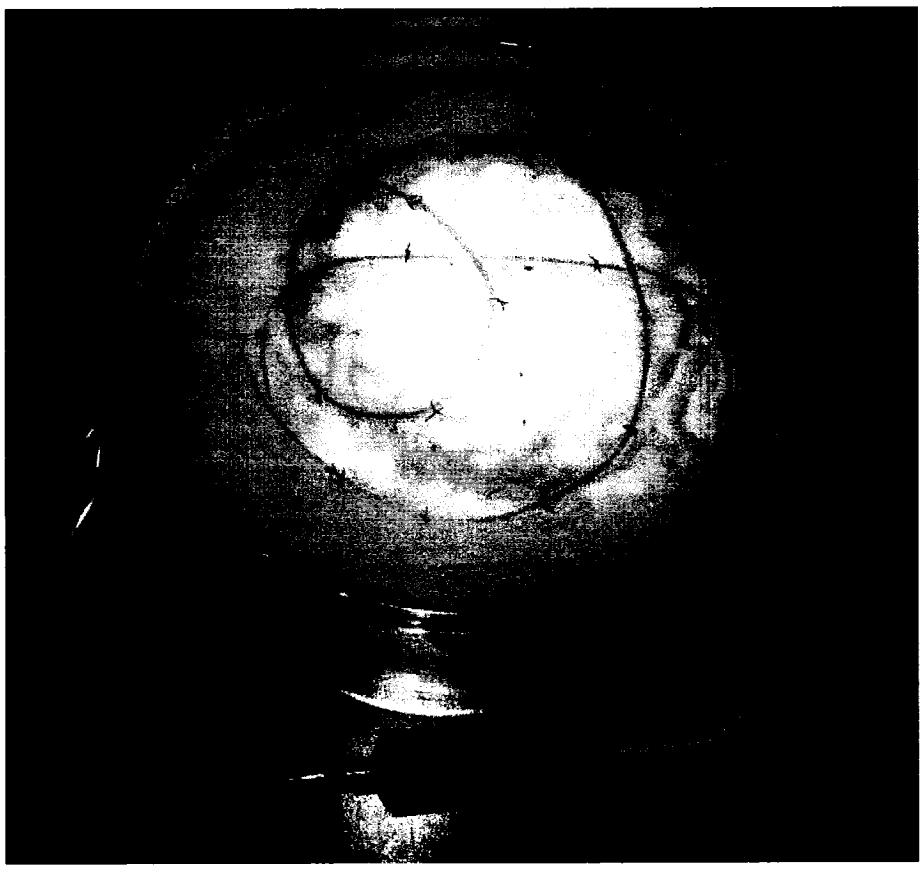

Figure 5–4: The PVA phantom in a plastic container. The syringe was used to inject water into the catheter balloon to deform the phantom.

with full brain coverage and 1 mm isotropic resolution. The phantom was scanned six times: twice for each catheter balloon volume filling (0 ml, 5 ml and 10 ml). The catheter was either inflated or deflated between each scan. The inflation or deflation of the balloon deformed the phantom in a non-linear fashion as shown in Figure 5–5. During MR imaging the phantom remained in the plastic container and the plastic tubes were filled with water. For technical reasons there was no flow in the tubes during imaging, but due to the contrast between the PVA (bright), the tubes (dark) and the water inside

the tubes (bright) it was still possible to apply the segmentation algorithm described in section 5.3.1. In order to be able to segment the smaller tubing, the original image was supersampled to 0.5 mm^3 isotropic resolution. The smallest tubes used in the phantom have an inside diameter of 1.57 mm. Unfortunately these tubes were too small for the automatic segmentation algorithm to detect. To overcome this problem, parts of the smallest tubes were segmented manually. Following segmentation, centerlines were extracted using the algorithm described in section 5.3.3. A surface rendering of the phantom with the segmented tubes is shown in Fig. 5–6.

US imaging and segmentation

Free-hand ultrasound images were then acquired using an HDI 5000, Philips Medical Sytems (Bothwell, WA) ultrasound machine with a Philips P7-4 multi-frequency probe. Tracking was achieved with the Polaris optical tracking system (Northern Digital Inc., Waterloo, ON), a passive reference and an passive tracker device (Traxtal Inc., Toronto, ON) attached to the ultrasound probe. The position and orientation of each 2D image were recorded and used to reconstruct a 3D volume as described in section 5.3.2. A physiological pump (Manostat Corp., New York City, NY) was used to pump water through the plastic tubes while the phantom was scanned using color Doppler imaging. The plastic container with the phantom was filled with water, and the phantom was allowed to rest for a few minutes for air bubbles in the water to disappear. This procedure is analogous to the one used in surgery when the craniotomy is filled with sterile water prior to ultrasound imaging. During Doppler imaging, the Doppler signal is overlaid on the regular B-mode ultrasound image. The gain of the B-mode signal was therefore turned down to facilitate the extraction of the "vessels" from the images afterwards. The

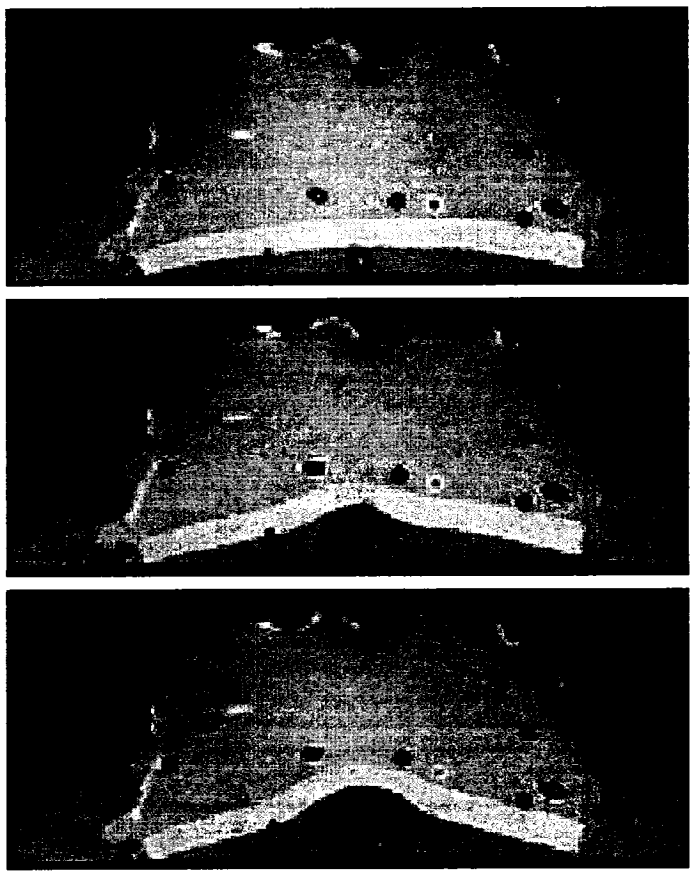

Figure 5–5: MR images of the phantom with empty catheter balloon (top), half-full catheter balloon (middle) and full catheter balloon (bottom).

phantom was scanned with catheter balloon filled with volumes of 0, 5 and 10 ml of water. The two dimensional ultrasound images were masked to remove all data outside the ultrasound image wedge, and then thresholded to separate the Doppler signal from the B-mode image. The slices were then resampled into a 3D volume. Following volume reconstruction, centerlines were extracted using the algorithm described in section 5.3.3.

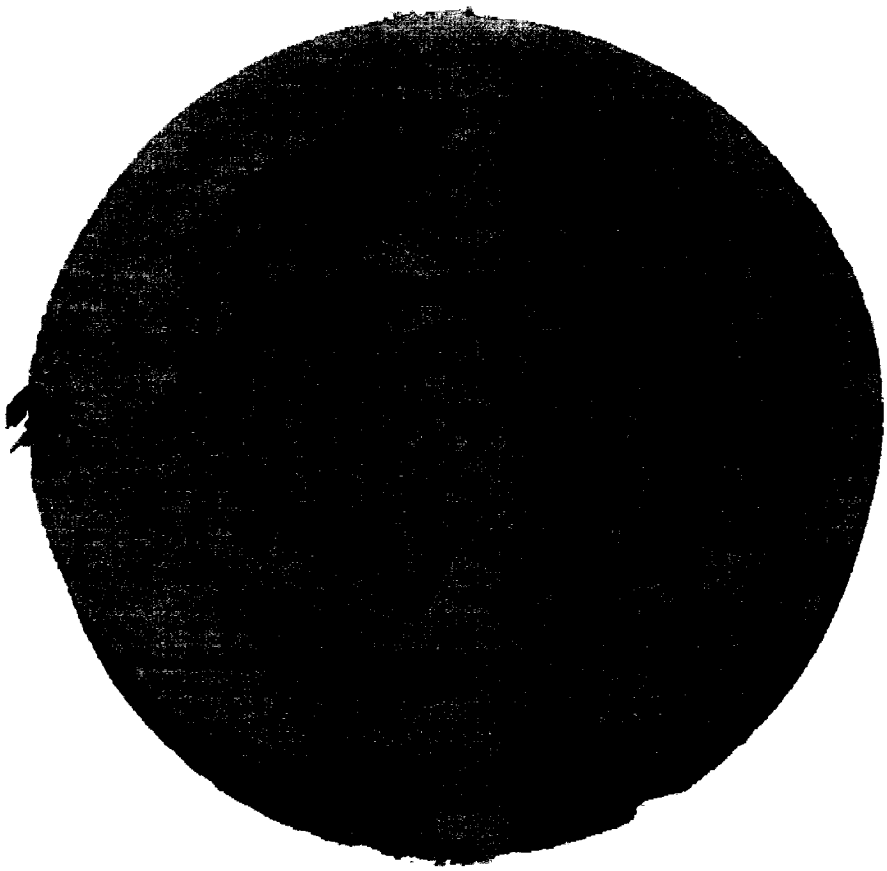

Figure 5–6: A surface rendering of the phantom with the segmented tubes in red.

Linear registration

Prior to ultrasound imaging, the phantom was linearly registered to the MR images by identifying four homologous landmarks on the phantom container and in the corresponding MR image. In order to improve this initial alignment we performed a linear registration between the ultrasound and MR images with corresponding catheter balloon volumes as described in section 5.3.4. In this case the ultrasound volume was considered the source volume and the MR volume the target because the ultrasound volume

contained fewer vessels than the MR volume. Based on the results presented in Figure 5–2, the iterations were stopped after 20 cycles. As we had 6 MR volumes and only 3 ultrasound volumes, each ultrasound volume was registered to both MR volumes with corresponding deformation, resulting in 6 linearly registered ultrasound volumes. These volumes provided the starting points for the non-linear registration described in the following section.

Non-linear registration

The centerlines of the MRI data and the US data were registered using the technique described in section 5.3.4. Between 55% and 99% of the available points were used for registration. We used a scaling parameter σ between 0.7 and 1.2. To decrease the computation time, the data were sub-sampled by a ratio between 0.5 (every second point) to 0.25 (every fourth point). The percentage of source points used, the sample ratio and σ were manually optimized for each registration depending on the amount of noise, missing vessels and volume covered by the ultrasound. One example of the original centerlines extracted from the two volumes and the centerlines with the selected points and the initial pairings is shown in Figure 5–7. We performed non-linear registrations between all the linearly registered ultrasound volumes to all MR volumes resulting in a total of 24 registrations.

In order to validate the accuracy of the registration we used a series of 10 homologous landmarks. Because it was very difficult to identify points in the ultrasound volume accurately, we tracked a series of points as they were deformed in the MR volumes. We identified 10 landmarks in all six MR volumes. These points were air bubbles in the PVA and less than 2 mm in diameter. They were clearly visible in all scans. The landmarks

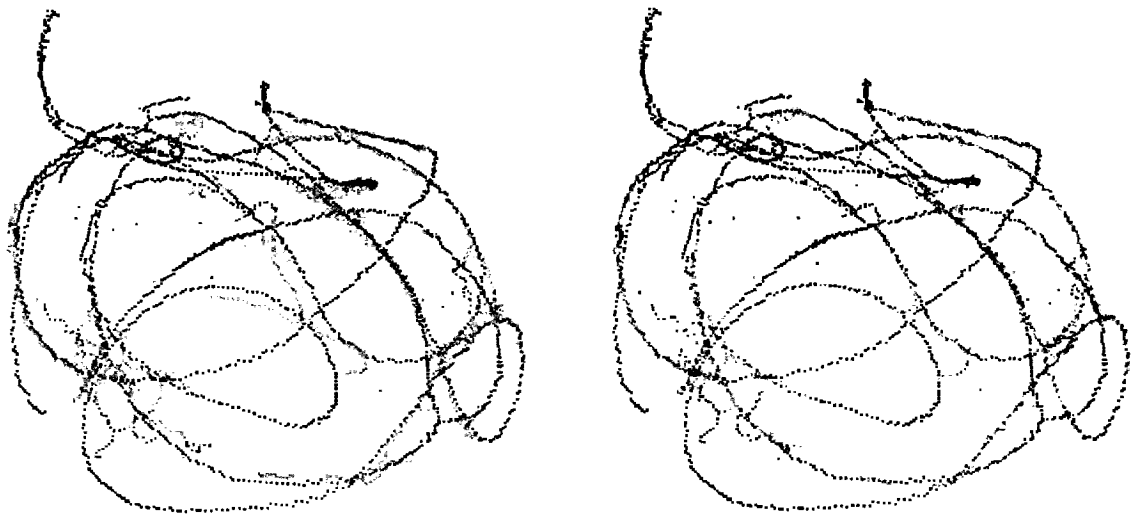

Figure 5–7: US-MR registration: before (left) and after (right) non-linear registration. Target points are in blue, source points that participate in the registration are in green and source points that don't participate in the registration are in red. The yellow lines illustrate the closest point correspondances for the points that participate in the regitration.

were located in the region of the phantom that deformed the most when the catheter balloon was either inflated or deflated. They were placed between "vessels" and did not participate in the registration. The transformation recovered after each non-linear registration was used to warp the landmarks identified in the source image, and the distances between the warped landmarks and the real landmarks identified in the target image were recorded. The mean distances of the landmarks in the source and target image before non-linear registration is shown in Table 5–3, and the distances between the warped landmarks and the landmarks in the target image are shown in Table 5–4. For comparison and in order to establish a lower bound on the registration error, we repeated the non-linear registrations using only MR data. One example of the MR-to-MR

registration is shown in Figure 5–8. In this case, we had full volume coverage for both source and target datasets and the overlap of the segmented vessels was nearly complete.

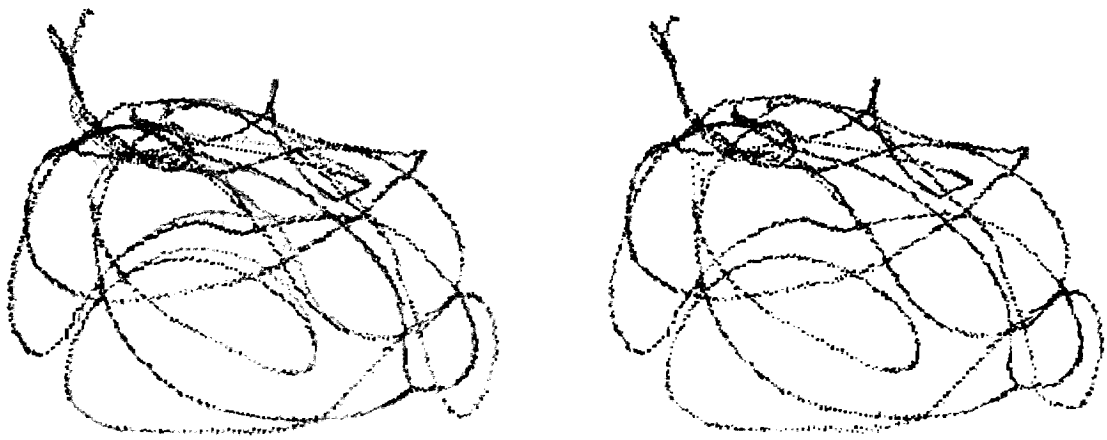

Figure 5–8: MR-MR registration: before (left) and after (right) non-linear registration. Target points are in blue, source points that participate in the registration are in green and source points that don't participate in the registration are in red. The yellow lines illustrate the closest point correspondances for the points that participate in the regitration.

The mean distances between the warped landmarks and the real landmarks identified in the target image are shown in Table 5–5 for the MR-MR experiment. Overall, these results show that we were able to correct the non-linear deformations with an average residual error of 1.6 mm for the ultrasound based registration. For comparison, the technique corrected the same deformations with an average residual error of 1.07 mm for the MR-to-MR registration.

Table 5–3: Mean±std distance in mm between the 10 landmarks before non-linear registration

	0ml-1	0ml-2	5ml-1	5ml-2	10ml-1	10ml-2
0ml-1	×	×	1.64 ± 0.56	1.79 ± 0.78	3.69 ± 0.94	3.83 ± 1.00
0ml-2	×	×	1.64 ± 0.73	1.78 ± 0.77	3.69 ± 1.02	3.83 ± 1.07
5ml-1	1.64 ± 0.56	1.64 ± 0.73	×	×	2.13 ± 0.69	2.32 ± 0.64
5ml-2	1.79 ± 0.78	1.78 ± 0.77	×	×	2.02 ± 0.40	2.21 ± 0.44
10ml-1	3.69 ± 0.94	3.69 ± 1.02	2.14 ± 0.69	2.02 ± 0.40	×	×
10ml-2	3.83 ± 1.00	3.83 ± 1.07	2.33 ± 0.65	2.21 ± 0.44	×	×

Table 5–4: Mean±std distance in mm between the 10 landmarks after US-to-MR non-linear registration. Ultrasound volumes (source) are listed vertically and MR volumes (target) horizontally.

	0ml-1	0ml-2	5ml-1	5ml-2	10ml-1	10ml-2
0ml-1	×	×	1.07 ± 0.53	1.46 ± 0.65	1.50 ± 0.78	2.04 ± 0.92
0ml-2	×	×	1.26 ± 0.51	1.23 ± 0.68	1.70 ± 0.98	1.85 ± 1.23
5ml-1	0.92 ± 0.47	0.91 ± 0.39	×	×	1.39 ± 0.36	1.72 ± 0.56
5ml-2	1.32 ± 0.62	0.90 ± 0.50	×	×	1.51 ± 0.38	1.53 ± 0.63
10ml-1	2.11 ± 0.92	2.08 ± 0.80	1.98 ± 1.02	1.38 ± 0.45	×	×
10ml-2	2.69 ± 0.76	2.49 ± 0.89	1.74 ± 0.57	1.61 ± 0.50	×	×

Table 5–5: Mean±std distance in mm between the 10 landmarks after MR-to-MR non-linear registration

	0ml-1	0ml-2	5ml-1	5ml-2	10ml-1	10ml-2
0ml-1	×	×	0.63 ± 0.36	0.87 ± 0.47	1.08 ± 0.63	1.35 ± 0.54
0ml-2	×	×	0.77 ± 0.51	0.73 ± 0.36	1.17 ± 0.64	1.50 ± 0.62
5ml-1	0.73 ± 0.42	0.75 ± 0.25	×	×	0.94 ± 0.43	0.95 ± 0.45
5ml-2	0.90 ± 0.40	0.82 ± 0.55	×	×	0.87 ± 0.56	1.17 ± 0.47
10ml-1	1.33 ± 0.82	1.43 ± 0.96	1.19 ± 0.54	1.00 ± 0.34	×	×
10ml-2	1.63 ± 0.89	1.59 ± 0.86	1.04 ± 0.58	1.21 ± 0.49	×	×

5.5 Discussion

In this paper, we have presented a new method for correction of brain shift based on blood vessel segmentation and registration. The technique has been tested in a series of simulation experiments, and in a phantom study. It has shown to be able to recover large portions of linear and non-linear deformations even when only a very limited region of the MR image is covered by the US acquisition.

For the simulation experiments presented here, the technique was capable of recovering on average 75% of the deformations within the ROI with only 2% of the brain volume used to estimate the transformation. Because the ground truth was known in these experiments, there was no observer error associated with the identification of landmarks. Three of the registrations showed no improvement with non-linear registration. By visual inspection of the registration results, the alignment of the vessel trees improved, but this change was too small to influence the RMS or the landmarks.

The registrations presented in this paper can all be performed in less than 30 seconds on a 1.7 GHz PC. Linear and non-linear registration of the vessels can therefore be achieved in less than a minute. Non-linear resampling of entire image volumes might take more time. The computation speed is an important feature for intraoperative use, and will make it possible to efficiently correct preoperative data several times during a neurosurgical procedure. For the segmentation techniques, the most time consuming MR vessel segmentation can be computed pre-operatively and therefore does not add to the computation time required during surgery. The ultrasound vessel segmentation is only a simple thresholding, and the center line extraction can also be performed within less than

30 seconds which makes it possible to produce corrected anatomical and angiographic MR images in 1-2 minutes.

For the phantom study, it proved to be difficult to obtain a reliable segmentation of the smallest tubes from the MR images, especially the tubes on the surface of the phantom. This could probably be solved with higher resolution image acquisition, and if necessary a MR contrast agent in the tubes instead of water. However, this problem will not arise in real data sets were the blood vessels appear bright on a dark background (MRA, CTA) or dark on a bright background (PD) with no contrast between the vessel wall and the surrounding brain tissue.

Missing ultrasound data in highly deformed regions, in particular the tubes on the top of the phantom surface limited the accuracy of the registration. The ultrasound acquisition therefore has to be optimized for registration purposes, in order to target vessels in highly deformed regions. Despite these difficulities, the US-to-MR registration was able to recover the deformations to within an average of 1.6 mm compared to an average of 1.07 mm for the MR-to-MR registration. We consider the MR-to-MR registration the best possible result for this technique, and it shows an accuracy comparable to the resolution of the original data and the observer error in point identification.

These results demonstrate that ultrasound imaging in general and Doppler ultrasound in particular can be very useful modalities in detection and correction of brain-shift occurring during neurosurgical operations if the ultrasound acquisition is carefully performed in the highly deformed regions and optimized in order to capture vessels that are well represented in the preoperative MRA data. Better segmentation techniques for

MRA data that include segmentation of smaller vessels and in particular vessels on the cortical surface will increase the accuracy of the image registration.

Even though numerical simulations and physical phantoms are useful to test validate a registration technique, these approximations cannot fully simulate the complexity of the human brain. The registration technique will therefore be applied to a series of clinical data in the near future. The application of the technique to real data will enable us test the technique on data with anatomical variability, different magnitudes and directions of brain-shift, and different ultrasound volume coverage. This application will also enable us to make further improvements to the navigation software and the registration algorithm. Classification of vessel segments and branching points in order to further reduce the number of incorrect pairings and take into account vessel directions are possible improvements to the existing algorithm.

5.6 Conclusions

In this study, we have designed and validated a method to detect and correct brain-shift using image registration of blood vessels segmented from MR images and Doppler ultrasound data. The ultrasound based registration was compared to results obtained using MR-to-MR registration, and the results are comparable taking into account the difference in volume coverage. While more experiments are required to test the method with real patient data, these experiments show that blood vessels have the potential of being very useful features for registration of MR and US images. By using segmented blood vessels, we overcome many of the difficulties associated with registration of US data, providing the neurosurgeon with a fast tool to obtain accurate information about the anatomy and vasculature at any point in time during a surgical procedure.

5.7 Acknowledgements

We are grateful to Sylvain Bouix for providing his code for the centerline extraction algorithm.

Chapter 6

Clinical Validation of Vessel-based registration

Foreword

Having tested and validated the registration algorithm using numerical simulations and phantom data, the next step in this process was to apply the technique to retrospective clinical data. This study would determine the performance of our method in the presence of the full complexity of both the anatomy and the deformations. In the absence of a gold standard, the main challenge in this study was to quantitatively measure the accuracy of the recovered transformations. We implemented a series of several measures, each having their advantages and limitations, in order to characterize the registration results. The method was applied to five data-sets from patients having undergone neurosurgical procedures.

Clinical Validation of Vessel based Registration

I. Reinertsen[1] , F. Lindseth[2 5] , G. Unsgaard[3 4 5] and D. L. Collins[1]

[1] Montreal Neurological Institute (MNI), McGill University, Montréal, Canada

[2] SINTEF Health Research, Trondheim, Norway

[3] Department of Neurosurgery, St. Olav University Hospital, Trondheim, Norway

[4] The Norwegian University of Science and Technology, Trondheim, Norway

[5] National Center for 3D ultrasound in Surgery,

St. Olav University Hospital, Trondheim, Norway

To be submitted to *Medical Image Analysis*, November 2006.

6.1 Abstract

In this paper, we have tested and validated a vessel based registration technique for correction of brain-shift using retrospective clinical data from five patients. The algorithm uses vessel centerlines extracted from segmented pre-operative MRA data and intra-operative power Doppler ultrasound images to compute first a linear fit and then a thin-plate spline transform in order to achieve non-linear registration. The method was validated using (i) homologous landmarks identified in the original data, (ii) selected vessels, excluded from the fitting procedure and and (iii) manually segmented, non-vascular structures. The tracking of homologous landmarks shows that we are able to correct the deformation to within 1.25 mm, and the validation using excluded vessels and anatomical structures shows an accuracy close to 1 mm. Pre-processing of the data can be completed in 30 seconds per dataset, and registrations can be performed in less than 30 seconds. This makes the technique well suited for intra-operative use.

6.2 Introduction

Brain tissue displacement and deformation during neurosurgical procedures are major sources of error in neuro-navigation systems. While most hospitals rely only on the neurosurgeon's anatomical knowledge and experience in order to account for such deformations, solutions based on intra-operative measurements of the brain's position are becoming available. These techniques include deformable models and intra-operative imaging.

Deformable models [56, 47, 48] are computed from pre-operative images and depend on a series of assumptions about the mechanical properties of brain tissue as well as the magnitude and direction of brain deformations. The model can be updated using intra-operative measurements of the exposed cortical surface, for example.

The most commonly used modalities for three dimensional intra-operative imaging are computer tomography (CT), magnetic resonance imaging (MRI) and ultrasound imaging (US). CT imaging is associated with radiation dose exposure. For repeated acquisitions during surgery, this poses concern for both the patient and the medical staff. In addition, CT imaging suffer from poor soft tissue contrast and is therefore rarely used for neurosurgical planning and navigation [61, 62].

Compared to other intra-operative imaging modalities, intra-operative MR imaging can provide high quality images several times during a procedure, and can therefore be a valuable tool for detection, characterization and correction of brain-shift [55, 64, 65, 66, 67]. The data can be used for direct navigation, and for image processing purposes such as image registration to update pre-operative functional data or update a deformable model of the brain. Despite the ability to acquire high-quality images in a reasonable

time, this modality suffers from some important disadvantages. These include lower image quality when compared to pre-operative data and high cost due to the scanner itself, the need for MR compatible surgical equipment and major modifications of the operating room [68, 69]. These investments can only be justified for a limited number of hospitals.

Intra-operative ultrasound imaging does not suffer from many of the limitations associated with intra-operative MRI. This modality has therefore become increasingly popular for use in conjunction with pre-operative images in neuro-navigation systems, and for detecting and correcting brain-shift. Ultrasound data can be used directly for navigation purposes [14], or for image registration if the surgeon prefers to use pre-operative MRI data for navigation. Image registration makes it possible to update not only anatomical images for navigation but also other pre-operative datasets such as functional data and diffusion tensor images (DTI). Registration techniques presented in the literature include identification of homologous landmarks and intensity matching [18, 71, 52, 50, 51]. Registration of pre-operative MR with intra-operative US is a challenging registration problem due to different underlying physical principles and thus different image characteristics. Image intensities, noise characteristics, contrast, volume coverage and acquisition time are only a few main differences between a typical pre-operative MR image and a corresponding intra-operative ultrasound acquisition.

In an attempt to overcome some of these difficulties, we have explored a different approach to this particular registration problem. We use homologous features segmented from pre-operative and intra-operative data as "landmarks" to drive the registration. Such features might be any structures present in both datasets such as organ surfaces, cavities

or tissue interfaces. In this paper we investigate the use of vascular structures in the brain segmented from pre-operative MR angiography (MRA) and intra-operative power Doppler ultrasound imaging (USA). Blood vessels are relatively easy to segment from angiographic images and are distributed all over the cerebral cortex and inside the brain. They will therefore in almost all cases be present in any region of interest (ROI). Several groups have already investigated the use of blood vessels for various registration purposes. Applications of these registration techniques include forearm, liver, prostate and brain surgery[73, 74, 75, 77, 78, 79].

The focus of this paper is the validation of a vessel based registration technique for correction of brain-shift using clinical datasets. The registration algorithm has already been presented in detail elsewhere [3] with thorough validation using numerical simulations and phantom data. In this paper our main contribution is to validate the approach using retrospective patient data presenting the full anatomical complexity in addition to a range of different deformations in different parts of the brain. This study also makes it possible to test the registration method with typical clinical datasets, and not only images specially acquired for research purposes.

The paper is divided into seven sections. In the section following this introduction, the patient data are presented. The pre-processing of the data and the registration algorithm are presented in section 6.4, and the validation techniques used are all described in section 6.5. In section 6.6, the registration experiments and results are presented. Finally, a discussion of the results along with some remaining issues and final remarks are given in sections 6.7 and 6.8.

6.3 Patients and Data

In this study we have used data from five patients who have undergone surgery at St. Olav University Hospital, Trondheim, Norway. The data were taken from an anonymized database with permission from SINTEF Health Research and St. Olav University Hospital. All patients were scanned using MRI prior to surgery and intra-operative ultrasound was acquired during the operations for navigation, monitoring of vessels and the progress of the procedure as well as resection control. The patient data is presented in Table 6–1.

Patient	Lesion type	Location	Data
1	Media aneurysm	Left	MRA and 2 USA
2	AVM	Left temporal lobe	MRA and 2 USA
3	Anaplastic glioma showing transition to glioblastoma	Left parietal lobe	T2, MRA, B-mode and 2 USA
4	Anaplastic astrocytoma	Left frontal lobe	T1, MRA, B-mode and 2 USA
5	Metastsis from colon cancer	Right frontal and parietal lobe	T1, MRA, B-mode and 2 USA

Table 6–1: Patient data. AVM: arteriovenous malformation, USA: ultrasound angiography (Doppler ultrasound imaging), B-mode: ultrasound tissue imaging, T1: T1 weighted MR imaging, T2: T2 weighted MR imaging.

6.3.1 Pre-operative MR acquisitions

MR data of the patients included in this study (see Table 6–1) was generally acquired the day before surgery. Prior to scanning, skin fiducials were glued onto the patient's head. For the vascular cases (patients 1 and 2) the MRA volumes ($240\times320\times151$ voxels with a voxel size of 0.68×0.68 mm^2 in plane and a slice thickness of 1 mm) were acquired in a Picker 1.5T scanner (Picker International, Inc., Cleveland, OH). For the tumor cases

(patients 3-5), both anatomical and angiographic MR data were acquired in a Philips Intera 3T scanner (Philips Medical Systems, Best, the Netherlands) giving anatomical MR volumes with 256×256×180 voxels and 1 mm isotropic resolution, as well as MRA volumes with 512×512×245 voxels and a voxel size of 0.39×0.39×0.5 mm^3.
Prior to surgery, the available MR data was imported into the ultrasound-based neuronavigation system SonoWand (MISON A/S, Trondheim, Norway) [14] and registered to the patient using a fiducial-based corresponding point technique. The registration accuracy was then verified to be acceptable (within 2 mm) and conventional pre-surgical planning based on available pre-operative MR data was performed.

6.3.2 Intra-operative ultrasound acquisitions

After the craniotomy, but before opening the dura, one or more ultrasound acquisitions were performed (only USA for the vascular cases, and both B-mode and USA for the tumor cases). A pre-calibrated [22] optically tracked 4-8 MHz Flat Phased Array (FPA) ultrasound probe with optimal focusing properties at 3-6 cm was tilted and/or translated by free hand movement over the anatomical area of interest. The 2D images were reconstructed into pyramid-shaped 3D data sets, and were then digitally transferred to the navigation computer and reconstructed into a regular 3D volume using the original 1D scan line data (unpublished method by SINTEF). The time required to perform the freehand scan, transfer the images and reconstruct the volume was between 30 and 60 seconds depending on the resolution of the final ultrasound volume (with a common volume consisting of 300×300×300 voxels with an isotropic voxelsize of 0.35 mm taking about 45 seconds). Additional 3D B-mode and power Doppler data were acquired when needed during the operation to update the image map for brain-shift or perform

resection control near the end of the operation. The clinical navigation accuracy of the neuronavigation system used has previously been estimated to be below 2 mm when navigation is based on a recently acquired ultrasound volume [6].

6.3.3 Data export

Postoperatively, both pre- and intra-operatively acquired image data could be exported with the same spatial mismatch (shift) as experienced during surgery. Any volume could be chosen as master and the other volumes were resliced according to the master volume (i.e. all exported volumes were equal in terms of number of voxels and voxel size, typically $300\times300\times300$ voxels with an isotropic voxel size of 0.4 mm for the spatial region where both MR and ultrasound data existed). This made it possible to evaluate the vessel-based registration method for brain-shift correction presented in this paper using real clinical patient data.

6.4 Registration method

6.4.1 Vessel segmentation and centerline extraction

High quality images from both MRA and USA can be segmented by simple thresholding or by more sophisticated techniques based on shape and intensity information [72].
In this study, both MRA and USA data were segmented by simple thresholding of the voxel intensities. In order to increase the signal-to-noise ratio and thereby facilitate segmentation by thresholding, the USA data were blurred with a Gaussian kernel with a full width at half maximum (FWHM) of 1 mm. The size of the blurring kernel was chosen to optimize the performance of the centerline extraction algorithm. Following segmentation, vessel centerlines were extracted using a fast, robust and automatic method based on medial surfaces. The technique uses the average outward flux of the

gradient vector field of the distance transform of the object to compute the medial surface [93]. The centered medial curves are then obtained by topology preserving thinning ordered by the distance function to the object's boundary. This ensures that the remaining points lie on the medial surface and as far away from the vessel boundary as possible. The medial curve was finally pruned based on length to remove superfluous branches and obtain a single curve for each vessel branch. Details of the method can be found in [94]. An example of the different pre-processing steps is shown in Figure 6–1.

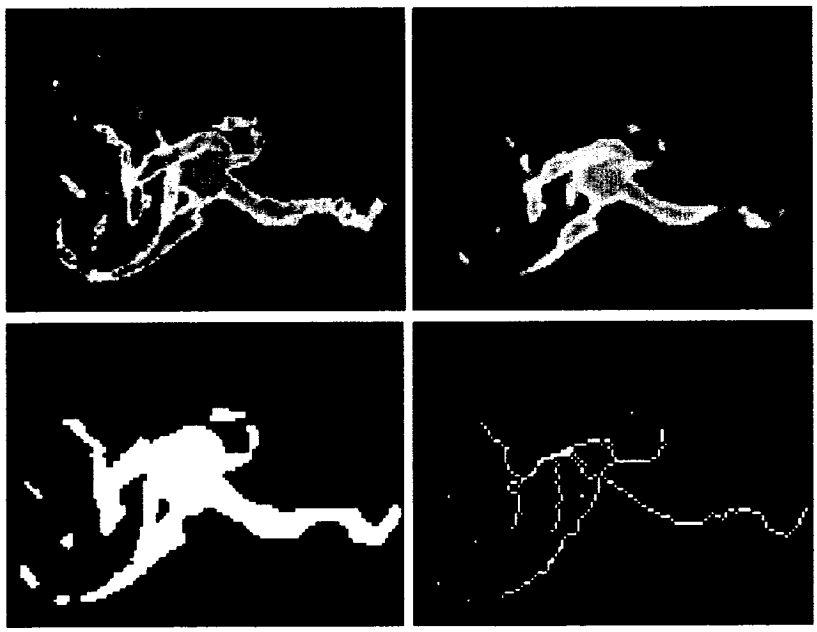

Figure 6–1: Pre-processing of an ultrasound image of an aneurysm acquired from the dura. Top left: Maximum intensity projection (MIP) of the original volume. Top right: MIP of the blurred volume. Bottom left: MIP of segmented volume. Bottom right: MIP of extracted centerlines.

6.4.2 Registration algorithm

After segmentation and centerline extraction, the MRA and USA volumes are binary images representing the vascular tree. The vessels are in the form of a "skeleton" representing the midlines. The two datasets are only partially overlapping, and vessels are not necessarily continuous. A number of vessels might also be missing from one or both data sets. The alignment of the two datasets is done in two steps: (1) a linear registration with six parameters (rigid body), and then (2) a non-linear registration to account for deformations. For both linear and non-linear registration we use modified versions of the iterative closest point algorithm (ICP) [95]. The method can be summarized as follows:

1. Point matching: Each point in the source dataset is paired to the closest point in the target dataset. The dataset with fewest points will serve as the source dataset and the other as target dataset. If necessary, the source dataset can be sub-sampled prior to point matching.
2. Weighting/Rejecting point pairs: The point matching process tends to produce a large number of incorrect pairings. In order to reduce the influence of such wrong pairings on the registration result, we use the least trimmed squares (LTS) [112] robust estimator. The LTS technique uses only a given percentage of the available points for the least squares estimation. These points are selected based on the distance to the closest point in the target dataset, and a given percentage of the points corresponding to the largest distances are rejected from the least squares estimation. This technique makes it possible to exclude a large number of outliers from the registration process. The percentage of points rejected from the

registration should be selected based on the amount of noise and missing vessels in the data, and has to be selected for each registration.

3. Estimating the transformation: The transformation (linear or non-linear) is computed using the remaining point pairs. For linear registration we use a six parameter least-squares transform, and for non-linear registration we use a thin-plate spline transform [113]. The thin-plate spline transform can be scaled used a parameter σ.
4. Applying transformation to the source points: The estimated transformation is then applied to the entire source dataset.
5. Calculating the error: We compute the mean distance between the source points and the closest point in the target dataset. In the case of linear registration, these five steps are iterated until the difference in mean distance between successive iterations is smaller than 0.0001 mm. Because the thin-plate spline transform gives an exact fit, only one iteration is needed for the non-linear registration.

For more details on the algorithm, see [3].

6.5 Validation methods

The validation of a registration technique should include several experiments carefully designed to investigate the behavior of the algorithm in the presence of a range of different deformations, complex anatomies as well as different image qualities. The first part of the validation process could be simulated deformations using a dataset from a patient or a normal volunteer. This experiment makes it possible to compare the recovered transformation with the known truth. One of the main limitations is that the simulated deformations are not necessarily representative of the range of deformations

present in real patient data. Another disadvantage is that only one image from one modality can be used and it is difficult to simulate the volume coverage and image quality of the other modality. In order to use both modalities in a more realistic setting, a phantom study can be performed. In this situation the true deformation remains unknown, but both anatomy and deformations can be closely controlled and kept simpler than those in the human brain. Both these studies have been performed using the registration algorithm described above, and are presented in [3]. The next step in the validation process is to test the algorithm using real patient data. These datasets represent the full anatomical complexity of the human brain in addition to a range of different deformations. The data used are typical clinical datasets acquired for diagnosis, surgical planning, neuro-navigation, resection control and monitoring during the procedure. The main challenge in this situation is that the true displacement remains unknown. We have therefore designed a series of experiments to investigate the performance and the behavior of the method using real data. As described below, they all have some advantages and some limitations. However, seen together, they give a good idea of the performance of the registration technique in the different surgical cases.

6.5.1 Identification of landmarks - Intra-rater variability

As mentioned above, the true displacement and deformation between the pre-operative and intra-operative data remains unknown. It was therefore necessary to establish a "gold standard" in order to evaluate the performance of the registration algorithm. This "gold standard" was defined by the identification of ten homologous anatomical landmarks in each angiographic dataset. Because they were identified in angiographic images, the landmarks were mainly vessel branching points and points with high curvature. It is

important to note, however, that the identification was performed in the original data and was therefore independent of the vessel segmentation.

Images from patients 3 and 4 were then used to evaluate the intra-rater variability in landmark identification. Vessel patterns such as branching points and high curvature points were identified, described and drawn on paper. The descriptions and drawings were then used to recognize the selected landmarks without the use of previously identified points. In total, ten points were identified in each dataset once every day for four consecutive days resulting in 40 points for each dataset. Points were identified in the MRA and the two USA exams for each patient.

6.5.2 Robustness and Capture range

The first validation experiment was performed in order to investigate the robustness, convergence properties and capture range of the linear registration. A "gold standard" was defined using the previously identified landmarks in one MRA and one USA acquired from the dura. The algorithm was then run from 20 different virtual starting positions relative to this "gold standard", and the registration result was compared to the "gold standard" after each iteration.

Brain-shift of up to 50 mm is reported in the literature [57]. It was therefore important to ensure that the algorithm was able to register data from a wide range of starting positions without getting trapped in local minima of the objective function, resulting in mis-registrations. This experiment was also important in order to evaluate the number of iterations required to reach convergence and the processing time needed for the linear registration.

6.5.3 Tracking of homologous landmarks

Again, a "gold standard" was established for each pair of images to be registered, and the registration algorithm was run with real patient data as input. The distance between corresponding landmarks in the source and target voulmes before and after registration was used as a measure of the registration performance.

In order to establish a lower bound for the linear registration, we performed a rigid body least-squares fit using the landmarks identified in the source and target volume, and computed the distance between the source and target landmarks following this transformation.

The main limitation with this validation technique is that we are tracking points that are localized on blood vessels. We are therefore tracking the distance between vessels, a measure that is biased toward our vessel-based registration technique. In addition, the registration result is only evaluated at ten points and not throughout the entire volume. In regions with few or no vessels, or close to the edges of the volume, for example, the registration result might be different from the result reflected by the landmarks.

6.5.4 Vessel exclusion

The next validation measure was also based on distance between vessels. For each of the patients we eliminated one or two segmented vessels from the source dataset. The linear and non-linear registrations were then performed using the remaining vessels. Following registration, the recovered transformations were applied to the excluded vessels, and the distance to the corresponding vessel in the target dataset was measured after each registration step. As mentioned earlier, this measure is also based on distances between vessels and is therefore somewhat biased. The result obviously also depends on

the vessels selected for distance measurements. However, the selected vessels did not participate in the registration process and are therefore useful for testing.

6.5.5 Segmentation of anatomical structures

It was only possible to perform this last experiment for patients 3-5 where both anatomical MRI (T1 or T2 weighted and Gd-enhanced T1 images) and B-mode images were available. Anatomical structures were manually segmented from anatomical MRI and B-mode images and distances were measured before registration, after linear registration and after non-linear registration. The advantage of this approach is that the data used for distance measurements are completely independent of the data used for registration. The structures segmented are also all non-vascular and make it possible to measure the performance of the algorithm in regions between vessels. This measure also gives an idea of how well brain deformations are captured by the vascular tree and how far away from a vessel we are able to correct deformations. A limitation with this method is that the results are dependent on the manual segmentations. Reliable and reproducible segmentations of B-mode images in particular can be very challenging. Another limitation is that the USA data used for registration and the B-mode data used for validation were not acquired simultaneously. For the data used in this study, there was a maximum delay of 5 minutes between the two acquisitions. Brain tissue can obviously move and deform during this period. However, visual inspection of the datasets shows good correspondence and no noticeable deformation.

6.6 Experiments and Results

6.6.1 Identification of landmarks - Intra-rater variability

As described in section 6.5.1, the intra-rater variability in landmark identification was assessed by identifying the ten points in six datasets four times each. The mean distances between the identified points in each of the datasets along with the corresponding standard deviation are presented in Table 6–2.

Patient	MRA	USA1	USA2
3	0.74±0.77	0.86±0.78	0.99±0.67
4	0.91±0.44	0.84±0.55	1.09±0.87

Table 6–2: Mean distance ± standard deviation between the identified points in each of the six datasets. All measurements in mm.

6.6.2 Robustness and Capture range

In order to assess the robustness and capture range of the linear registration results we assumed that the transformation defined by the least squares fit between the landmarks identified in patient 3, represented the gold standard. The algorithm was then run from 20 different starting positions. The starting positions were uniformly distributed in the range of +/- 10 mm for each of the three translational parameters and in the range of +/- 10 degrees for each of the three Euler angles away from the assumed correct position. The mean distance between all source points and the corresponding closest points in the target volume was recorded after each iteration. The iteration process was stopped when the difference in mean distance between two successive iterations was smaller than 0.0001 mm.

The difference in mean distance between the recovered transformation and the "gold standard" as a function of iteration number for each of the 20 starting positions is shown in Fig. 6–2.

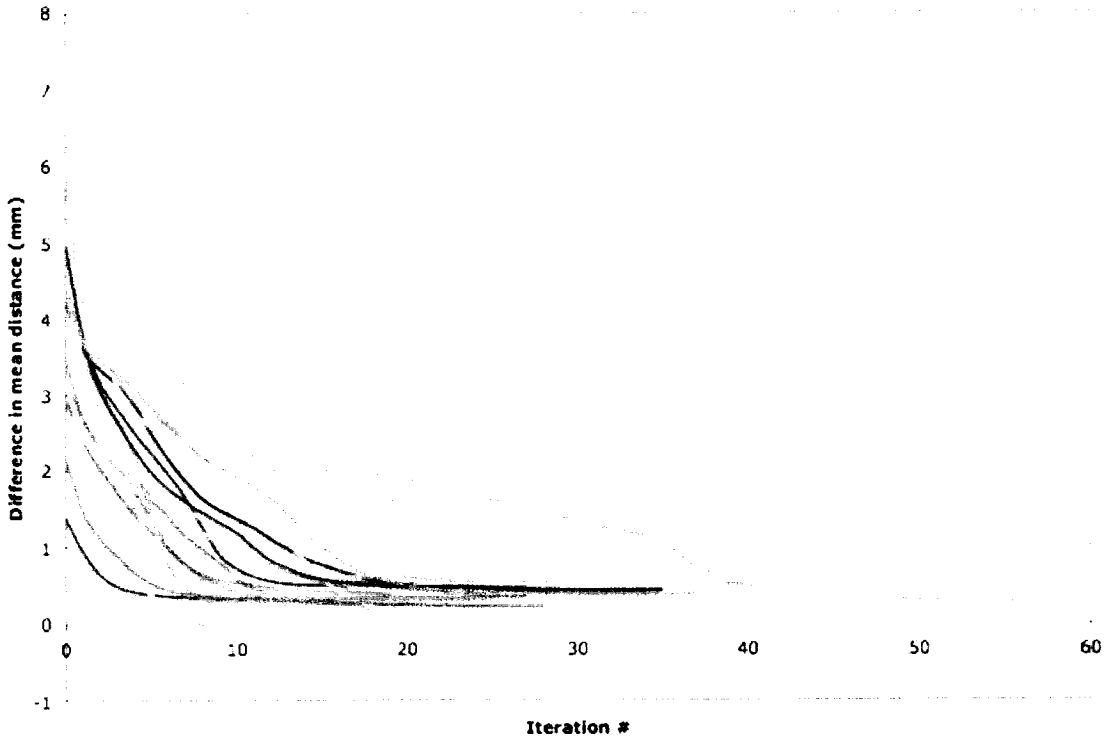

Figure 6–2: Difference in mean distance between the recovered transformation and the gold standard as a function of iteration number for each of the 20 starting positions

As shown in Figure 6–2, 19 of the 20 starting positions resulted in a correct registration as evaluated by visual inspection. In one case, the algorithm failed and the recovered transformation resulted in a mis-registration. Before registration, the difference in mean distance between the simulated transformation and the gold standard was 4.33 ± 1.44 mm. After registration, this distance was reduced to 0.33 ± 0.18 mm for the 19 successful

registrations. For the unsuccessful registration the difference was 3.03 mm. The mean computation time for these registrations was 20.3±6.5 seconds on a 1.67 GHz laptop PC.

6.6.3 Tracking of homologous landmarks

Following segmentation and centerline extraction, the data-sets were registered linearly and non-linearly using the algorithm described in section 5.3.4. The necessary preprocessing of the data took close to 30 seconds per dataset on a 1.67 GHz laptop PC. Three series of registrations were then performed. First, the pre-operative MRA images were registered to the USA images recorded from the dura, then the USA data from the dura were registered to the USA acquired during the operation, and finally the pre-operative MRA images were registered to the USA acquired during the operation. The optimization parameters (sub-sampling of source dataset, the percentage of points used in the LTS estimation and the scaling factor σ) were manually optimized for each registration. The second and third series of registration were only performed in patients 1, 3 and 4 because of insufficient quality of the second USA images and difficulty in identifying reliable landmarks.

For comparison and in order to establish a lower bound for the linear registration, we performed a rigid body least squares registration using the landmarks identified in the MRA and first USA volume, then using the landmarks from the first and second USA volumes and finally using landmarks from the MRA and the second USA volume.

As shown in Tables 6–3, 6–4 and 6–5, the distance between landmarks after linear registration was between 0.89 and 3.00 mm with a mean value of 1.58 mm, and between 0.67 and 2.22 mm with a mean value of 1.24 mm after non-linear registration. For comparison, the distance between landmarks after landmark-based rigid body registration

Patient	Distance before reg.	Landmark-based reg.	Distance after lin. reg.	Distance after non-lin. reg.
1	7.28±0.88	1.44±0.49	1.72±0.90	1.44±0.64
2	9.70±1.05	1.55±0.55	1.84±0.64	1.52±0.60
3	9.02±1.01	0.76±0.28	0.89±0.46	0.67±0.37
4	4.68±1.05	0.83±0.49	0.98±0.48	0.72±0.49
5	6.02±1.30	0.82±0.36	1.03±0.39	1.04±0.67

Table 6–3: Mean distance ± standard deviation in mm between 10 landmarks identified in USA from the dura and original MRA before and after registration.

was between 0.76 and 2.57 mm with a mean value of 1.38 mm. Extracted centerlines of the USA and MRA for one patient before and after registration are shown in Figure 6–3, and volume renderings of the vessels from the same patient before and after registration are shown in Figure 6–4.

Patient	Distance before reg.	Landmark-based reg.	Distance after lin. reg.	Distance after non-lin. reg.
1	3.25±1.41	2.03±1.06	2.36±0.86	1.86±0.94
3	2.00±0.84	1.27±0.77	1.29±0.81	0.86±0.53
4	3.97±0.91	1.12±0.36	1.16±0.38	1.14±0.60

Table 6–4: Mean distance ± standard deviation in mm between 10 landmarks in USA from dura and second USA before and after registration.

Patient	Distance before reg.	Landmark-based reg.	Distance after lin. reg.	Distance after non-lin. reg.
1	6.83±1.00	2.57±1.56	3.00±1.42	2.22±1.18
3	8.25±1.17	1.29±0.45	1.43±0.40	1.03±0.38
4	7.58±1.20	1.49±0.46	1.67±0.44	1.10±0.59

Table 6–5: Mean distance ± standard deviation in mm between 10 landmarks in second USA and MRA before and after registration.

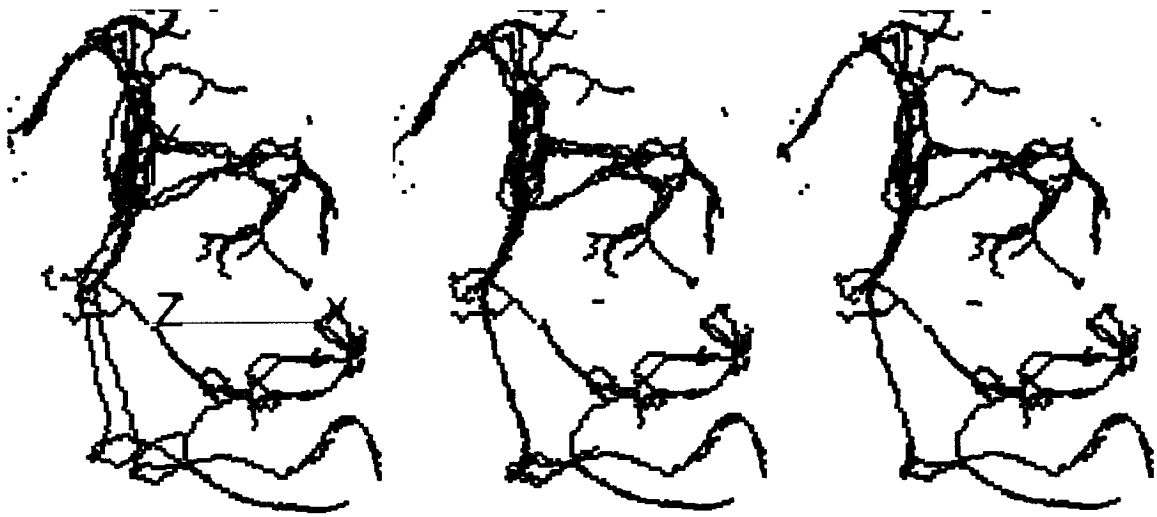

Figure 6–3: Centerlines extracted from vessels segmented from data-set 3 before registration (left), after linear registration (middle) and after non-linear registration (right). MRA in red and USA in blue.

6.6.4 Vessel exclusion

For this experiment, the segmented vessels from pre-operative MRA and intra-operative USA from the dura were used. One or two segmented vessels were manually selected and removed from each of the source data-sets. The linear and non-linear registrations

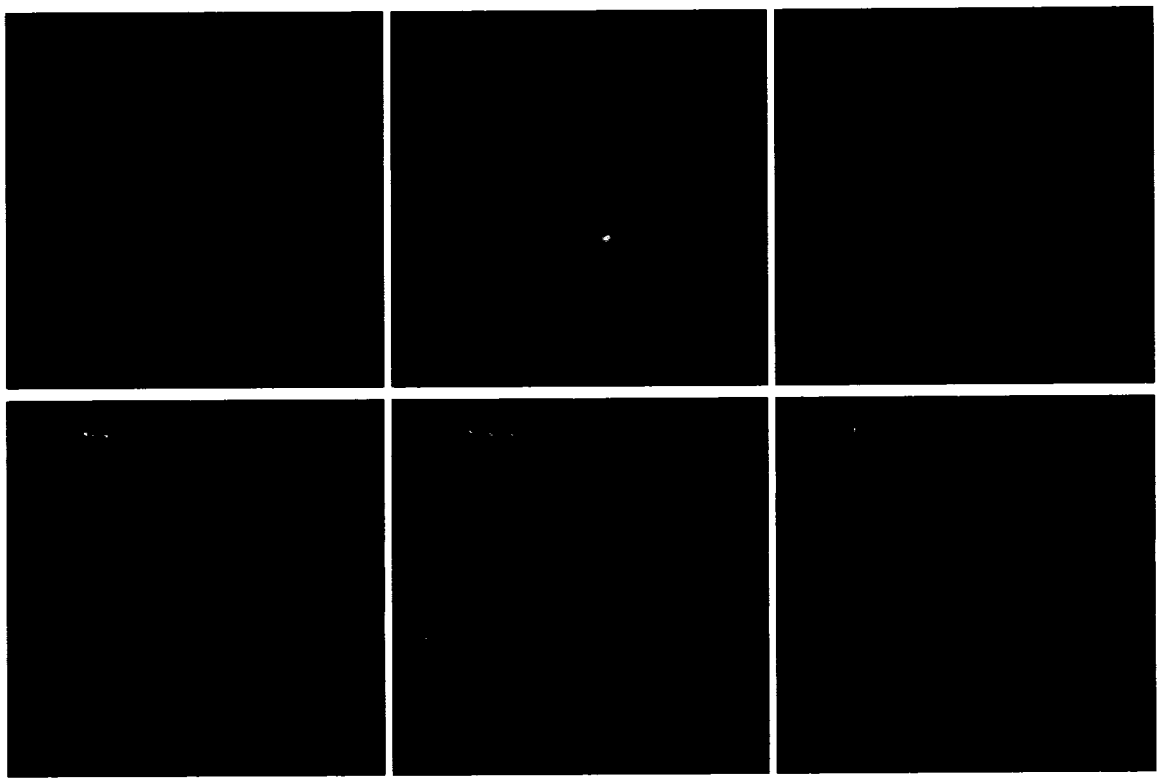

Figure 6–4: Patient 3: Volume renderings of the USA (grey) and MRA volumes before registration (left column), after linear registration (middle column) and after non-linear registration (right column). MRA before registration is in red, MRA after linear registration is in yellow and MRA after non-linear registration is in green. The top row and bottom row show two different views of the same patient.

were then performed as described above. The landmarks previously identified (see section 6.5.1) in all datasets were used to select the optimization parameters (sampling, percentage of points used in LTS and scaling) in each case. In order to measure distances between the excluded vessels before and after registration, we used chamfer distance maps [117]. A distance map of the vessel selected from the source data-set was computed and multiplied with the vessel selected from the target data-set. We then computed the distance map for the target vessel and multiplied it with the source vessel. The mean

and standard deviation of the resulting distances in the two images were recorded. In cases where one vessel was clearly longer than the other, a chamfer map was computed only for the longest vessel and multiplied with the shortest vessel. This was done in order to minimize the error due to different lengths. The recovered linear and non-linear transforms were applied to the source vessels and the measurements were repeated. The resulting distances are presented in Table 6–6. An example of extracted centerlines with vessels selected for exclusion is shown in Figure 6–5, and the two selected vessels before and after registration are shown in Figure 6–6.

Patient	Vessel	Distance before reg.	Distance after lin. reg.	Distance after non-lin. reg.
1	1	2.85±1.53	0.86±0.26	0.73±0.18
2	1	6.23±0.65	0.87±0.36	0.90±0.48
3	1	8.90±1.51	0.74±0.27	0.68±0.24
	2	6.34±0.54	0.70±0.38	0.66±0.38
4	1	1.86±0.38	0.79±0.39	0.73±0.45
	2	2.93±0.16	0.38±0.26	0.73±0.65
5	1	3.28±1.83	0.95±0.44	0.98±0.52

Table 6–6: Mean distance ± standard deviation in mm between excluded vessels before and after registration

6.6.5 Segmentation of anatomical structures

In order to test the behavior of the registration algorithm in regions between vessels we measured distances between structures segmented from anatomical images before and after registration. This validation could only be performed for patients 3-5 where both angiographic and anatomical data were available. For patient 3, a portion of the Sylvian fissure was segmented from pre-operative T2 data and intra-operative B-mode. For patient 4, a portion of the right lateral ventricle was segmented from pre-operative T1 data and intra-operative B-mode, and for patient 5 a part of the tumor was segmented

Figure 6–5: Centerlines extracted from vessels segmented from data-set 3 with vessels excluded from the registration process. MRA in red, USA in blue and selected vessels in green.

from pre-operative T1 and intra-operative B-mode. The contours of the selected structures were then extracted by dilating the original labels once and subtracting the original labels. Distances between contours before and after registration were then measured using chamfer distance maps as described in the previous section. An example of the tumor contour extracted from pre-operative MR data and the corresponding B-mode image before registration, after linear registration and after non-linear registration is shown in Figure 6–7, and the distance measures are presented in Table 6–7.

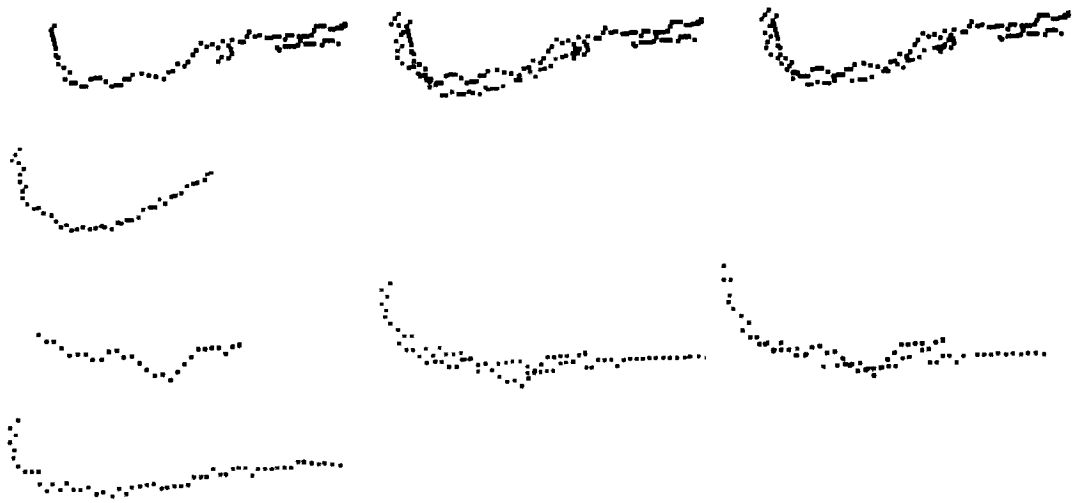

Figure 6–6: The excluded vessels from data-set 3 before registration (left), after linear registration (middle) and after non-linear registration (right). Vessel 1 (top row) and vessel 2 (bottom row). MRA in red and USA in blue.

Patient	Structure	Distance before reg.	Distance after lin. reg.	Distance after non-lin. reg.
3	Sulcus	6.99±2.93	0.91±0.69	0.71±0.66
4	Lateral ventricle	1.61±0.86	0.92±0.47	1.01±0.54
5	Tumor	2.11±1.18	0.85±0.56	0.79±0.51

Table 6–7: Mean distance ± standard deviation in mm between segmented structures in anatomical data.

6.7 Discussion

In this paper, we have tested and validated a vessel based registration technique for correction of brain-shift using clinical data-sets from five patients. By using three different validation methods, we have demonstrated that the technique is able to recover large portions of the displacements.

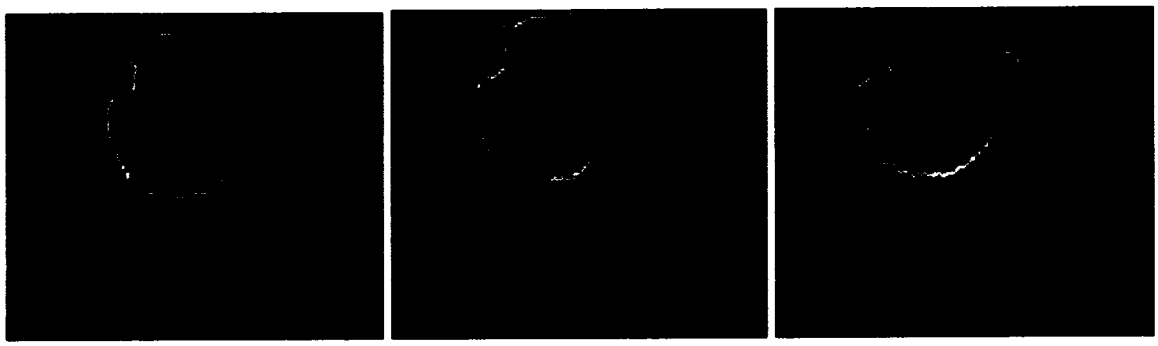

Figure 6–7: Patient 5: Contour of tumor segmented from pre-operative Gd-enhanced T1 data on top of intra-operative B-mode image before registration (left), after linear registration (middle) and after non-linear registration (right).

The intra-rater variability presented in section 6.6.1 show that the landmarking error is on the order of twice the voxel size in the data. It is also worth noting that the landmarking error in the two modalities is of the same order of magnitude.

The reproducibility results presented in section 6.5.2 show that in almost all cases, the algorithm converges to the correct solution in less than 30 seconds. The mean difference between the recovered transformations and the assumed "gold standard" is smaller than both the landmarking error and the resolution of the images which is 0.4 mm in all three directions. In the case where the algorithm failed, the parameters of the starting position were translations of 10, 4 and -10 mm in the x, y and z-direction respectively, and rotations of -7, -10 and 3 degrees for the three Euler angles. This position proved to be too far away for the algorithm to correctly register the data. Compared to the translations and rotations seen in the 5 patient datasets presented here, this starting position seems to represent an extreme case rarely seen in real data. If, however, the situation occurs in a clinical setting, it is possible to perform a preliminary manual registration in order to ensure a correct result.

The registration results presented show that the linear registration in general accounts for most of the displacement. The linear shift between pre-operative and intra-operative images is a combination of the error in the rigid registration performed prior to the craniotomy using anatomical landmarks on the patients head, and the linear component of the actual brain-shift occurring after the opening of the skull. Using landmarks identified in the original angiographic images, the distance after linear registration was between 0.89 and 3.00 mm with a mean value of 1.58 mm, and between 0.67 and 2.22 mm with a mean value of 1.24 mm after non-linear registration. All the images had an isotropic voxel size of 0.4 mm. The landmark-based registration represents the lower bound for the linear registration. For comparison, the distance between landmarks after landmark-based rigid body registration was between 0.76 and 2.57 mm with a mean value of 1.38 mm.

The non-linear registration using a thin-plate spline improved the registration slightly in most of the cases, but also made no change or made the distance slightly larger in some cases. In general, the thin-plate spline transform improves the registration in regions between or relatively close to the vessels. Close to the edges of the volume, for example, the thin-plate spline transform can possibly make the registration worse due to the lack of vessels and thus a lack of reliable landmarks to restrain the transform.

The experiment performed using excluded vessels and segmented anatomical structures shows that we are able to correct the deformation to within 1 mm.

In the experiments presented in this paper, the dataset with fewest points is always considered the source. Therefore, depending on the number of points in each data-set, the MRA or the USA may serve as the source. If the USA volume is the source,

the recovered transform has to be inverted and applied to the MRA. This approach is consistent with the original ICP algorithm proposed by Besl and McKay [95]. In some cases, however, matching the largest dataset to the smallest dataset gives a better result when tracking homologous landmarks. It is possible that the choice of source and target should depend not only on the number of available points but also on the "quality" of the points (fairly long continous vessel branches compared to short non continuous segements, for example). If this is the case, more experiments will be needed in order to determine which dataset should be considered the source in order to obtain the best possible result.

In principle, the registration technique can be used to correct brain-shift in all types of neurosurgical procedures. However, vascular cases (AVMs and aneurysms, for example) can be more challenging than tumor cases because the goal of the surgery is to eliminate vascular structures. Large portions of the vessels in the ROI present in the ultrasound acquisition made on the dura might be missing from subsequent acquisitions. In these cases it might be more difficult to perform registrations toward the end of the procedure. In our future work, we plan to further validate the registration algorithm by performing registrations in the operating room during surgery. In addition to visual inspection of the registration results, a possible validation experiment will be to identify points in the patient's brain using a computer tracked pointer and compare the locations with the corresponding points in the corrected MR images.

All the registrations presented in this paper were performed in less than 30 seconds, and the pre-prcessing was completed in close to 30 seconds per dataset on a 1.67 GHz laptop PC. This makes it possible to present updated images in the OR within reasonable

time limits. As the linear portion of the registration accounts for most of the shift, it is also possible to only perform linear alignment and thus avoid the slightly more time consuming non-linear resampling of the data.

6.8 Conclusions

In this study, we have validated a vessel based registration algorithm for correction of brain-shift using retrospective MR and ultrasound data from five patients who have undergone neurosurgery. The technique has been validated using three different measures, and has shown to be able to recover large portions of the brain displacements and deformations occurring during the neurosurgical procedure. The results presented in this paper show that blood vessels are useful features for registration of MR and US data and enable us to update pre-operative images with high accuracy in a short period of time.

6.9 Acknowledgements

We are grateful to Drs. Sylvain Bouix and Kaleem Siddiqi for providing the code for the centerline extraction algorithm.

Chapter 7

Discussion and Conclusions

7.1 Discussion

The purpose of this thesis was to develop and validate a vessel based registration method for correction of brain-shift. The method uses segmented blood vessels from pre-operative angiographic images and intra-operative Doppler ultrasound to drive the linear and non-linear registration.

Chapter 4 presented the design, construction and characterization of a deformable brain phantom. The phantom was built and the reproducibilty of the deformations were carefully characterized in order to serve as a gold standard in the validation of the registration technique. The experiments presented using surface measurements and MR imaging showed that the deformations were reproducible to within 1 mm. It was also demonstrated that the phantom was compatible with both MR and ultrasound imaging.

In Chapter 5 the registration algorithm was presented in detail and phantom data was used to validate the method. For comparison, both ultrasound based registration and MR

based registration were performed using the same deformations of the phantom. The ultrasound based registration showed an accuracy of 1.6 mm and the MR based registration showed and accuracy of close to 1 mm. In addition to the phantom experiment, a series of numerical simulations using an MRA volume from a normal volunteer was presented. These experiments showed that the registration algorithm was able to account for 75% of the deformations in the volume covered by both modalities.

Having validated the technique using both numerical simulations and phantom data, the next step in the validation process was to evaluate the method using retrospective clinical data. In Chapter 6, five patient data-sets were used for validation. Because the true displacement remained unknown, a series of validation experiments was designed and performed. These included tracking of homologous landmarks, exclusion of selected vessels and segmentation of non-vascular structures from anatomical data. Tracking of homologous landmarks resulted in a registration error of 1.24 mm while the experiments using excluded vessels and segmented anatomical structures showed an error close to 1 mm.

In this thesis, no measures of the diameter of the vessels used for registration were made using real patient data, but the phantom study suggested that it was possible to detect vessels with a diameter of 1.6 mm. The validation using clinical data suggest that the Doppler ultrasound is more sensitive to small vessels than MRA. High quality MRA data is therefore important for successful registration of small vessels.

As mentioned in the introduction to this thesis, intensity-based registration of ultrasound and MR data is challenging due to different image characteristics. By using automatically extracted features such as blood vessels, many of the difficulties associated with

this particular registration task can be overcome. The registration using blood vessels makes it possible to present updated pre-operative data several times during the operation and will therefore increase the usefulness of all available pre-operative datasets. Compared to other methods for correction of brain-shift, the vessel-based technique presented in this thesis has some important advantages. The experiments show that it is possible to achieve an accuracy between 1 and 1.6 mm which is comparable to results presented in the literature using deformable models [48] or registration of intra-operative MRI [66, 67], which is often considered to be the gold standard in detection and correction of brain-shift. The solution proposed in this thesis is less complex, less time consuming and several times less expensive than iMRI.

7.2 Future work

The registration technique presented in this thesis can be further improved and validated in several ways. The registration results are dependent on the accurate segmentation of blood vessel from both ultrasound and MRA data. Consequently, the registration will benefit from both improvements in image quality and segmentation and centerline extraction algorithms. In particular, little work has been published on segmentation of ultrasound data. For both the linear and non-linear registration, the choice of source and target in order to obtain the best possible registration result remains an open issue. Further experiments will be necessary in order to determine the characteristics of the data-sets and their influence on the registration result. Further possible improvements of the algorithm include the use of approximating thin-plate splines [116] or possibly other types of splines. By using approximating splines, it will be possible to perform more than one iteration for the non-linear registration and possibly improve registration

results. Another possibility is to extrapolate the displacement outside the volume covered by the ultrasound images. This will require the use of anchor points for the non-linear registration defined on the skull, for example. Structures other than blood vessels could also be incorporated in order to improve the accuracy of the technique. Such structures could be tumor boundaries, ventricles or sulci, for example. This would be particularly useful if the structures could be automatically or semi-automatically extracted from ultrasound data.

The next step in the validation of this technique would be to perform registrations during surgery, and eventually incorporate the registration software into a neuronavigation system. Testing in a real clinical setting makes it possible to measure the real diameter of vessels used for registration, and give further indication of areas that will need improvement and optimization, .

An important validation experiment would also be the comparison between ultrasound based registration and intra-operative MR using real patient data. Intra-operative MR is the imaging modality giving the highest quality intra-operative images and would represent the best possible "gold standard" for this type of registration experiments. In this thesis, correction of anatomical data has been shown. A further extension of this work would be to correct functional data such as fMRI, PET and diffusion tensor images (DTI) used for surgical planning.

7.3 Conclusions

The goal of this thesis was to present the development and validation of a vessel based registration technique based on pre-operative angiographic data and intra-operative Doppler ultrasound images. The experiments and results presented show that the

technique can correct brain displacements and deformations with high accuracy in a very reasonable time. The method is therefore well suited for intra-operative use. The studies presented in this thesis also show that blood vessels are useful features for image registration and that they in general capture the deformation of the surrounding tissue. By using blood vessels for registration purposes, it was possible to overcome many of the difficulties associated with MR-to-US registration, and this approach will provide the surgeon with updated information about the vasculature, as well as anatomy during surgical procedures

References

[1] I. Reinertsen and D. L. Collins, A Realistic Phantom for Brain-shift Simulations, Medical Physics, 33(9), p. 3234-3240, 2006.

[2] I. Reinertsen, M. Descoteaux, K. Siddiqi and D. L. Collins, Validation of Vessel-based Registration for Correction of Brain-shift, Accepted for publication, Medical Image Analysis, June 2006.

[3] I. Reinertsen, F. Lindseth and D. L. Collins, Clinical Validation of Vessel based Registration, To be submitted to Medical Image Analysis, October 2006.

[4] N. E. Leeds and S. A. Kieffer, Evolution of diagnostic Neuroradiology from 1904 to 1999, Radiology, 217, p. 309-318, 2000.

[5] T. M. Peters, Image-guidance for surgical procedures, Physics in Medicine and Biology, 51, p. 505-540, 2006.

[6] F. Lindseth, T. Langø, J. Bang and T. A. Nagelhus Hernes, Accuracy evaluation of a 3D ultrasound-based neuronavigation system. Computer Aided Surgery, 7(4), p. 197-222, 2002.

[7] F. Lindseth, J. Bang and T. Langø, A robust and automatic method for evaluating accuracy in 3-D ultrasound-based navigation, Ultrasound in Medicine and Biology, 29(10), p. 1439-1452, 2003.

[8] E. Samset, Hirschberg H. Neuronavigation in intraoperative MRI, Computer Aided Surgery, 4(4), p. 200-207, 1999.

[9] S. Poggi, S. Pallotta, S. Russo, P. Gallina, A. torresin and M. Bucciolini, Neuronavigation accuracy dependence on CT and MR imaging parameters: a phantom-based study. Physics in Medicine and Biology, 48, p. 2199-2216, 2003.

[10] D. Dean, J. Kamath, J. L. Duerk and E. Ganz, Validation of Object-Induced MR Distortion Correction for Frameless Stereotactic Neurosurgery, IEEE Transactions on Medical Imaging, 17(5), p. 810-817, 1998.

[11] R. Steinmeier, J. Rachinger, M. Kaus, O. Ganslandt, W. huk and R. Fahlbusch, Factors Influencing the Application Accuracy of Neuronavigation systems, Stereotactic and Functional Neurosurgery, 75, p. 188-202, 2000.

[12] C. R. Maurer Jr., G. B. Aboutanos, B. M. Dawant, S. Gadamsetty, R. A. Margolin, R. J. Maciunas and J. M. Fitzpatrick, Effect of Geometric Distortion Correction in MR on Image Registration Accuracy. Journal of Computer Assisted Tomography, 20(4), p. 666-676, 1996.

[13] C. R. Mascott, J. C. Sol, P. Bousquet, J. Lagarrigue, Y. Lazorthes and V. Lauwers-Cances. Quantification of true in vivo (application) accuracy in cranial image-guided surgery: influence of mode of patient registration. Neurosurgery, 59(1 Suppl. 1), p. 146-156, 2006.

[14] Aa. Grønningsæter, A. Kleven, S. Ommedal, T. E. Aarseth, T. Lie, F. Lindseth, T. Langø and G. Unsgaard, SonoWand, an Ultrasound-based Neuronavigation System, Neurosurgery, 47(6), p. 1373-1380, 2000.

[15] M. M. Bonsanto, A. Staubert, C. R. Wirtz, V. Tronnier and S. Kunze, Initial Experience with an Ultrasound-Integrated Single-Rack neuronavigation system, Acta neurochirurgica (Wien), 143, 1127-1132, 2001.

[16] W. Tirakotai, D. Miller, S. Heinze, L. Benes, H. Bertalanffy and U. Sure, A Novel Platform for Image-guided Ultrasound, Neurosurgery, 58, p. 710-718, 2006.

[17] R. W. Prager, R. N. Rohling, A. H. Gee and L. Berman, Rapid calibration for 3-D freehand ultrasound, Ultrasound in Medicine and Biology, 24(6), p. 855-869, 1998.

[18] R. M. Comeau, A. F. Sadikot, A. Fenster and T. M. Peters, Intraoperative ultrasound for guidance and tissue shift correction in image-guided neurosurgery, Medical Physics, 27(4), p. 787-800, 2000.

[19] J. M. Blackall, D. Ruecert, C. R. Maurer Jr., G. P. Penney, D. L. G. Hill and D. J. Hawkes, An Image Registration Approach to Automated calibration for Freehand 3D Ultrasound, In Proc. MICCAI 2000, p. 462-471, 2000.

[20] F. Lindseth, G. A. Tangen, T. Langø and J. Bang, Probe calibration for freehand 3-D ultrasound, Ultrasound in Medicine and Biology, 29(11), p. 1607-1623, 2003.

[21] F. Rousseau, P. Hellier and C. Barillot, Confhusis: A robust and fully automatic calibration method for 3D freehand ultrasound, Medical Image Analysis, 9, p. 25-38, 2005.

[22] L. Mercier, T. Langø, F. Lindseth and D. L. Collins, A review of calibration techniques for freehand 3-D ultrasound systems, Ultrasound in Medicine and Biology, 31(4), p. 449-471, 2005.

[23] G. M. Treece, A. H. Gee, R. W. Prager, C. J. C. Cash and L. H. Berman, High-definition freehand 3-D ultrasound, Ultrasound in Medicine and Biology, 29(4), p. 529-546, 2003.

[24] M. J. Gooding, S. H. Kennedy and J. A. Noble, Temporal calibration of freehand three-dimensional ultrasound using image alignment, Ultrasound in Medicine and Biology, 31(7), p. 919-927, 2005.

[25] F. Rousseau, P. Hellier and C. Barillot, A Novel temporal Calibration Method for 3-D Ultrasound, IEEE transactions on Medical Imaging, 25(8), p. 1108-1112, 2006.

[26] S. Sherebrin, A. Fenster, R. N. Rankin and D. Spence, Freehand three-dimensional ultrasound: implementation and application, In. Proc. SPIE, p. 296-303, 1996.

[27] J. W. Trobaugh and W. D. Richard, Three dimensional imaging with stereotactic ultrasonography ,Computerized Medical Imaging and Graphics, 18(5), p. 315-323, 1994.

[28] C. D. Barry, C. P. Allott, N. W. John, P. M. Mellor, P. A. Arundel, D. S. Thomson and J. C. Waterton, Three dimensional freehand ultrasound: image reconastruction and volume analysis, Ultrasound in Medicine and Biology, 23(8), p. 1209-1224, 1997.

[29] Q.-H. Huang and Y.-P. Zheng, An adaptive squared-distance-weighted interpolation for volume reconstruction in 3D freehand ultrasound, In Press Ultrasonics, 30, 2006.

[30] R. Rohling A. H. Gee, L. H. Berman and G. M. Treece. Radial basis function interpolation for freehand 3D ultrasound. In Proc. IPMI, LNCS vol. 1613, p. 478-483, 1999.

[31] G. P. Penney, J. A. Schnabel, D. Rueckert, M. A. Viergever and W. J. Niessen, Registration-based interpolation, IEEE Transactions on Medical Imaging, 23(7), p. 922-926, 2004.

[32] J. M. Sanchez and J. S. Marques, A rayleigh reconstruction/interpolation algorithm for 3D ultrasound, Pattern recognition letters, 21, p. 917-926, 2000.

[33] P. Coupé, P. Hellier, N. Azzabou and C. Barillot, 3D freehand Ultrasound Reconstruction Based on Probe Trajectory, In Proc. MICCAI 2005, LNCS vol. 3748, p. 597-604, 2005.

[34] A. Jodicke, T. Springer and D.-K. Boker, Real-time integration of ultrasound into neuronavigation: technical accuracy using light emitting-diode-based navigation system, Acta neurochirurgica (Wien), 146, p. 1211-1220, 2004.

[35] A. H. Jacobs, L. W. Kracht, A. Gossman, M. A. Ruger, A. V. Thomas, A. Thiel and K. Herholz, Imaging in Neurooncology, NeuroRx, 2, p. 333-347.

[36] W. B. Pope, J. Sayre, A. Perlina, J. P. Villablanca, P. S. Mischel and T. F. Cloughesy, MR imaging correlates of survival in patients with high-grade gliomas. American Journal of Neuroradiology, 26, p. 2466-2474, 2005.

[37] W. A. Kalender, X-ray computed tomography, Physics in Medicine and Biology, 51, p. 29-43, 2006.

[38] S. Sunaert, Presurgical Planning for Tumor Resection, Journal of Magnetic Resonance Imaging, 23, p. 887-905, 2006.

[39] D. G. Jamieson and J. H. Greenberg, Positron Emission Tomography of the Brain, Computerized Medical Imaging and Graphics, 13(1), p. 61-79.

[40] N. K. Logothetis, The neural basis of the blood-oxygen-level-dependent functional magnetic resonance imaging signal, Magnetic Resonance Imaging, 22(10) p. 1517-31, 2004.

[41] D. van Westen, G. Skagerberg, J. Olsrud, P. Fransson and E.-M. Larsson, Functional magnetic resonance imaging at 3T as a clinical tool in patients with intracranial tumors, Acta radiologica, 6, 2005, p. 599-609.

[42] D. Tampieri, D. Melancon and R. Ethier, The role of computer tomographic angiography in the assessment of intracranial vascular disease, Neuroimaging clinics of North America, 6(3), p. 759-767, 1996.

[43] O. Ozsarlak, J. W. Van Goethem, M. Maes and P. M. Parizel, MR angiography of the intracranial vessels: technical aspects and clinical applications, Neuroradiology, 46, p. 955-972, 2004.

[44] H. J. Cloft, K. J. Murphy, M. R. Prince and J. A. Brunberg, 3D Gadolinium-enhanced MR Angiography of the Carotid Arteries, Magnetic Resonance Imaging, 14(6), p. 593-600, 1996.

[45] G. J. Dohrmann and J. M. Rubin, History of intraoperative ultrasound in neurosurgery, Neurosurgery clinics of North America, 12(1), p. 155-166, 2001.

[46] M. C. Preul and W. Feindel, A history of brain imaging technology in neurosurgery, Neurosurgery clinics of North America, 12(1), p. 127-143, 2001.

[47] M. I. Miga, K. D. Paulsen, J. M. Lemery, S. D. Eisner, A. Hartov, F. E. Kennedy and D. W. Roberts, Model-Updated Image Gudence: Initial Clinical Experiences with Gravity-Induced Brain Deformation, IEEE Transactions on Medical Imaging, 18(10), p. 866-874, 1999.

[48] O. Skrinjar, A. Nabavi and J. Duncan, Model-driven brain shift compensation, Medical Image Analysis, 6, p. 361-373, 2002.

[49] G. Soza, C. Nimsky, G. Greiner and P. Hastreiter, Estimating Mechanical Brain Tissue properties with Simulation and Registration, In Proc. MICCAI 2004, LNCS vol. 3217, p. 276-283, 2004.

[50] T. Arbel, X. Morandi, R. M. Comeau and D. L. Collins, Automatic Non-linear MRI-Ultrasound Registration for the Correction of Intra-operative Brain deformations, In Proc. MICCAI 2001, LNCS vol. 2208, p. 913-922, 2001.

[51] T. Arbel, X. Morandi, R. M. Comeau, D. L. Collins, Automatic Non-linear MRI-Ultrasound Registration for the Correction of Intra-operative Brain deformation, Computer Aided Surgery, 9(4), 123-136, 2001.

[52] A. Roche, X. Pennec, G. Malandin and N. Ayache, Rigid Registration of 3D Ultrasound with MR Images: A New Approach Combining intensity and Gradient Information, IEEE Transactions on Medical Imaging, 20(10), p. 1038-1049, 2001.

[53] S. R. Stauffer and N. A. Peppas, Poly(vinyl alcohol) hydrogels prepared by freezing-thawing cyclic processing, Polymer, p. 3932-3936, 1992.

[54] K. J. M. Surry, H. J. B. Austin, A. Fenster and T. M. Peters, Poly(vinyl alcohol) cryogel phantoms for use in ultrasound and MR imaging, Physics in Medicine and Biology, 49(24), p. 5529-5546, 2004.

[55] D. L. G. Hill, C. R. Maurer, R. J Maciunas, J. A. Barwise, J. M. Fitzpatrick and M. Y. Wang, Measurement of Intraoperative Brain Surface Deformation under a Craniotomy, Neurosurgery, 43(3), p. 514-528, 1998.

[56] D. W. Roberts, M. I. Miga, A. Hartov, S. Eisner, J. M. Lemery, F. E. Kennedy and K. D. Paulsen , Intraoperative Brain Shift and Deformation: A Quantitative Analysis of Cortical Displacement in 28 Cases, Neurosurgery, 43(5), p. 749-760, 1998.

[57] A. Nabavi, P. M. Black, D. T. Gering, C. F. Westin, V. Mehta, R. S. Pergolizzi Jr, M. Ferrant, S. K. Warfield, N. Hata, R. B. Schwartz, W. M. Wells 3rd, R. Kikinis

and F. A. Jolesz, Serial Intraoperative Magnetic Resonance Imaging of Brain Shift, Neurosurgery, 48(4), p. 787-798, 2001.

[58] T. Hartkens, D. L. G. Hill, A. D. Castellano-Smith, D. J. Hawkes, C. R. Maurer, A. J Martin, W. A. Hall, H.Liu and C. L. Truwit., Measurement and Analysis of Brain Deformation During Neurosurgery, IEEE Transactions on Medical Imaging, 22(1), p. 82-92, 2003

[59] M. M. Letteboer, P. W. A. Willems, M. A. Viergever and W. J. Niessen., Brain Shift Estimation in Image-Guided neurosurgery Using 3-D Ultrasound, IEEE Transactions on Medical Imaging, 52(2), p. 268-276, 2005.

[60] C. Matula, K. Rossler, M. Reddy, E. Schindler and W. T. Koos, Intraoperative Computed Tomography Guided neuronavigation: Concepts, Efficiency, and Work Flow. Computer Aided Surgery, 3, 174-182, 1998.

[61] P. Grunert, W. Muller-Forell and K. Darabi, R. Reisch, C. Busert, N. Hopf and A. Perneczky, Basic Principles and Clinical Applications of neuronavigation and Intraoperative Computed Tomography, Computer Aided Surgery, 3(4), p. 166-173, 1998.

[62] N. Haberland, K. Ebmeier, R. Hliscs, J. P. Grunewald, J. Silbermann, J. Steenbeck, H. Nowak and R. Kalff, Neuronavigation in surgery of intracranial and spinal tumors, Journ. Canc. Res. Clin. Onc., 126, p. 529-541, 2000.

[63] N. Nakao, K. Nakai and T. Itakura, Updating of Neuronavigation Based on Images Intraoperatively Acquired with a mobile Computerized Tomographic Scanner: Technical Note. Minimally Invasive Neurosurgery, 46, p. 117-120, 2003.

[64] P. M. Black, E. Alexander, C. Martin, T. Moriarty, A. Nabavi, T. Z. Wong, R. B. Schwartz and F. Jolesz, Craniotomy for Tumor treatment in an Intraoperative Magnetic Resonance Imaging Unit, Neurosurgery, 45(3), 423-433, 1999.

[65] C. Nimsky, O. Ganslandt, P. Hastreiter and R. Fahlbusch., Intraoperative compensation for brain shift, Surgical Neurology, 10, p. 357-365, 2001.

[66] M. Ferrant, A. Nabavi, B. Macq, P. M. Black, F. A. Jolesz, R. Kikinis and S. K. Warfield , Serial registration of intraoperative MR images of the brain, Medical Image Analysis, 6, p. 337-359, 2002.

[67] P. Hastreiter, C. Rezk-Salama, G. Soza, M. Bauer, G. Greiner, R. Fahlbusch, O. Ganslandt and C. Nimsky, Strategies for brain shift evaluation, Medical Image Analysis, 8, 447-464, 2004.

[68] C. Nimsky, O. Ganslandt, B. von Keller, J. Romstock and R. Fahlbusch, Intraoperative High-Field-Strength MR Imaging: Implementation and Experience in 200 Patients, Radiology, 233, 67-78, 2004.

[69] F. A. Jolesz, Future persectives for intraoperative MRI, Neurosurgey Clinics of North America, 16(1):201-13 Jan 2005.

[70] J. A. Zagzebski, Essentians of Ultrasound Physics, Mosby editions, 1996.

[71] D. G. Gobbi, R. M. Comeau and T. M. Peters., Ultrasound/MRI Overlay with Image Warping for Neurosurgery, In Proc. MICCAI 2000, LNCS vol. 1935, p. 106-114, 2000.

[72] M. Descoteaux, A Multi-Scale Geometric Flow for Segmenting Vasculature in MRI: Theory and Validation, Master's Thesis, School Of Computer Science, McGill University, 2004.

[73] B. C. Porter, D. J. Rubens, J. G. Strang, J. Smith, S. Totterman and K. J. Parker, Three-Dimensional registration and fusion of Ultrasound and MRI Using Major Vessels as Fiducial Markers, IEEE Transactions on Medical Imaging, 20(4), p. 354-359, 2001.

[74] P. J. Slomka, J. Mandel, D. Downey and A. Fenster, Evaluation of voxel-based registration of 3-D power Doppler ultrasound and 3-D magnetic resonance angiographic images of carotid arteries, Ultrasound in Medicine and Biology, 27(7), p. 945-955, 2001.

[75] S. R. Aylward, J. Jomier, S. Weeks and E. Bullitt, Registration and Analysis of Vascular Images, International Journal of Computer Vision, 55(2/3), p. 123-138, 2003.

[76] S. R. Aylward, J. Jomier, Jean-Philippe Guyon and S. Weeks., Intra-operative 3D ultrasound augmentation, In Proc. IEEE International Symposium on Biomedical Imaging, 421-424, 2002.

[77] J. Jomier and S. R. Aylward, Rigid and deformable Vasculature-to-Image Registration: A Hierarchical Approach, In Proc. MICCAI 2004, LNCS vol. 3216, 829-836, 2004.

[78] G. P. Penney, J. A. Little, J. Weese, D. L. G. Hill and D. J. Hawkes, Registration of freehand 3D ultrasound and magnetic resonancs liver images, Medical Image Analysis, 8, p. 81-91, 2004.

[79] T. Lange, S. Eulenstein, M. Hunerbein, H. Lamecker and Peter-Michael Schlag, Augmenting Intraoperative 3D ultrasound with preoperative models for navigation in liver surgery, In Proc. MICCAI 2004, LNCS vol. 3217, p. 534-541, 2004.

[80] L. M. Lorigo, O. D. Faugeras, W. E. L. Grimson, R. Keriven, R. Kikinis, A. Navabi and C.-F. Westin, CURVES: Curve evolution for vessel segmentation, Medical Image Analysis, 5, p. 195-206, 2001.

[81] M. S. Hassouna, A. A. Farag, S. Hushek and T. Moriarty, Cerebrovascular segmentation from TOF using stochastic models. Medical Image Analysis, 10, p. 2-18, 2006.

[82] N. Passat, C. Ronse, J. Baruthio, J.-P. Armspach and C. Maillot, Magnetic resonance angiography: From anatomical knowledge to vessel segmentation, Medical Image Analysis, 10, p. 259-274, 2006.

[83] S. Kobashi, N. Kamiura, Y. Hata and F. Miyawaki, Volume-quantization-based neural network approach to 3D MR angiography image segmentation, Image and Vision Computing, 19, p. 185-193, 2001.

[84] K. Krissian, G. Malandain, N. Ayache, R. Vaillat and Y. Trousset, Model-based detection of tubular structures in 3D images, Computer Vision and Image Understanding, 80, p. 130-171, 2000.

[85] I. Reinertsen, M. Descoteaux, S. Drouin, K. Siddiqi and D. L. Collins, Vessel Driven Correction of Brain Shift, In Proc. MICCAI 2004, LNCS vol. 3217, p. 208-216, 2004.

[86] D. L. Collins and A. C. Evans, ANIMAL: Validation and application of non-linear registration-based segmentation, IJPRAI, 11(8), 1271-1294, 1997.

[87] K. Palagyi, E. Sorantin, E. Balogh, A. Kuba, C. Halmai, B. Erdohelyi and K. Hausegger, A sequential 3D Thinning Algorithm and Its Medical Applications, In Proc. IPMI 2001, LNCS vol. 2082, p. 409-415, 2001.

[88] T. Deschamps and L. D. Cohen, Fast extraction of minimal paths in 3D images and applications to virtual endoscopy, Medical Image Analysis, 5, p. 281-299, 2001.

[89] S. R. Aylward and E. Bullitt, Initialization, Noise, Singularities, and Scale in Height Ridge Traversal for Tubular Object Centerline Extraction, IEEE Transactions on Medical Imaging, 21(2), 2002.

[90] O. Wink, W. J. Niessen and M. A. Viergever, Multiscale Vessel Tracking, IEEE Transactions on Medical Imaging, 23(1), 2004.

[91] A. F. Frangi, W. J. Niessen, K. L. Vincken and M. A. Viergever, Muliscale Vessel Enhancement Filtering, In Proc. MICCAI 1998, LNCS vol. 1496, p. 130-137, 1998.

[92] A. Vasilevskiy and K. Siddiqi, Flux Maximizing Geometric Flows, IEEE PAMI, 24(12), p. 1565-1578, 2002.

[93] K. Siddiqi, S. Bouix, A. Tannenbaum and S. W. Zucker, Hamilton-Jacobi skeletons, International Journal of Computer Vision, 48(3), 2002.

[94] S. Bouix, K. Siddiqi and A. Tannenbaum., Flux Driven Automatic Centerline Extraction, Medical Image Analysis, 9, p. 209-221, 2005.

[95] P. J. Besl and N. D. McKay, A Method for Registration of 3D Shapes, IEEE PAMI, 14(2), p. 239-256, 1992.

[96] G. Turk and M. Levoy, Zippered Polygon Meshes from Range Images, In Proc. SIGGRAPH, p. 311-318, 1994.

[97] T. Masuda, K. Sakaue and N. Yokoya, Registration and Integration of Multiple Range Images for 3-D Model Construction, Proceedings of ICPR, 1996.

[98] S. Weik, Registration of 3-D Registration of 3-D Partial Surface Models Using Luminance and depth Information, In Proc. International Conference on 3-D Digital Imaging and Modeling, p. 93-100, 1997.

[99] S. Rusinkiewicz and M. Levoy, Efficient Variants of the ICP Algorithm, In Proc. International Conference on 3-D Digital Imaging and Modeling, 2001.

[100] M. A. Fischler and R. C. Bolles, Random Sample Consensus: A Paradigm for Model Fitting with Applications to Image Analysis and Automated Cartography, Comm of the ACM, 24, p. 381-395, 1981.

[101] K. Pulli, Multiview Registration for Large Data Sets, In Proc. International Conference on 3-D Digital Imaging and Modeling, p. 160-168, 1999.

[102] E. Trucco, A. Fusiello and V. Roberto, Robust motion and correspondence of noisy 3-D point sets with missing data, Pattern Recognition Letters, 20, p. 889-898, 1999.

[103] D. Chetverikov, D. Svirko and D. Stepanov, The Trimmed Iterative Closest Point Algorithm, In Proc. International Conference on Pattern Recognition, 2002.

[104] M. Otte, Elastic Registration of fMRI data Using Bézier-Spline Transformations, IEEE Transactions on Medical Imaging, 20(2), p. 193-206, 2001.

[105] D. R. Forsey and R. H. Bartels, Hierarchical B-Spline Refinement, Computer Graphics, 22(4), p. 205-212, 1988.

[106] Z. Xie and G. E. Farin, Image Registration Using Hierarchical B-Splines, IEEE Transactions on Visualization and Computer Graphics, 10(1), p. 85-94, 2004.

[107] C. J. Kuo, J.-H. Hung, M.-H. Tsai and P.-L. Shih, Elastic Body Spline Technique for Feature Point generation and Face Modeling, IEEE Transactions on Image Processing, 14(12), p. 2159-2166, 2005.

[108] G. P. Penney, J. A. Little, J. Weese, D. L. G. Hill and D. J. Hawkes, deforming a Preoperative Volume to Represent the Intraoperative Scene, Computer Aided Surgery, 7, p. 63-73, 2002.

[109] Z. R. Yang, A novel radial basis function neural network for discriminant analysis, IEEE Transactions on Neural Networks, 17(3), p. 604-612, 2006.

[110] M. Fornefett, K. Rohr and H.S. Stiehl. Elastic registration of medical images using radial basis functions with compact support. In Proc. CVPR99, p. 402-407, 1999.

[111] L. Zagorchev and A. Goshtasby, A Comparative Study of Transformation functions for Nonrigid Image Registration, IEEE transactions on Image Processing, 15(3), p. 529-538, 2006.

[112] P. J. Rousseeuw and A. M. Leroy, Robust Regression and Outlier Detection, Wiley Series in Probability and Mathematical Statistics, first edition, 1987.

[113] F. L. Bookstein, Principal Warps: Thin-plate Splines and the decomposition of Deformations, IEEE Transactions on PAMI, 11(6), p. 567-585, 1989.

[114] F. L. Bookstein, Shape and the Information in Medical Images: A Decade of the Morphometric Synthesis, Computer Vision and Image Understanding, 66(2), p. 97-118, 1997.

[115] Y. Chen and G. Medioni, Object Modeling by Registration of Multiple Range Images, IEEE Conference on Robotics and Automation, p. 145-155, 1991.

[116] K. Rohr, H. S. Stiehl, R. Sprengel, T. M. Buzug, J. Weese and M. H. Kuhn, Landmark-Based Elastic Registration using Approximating Thin-Plate Splines, IEEE Transactions on Medical Imaging, 20(6), p. 526-534, 2001.

[117] G. Borgefors, Hierchical Chamfer Matching: A parametric Edge Matching Algorithm, IEEE Transactions on PAMI, 10(6), p. 849-865, 1988.

List of abbreviations

AVM	Arteriovenous malformation
B-mode	Brightness mode
BOLD	Blood oxygen level dependent
CBV	Cerebral blood volume
CSF	Cerebral blood flow
CT	Computer tomography
CTA	Computer tomography angiography
DSA	Digital subtraction angiography
DTI	Diffusuion tensor imaging
fMRI	Functional magnetic resonance imaging
FWHM	Full width at half maximum
Gd	Gadolinium
ICP	Iterative closest points
iMRI	Intraoperative magnetic resonance imaging
LMS	Least median of squares
LTS	Least trimmed squares

MCA	Middle cerebral artery
MEG	Magnetoencephalography
MOTSA	Multiple overlapping thin slab acquisition
MRA	Magnetic resonance angiography
MRI	Magnetic resonance imaging
PC	Phase contrast
PD	Proton density
PET	Positron emission tomography
PVA	Polyvinyl alcohol
PVAc	Polyvinyl alcohol cryogel
RANSAC	Random sample consensus
RMS	Root mean square
ROI	Region of interest
SNR	Signal-to-noise ratio
TOF	Time of flight
TPS	Thin-plate splines
US	Ultrasound
USA	Ultrasound angiography